CONTROLLED ASSEMBLY OF SEMICONDUCTING POLYMERS: FROM FUNDAMENTAL UNDERSTANDING TOWARDS STRETCHABLE ELECTRONICS

A Dissertation
Presented to
The Academic Faculty

by

Dalsu Choi

In Partial Fulfillment
of the Requirements for the Degree
Ph.D. in the
School of Chemical & Biomolecular Engineering

Georgia Institute of Technology
December 2015

CONTROLLED ASSEMBLY OF SEMICONDUCTING POLYMERS: FROM FUNDAMENTAL UNDERSTANDING TOWARDS STRETCHABLE ELECTRONICS

Approved by:

Dr. Elsa Reichmanis, Advisor
School of Chemical and Biomolecular Engineering
Georgia Institute of Technology

Dr. Dennis W. Hess
School of Chemical and Biomolecular Engineering
Georgia Institute of Technology

Dr. Samuel Graham
The George W. Woodruff School of Mechanical Engineering
Georgia Institute of Technology

Dr. William J. Koros
School of Chemical and Biomolecular Engineering
Georgia Institute of Technology

Dr. J. Carson Meredith
School of Chemical and Biomolecular Engineering
Georgia Institute of Technology

Date Approved: November 6th, 2015

This thesis is dedicated to my parents and brother.

ACKNOWLEDGEMENTS

First and foremost, I would like to thank my advisor, Dr. Elsa Reichmanis, for her steady and persistent support throughout my PhD years. Without her guidance and support, I would not make it to graduation. I will always keep your valuable advices about professional attitude toward work and life in heart!

I also want to thank to my PhD thesis committee members: Dr. William J. Koros, Dr. Dennis W. Hess, Dr. J. Carson Meredith, and Dr. Samuel Graham for their helpful comments during my PhD years.

I would like to sincerely thank to all the group members. I cannot expect all the accomplishment I made without their help and discussions. Avi, Boyi, Mincheol, Jihwan, Nabil, Ping-Hsun, Cornelia, Nils, Zhibo, Rui, Yo Han, Bailey and Mike, thank you all!

For all my friends I met in Georgia Tech, I was really lucky to have all the valuable relationship with you. We’ve shared happiness and struggles during PhD studies and I will never forget those days!

Lastly, I would like to acknowledge endless love and support from my family.

TABLE OF CONTENTS

CHAPTER

LIST OF FIGURES

Page

SUMMARY

As a new class of electronic material possessing characteristics combining the electrical properties of inorganic electronic materials with the properties of plastics, organic electronics materials have gained a lot of traction for over 40 years since their discovery by Alan MacDiarmid, Hideki Shirakawa and Alan Heeger in 1972. Solution processibility and low-temperature processibility of organic electronic materials endowed them a unique status as a promising alternative to their inorganic counterparts for realization of flexible, stretchable, low-cost electronics. However, due to their intrinsic low electrical performance, in a field of organic electronics, enhancement of charge carrier mobility within the active layer has been a grand challenge. Various approaches including development of novel conjugated materials, interface optimization, and solution processing methods have been introduced to the field. Among them more recently, solution processing methods promoting ordering of organic conjugated molecules are gaining attentions as a simple and effective route to improve charge carrier mobility. Nonetheless, though important, there have been only limited studies pertaining to the molecular ordering mechanism during solution processing.

In the second chapter of this thesis, we provide mechanistic elucidation of poly(3-hexylthiophene) (P3HT) molecular assembly during solution processing based on first-time experimental demonstration of controlled assembly of high-mobility, rod-like poly(3-hexylthiophene) (P3HT) nanostructures through synergistic combination of non-solvent addition followed by ultrasonication. Application of a simple 2-step crystallization model including nucleation and growth could successfully explain the

assembly process of P3HT mesoscale structures. We believe that understanding of the conjugated polymer assembly process obtained in this study using P3HT can be expanded to other conjugated molecule-solvent systems so that molecular assembly through solution processing methods can be applied in a more systematic and controllable manner.

Next, in chapter 3, through quantification of solubility by adopting Hansen solubility parameters (HSPs), it is confirmed that there is a direct influence of solubility on feasibility of the ultrasonication technique as a means to induce semiconducting polymer (P3HT) assembly. Further, using HSPs as a platform, the solubility of the solution system is controlled in a rational manner. Based on HSP calculations, solubility of P3HT solution system, which is initially unresponsive to ultrasound treatment, is successfully adjusted in a way that P3HT molecular assembly can take place through ultrasonication.

Finally, in chapter 4, an inverse relationship between mechanical resiliency and charge carrier mobility/molecular ordering in conjugated polymer systems is determined definitively through systematic interrogation of poly(3-hexylthiophene) (P3HT) films with varied degrees of molecular ordering. As a solution to the dilemma, a simple elastomer blend approach incorporating the advantages of polymer molecular interactions and crystallization mechanisms is presented. A composite of processed P3HT and poly(dimethylsiloxane) (PDMS) is shown to create semiconducting films exhibiting both high ductility and superior mobility versus single component organic semiconductor counterparts.

CHAPTER 1

INTRODUCTION

1.1 Organic Electronic Materials

1.1.1 Overview

The pioneering discovery of conducting polymers in 1972 by Alan MacDiarmid, Hideki Shirakawa and Alan Heeger introduced π-conjugated organic materials as a whole new class of electronic material.[1] Their work successfully demonstrated electrical conductivity in the π-conjugated polymer (polyacetylene) upon chemical doping. Since this discovery, conjugated organic electronic materials have attracted much attention in academia and industry due to their materials characteristics combining the electrical properties of rigid inorganic materials with the properties of plastics. The significance of their discovery was rewarded by the Nobel Prize in 2000.[2] Organic π-conjugated electronic materials possess unique intrinsic properties such as low temperature and solution processibility.[3–7] Such properties of organic electronic materials present clear distinctions over mainstream inorganic electronic materials which require costly high temperature, high vacuum processes for device fabrication.

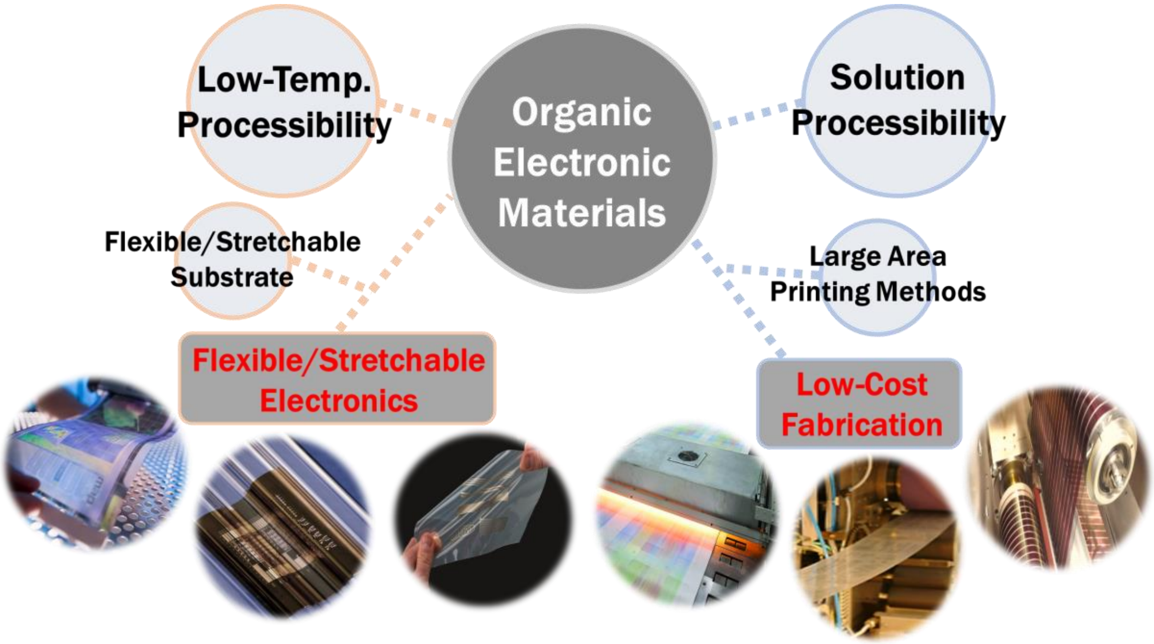

Figure 1.1 Branch diagram summurizing advantages of organic electronic materials in material perspective and their applications.

Solution processibility of organic materials allows direct adoption of large area printing techniques such as gravure and roll-to-roll printing to fabricate electronic devices,[8–10] ensuring significant cost reduction. Moreover, low temperature processibility enables easy accommodation of flexible or stretchable substrates having low melting temperatures. As a result, organic electronic materials have built up solid status as a promising alternative to their inorganic counterparts for realization of flexible, stretchable, low-cost electronics. However, organic electronic materials also have some intrinsic drawbacks. First, the performance of organic electronic materials degrades under atmospheric conditions where oxygen and water are present. State-of-the-art encapsulation techniques provide a quite solid solution for this issue and widely available commercial OLED displays exhibit superb stability.[11–13] Second, and perhaps the most critical drawback, is inferior electronic performance compared to conventional inorganic semiconductors. Charge carrier mobility, a figure-of-merit representing charge carrier transport efficiency, of grain-engineered polycrystalline silicon reaches a value up to 914 $cm^2\ V^{-1}\ s^{-1}$, while solution processible novel organic small molecules processed through state-of-the art techniques exhibit average mobility of up to only 25 $cm^2\ V^{-1}\ s^{-1}$.[14,15]

To date, studies have been focused on the design and synthesis of new organic electronic materials having improved electrical properties.[16–18] Currently however, studies related to the use of processing methods to enhance the properties of the organic semiconducting materials have gained significant attention.[3–6,19] In particular, development of conjugated polymer ordering/assembly coupled with systematic investigations relating electrical properties with the evolution of conjugated polymer molecular ordering/assembly is considered to be vital.

1.1.2 Market Analysis[20,21]

Over the past 40 years, extensive research efforts have enabled successful application of organic electronics materials on various platforms such as Organic Field Effect Transistors (OFET), Organic Photovoltaics (OPV) and Organic Light Emitting Diodes (OLED) and now in 2015, flexible, even stretchable electronic devices have been successfully demonstrated an a lab scale. In the commercial market, however, organic electronic devices based on rigid substrates still constitute the major portion of sales, but flexible commercial OLED display panels are scheduled to be released in 2016, which is expected to be a ‘game-changer’, initiating a transition from rigid electronics to flexible electronics in the commercial electronics market. All these successful introductions of technologies based on organic electronic materials suggest a very positive future for entire markets related to organic electronic materials. A market analysis report published in 2012 by IDTechEX stated that the size of the market related to organic electronic materials marked $ 2.394 billion in 2011 and it was speculated that a rapid expansion reaching $ 44.247 billion would take place by 2021. A more recent market report from the Japan based research firm Fuji-Keijai group published in 2015 also expects the same radical market expansion. According to the Fuji-Keijai report, the market size for organic electronic products in 2014 was $ 6.366 billion and the report expected a growth reaching $ 35.227 billion by 2030. Interestingly, the actual market size in 2014 ($ 6.366 billion) was higher than the speculated market size presented by IDTechEX in 2012, which was $ 5.483 billion.The comparison clearly indicates more rapid expansion of this market sector than was speculated in 2012. In conclusion, the organic electronics industry has entered a phase of realistic growth, with significant revenues. As a consequence, huge demand for further market expansion through application of organic electronics in various areas is expected, accompanied by significant attention to organic electronics research.

1.2 Charge Transport within Organic Electronic Materials

1.2.1 π-conjugation and formation of HOMO-LUMO energy gap[22–25]

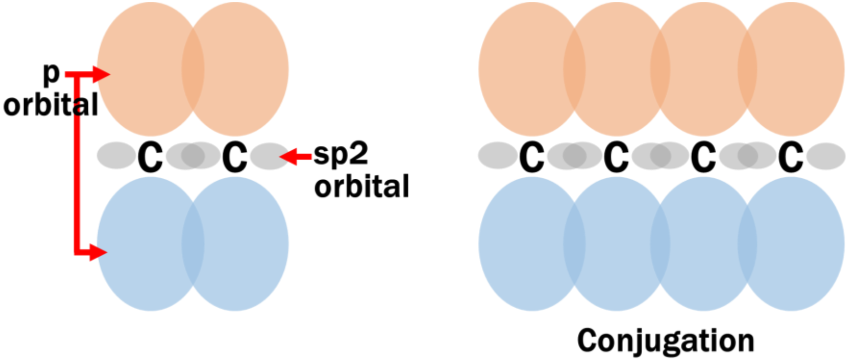

Figure 1.2 Pictorial explanation about formation of π-conjugation

A key concept that need to be understood in the discussion of organic electronics is π-conjugation. As it gives rise to formation of the energy gap which provides distinctive electrical and optical properties to organic π-conjugated materials. Adjacent p-orbitals across σ-bonding formed by horizontal overlap of sp^2 hybridized orbitals vertically overlap and form π-bonds so that valence electrons resident in p-orbitals delocalize and move freely between them (**Figure 1.2)**. As a result, in molecules having three or more adjacent p-orbitals, interactions among multiple p-orbitals enables electrons to be delocalized throughout a chain which leads to conjugation. Conjugation gives to rise multiple energy levels, with and without electrons, thereby defining and energy gap which affords organic π-conjugated materials their electronic properties resembling inorganic semiconductors with a band gap.

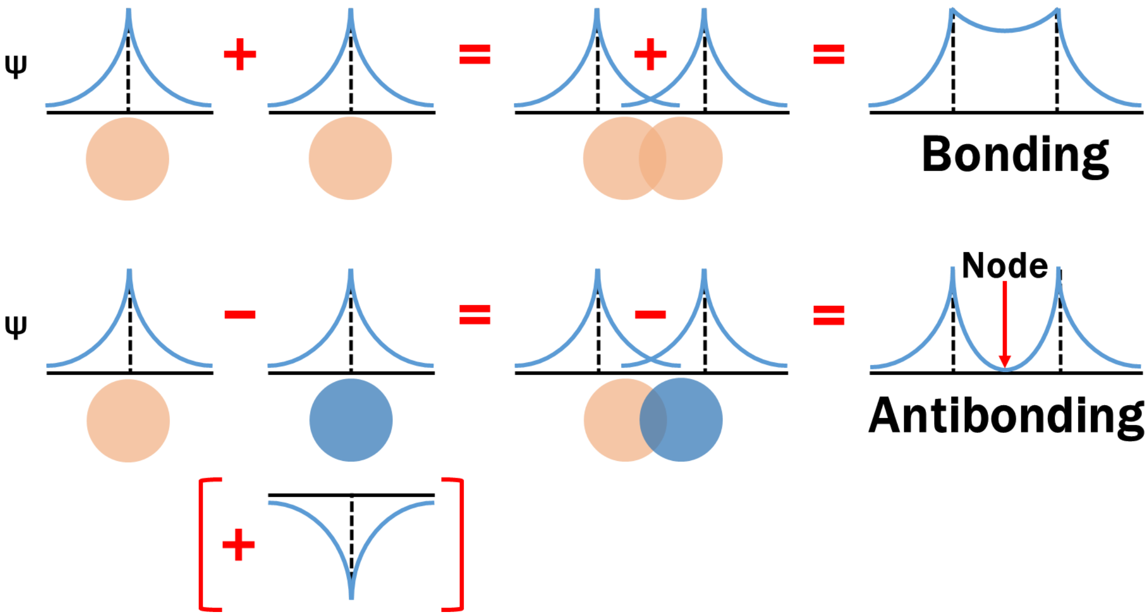

Figure 1.3 Formation of bonding and antibonding based on molecular orbital theory

Emergence of an energy gap in conjugated systems can be explained based on molecular orbital (MO) theory considering an orbital as a spatial distribution of electrons surrounding a 'molecule'. In MO theory, interacting atomic orbitals (AO) are combined to form the same number of multiple MOs. As orbitals are wave functions, combinations of AOs can take place in both constructive and destructive ways. MO formed as a consequence of constructive AO combination has the highest electron probability density between given nuclei and is called a 'Bonding MO'; while destructive combination of AOs forms an 'Antibonding MO' and a node, a region where there is zero probability of electron presence which appears between nuclei (**Figure 1.3)**. High electron density population between nuclei in a bonding MO reduces nuclei repulsions. Thus, the energy associated with a stabilized bonding MO is lower than that of the original AO. Conversely, an antibonding MO has higher energy than the AO because the probability of electrons residing there is low in the area outside of region between nuclei.

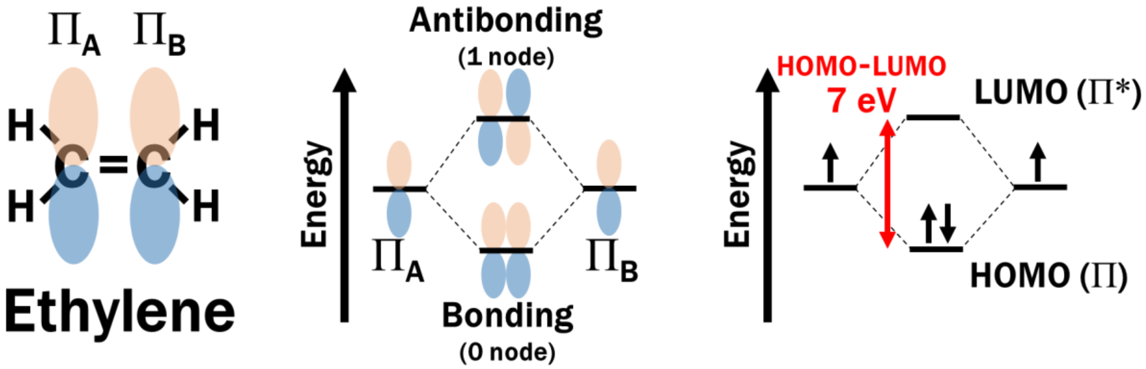

Figure 1.4-a Schematic illustration of HOMO-LUMO energy gap formation in Ethylene

Let's take a look at ethylene as a first example of an MO energy level diagram (**Figure 1.4-a)**. Ethylene has two p-orbitals interacting with each other giving two possible combinations of MOs. The bonding MO is located in the lower energy level and electrons should fill that lower energy level following the Aufbau principle and Pauli's exclusion principle.[22,23] The outcome provides for the molecular orbital energy level diagram of ethylene. The lower energy MO is filled with electrons and is called highest occupied molecular orbital (HOMO). In same manner, the empty higher energy MO is called lowest unoccupied molecular orbital (LUMO). Energy gap between HOMO and LUMO is the amount of energy required to excite the electron in HOMO to empty LUMO which exactly resembles the conduction and valence band of an inorganic semiconducting material, except that ethylene does not possess an energy band.

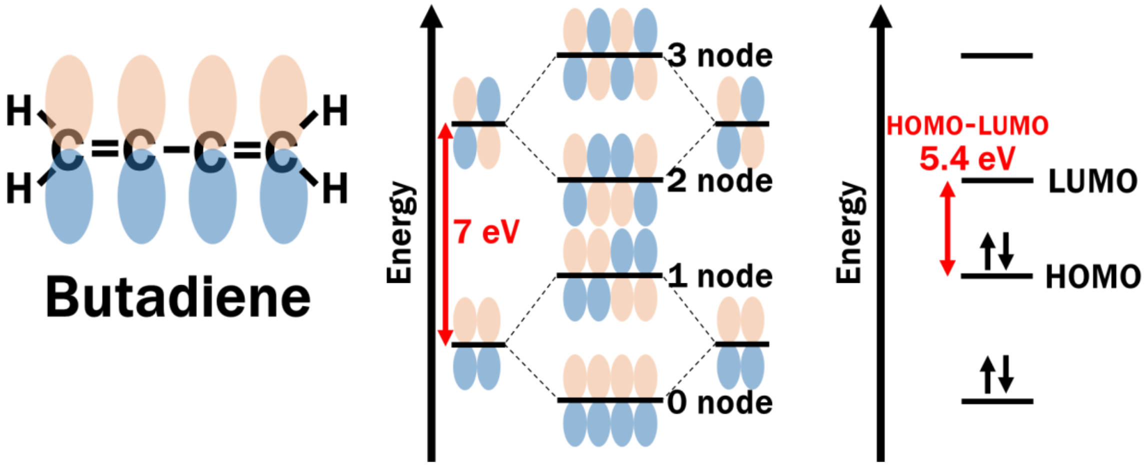

Figure 1.4-b Schematic illustration of HOMO-LUMO energy gap formation in Butadiene

Next, let's move on to butadiene (**Figure 1.4-b)**. Butadiene has four p-orbitals interacting each other giving 4 different combinations. All-bonding MO are located at the lowest energy levels and all-antibonding MO have the highest energy levels. Difference arise from intermediate MOs, but the principle is exactly same. MOs with more nodes from antibonding configurations have higher energy than MOs with fewer nodes. After placing 4 electrons into the lowest energy molecular orbitals, the HOMO and LUMO of butadiene can be identified. One thing to be noted is that HOMO and LUMO energy gap of butadiene is smaller than that of ethylene. The Energy difference between energy levels defined by antibonding and bonding of two p-orbitals (ethylene) is 7 eV. Energy level formation of butadiene with 4 p-orbitals can be expressed as a combination of energy levels consisting of two p-orbitals. HOMO and LUMO of butadiene, which can be expressed as fusion of HOMO and LUMO of ethylene, lie between the energy gap of ethylene, thus, the HOMO-LUMO energy gap for butadiene has a smaller value than that of ethylene (5.4 eV vs. 7 eV).

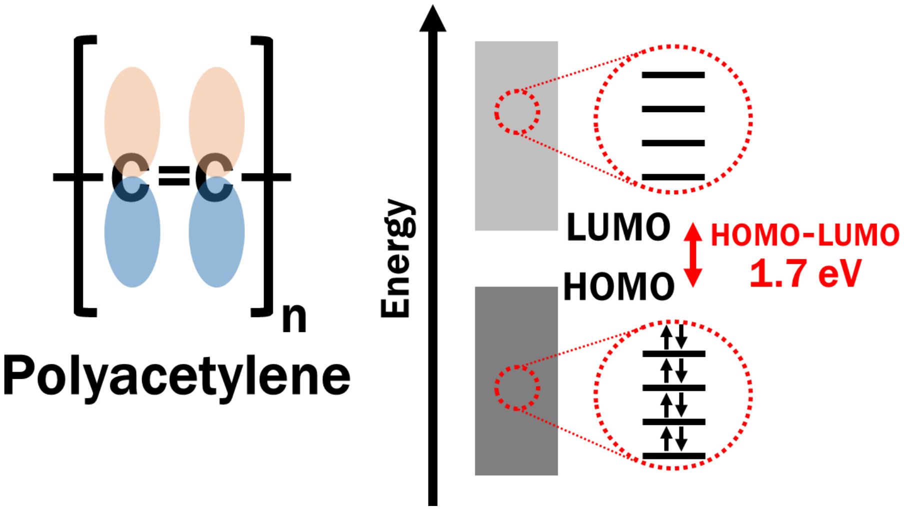

Figure 1.4-c HOMO-LUMO and band-like energy structure formation in Polyacetylene system.

In similar fashion, it can be easily deduced that a molecule with longer conjugation length and having a larger number of AO combinations would have a larger number of MO energy levels and finally would form a band-like energy structure resembling the conduction and valence bands of inorganic semiconductor (**Figure 1.4-c)**. As a function of AO combination, the HOMO-LUMO gap becomes smaller and the value finally converges into a finite number (1.7 eV for polyacetylene).

1.2.2 Charge Hopping in Organic Semiconducting Materials[3,4,19,26–30]

One major obstacle inhibiting straightforward translation of organic semiconducting materials into various commercial electronics is inferior charge carrier transport properties compared to mainstream inorganic electronic materials. Therefore, significant research efforts have aimed to improve the inferior charge carrier transport properties. To handle this problem in rational manner, we need to understand fundamentals of charge carrier transport phenomena within materials.

The main reason causing slow charge transport within organic semiconducting molecules is intrinsic low degree of molecular ordering. Charge delocalization within inorganic semiconducting materials takes place in 3 dimensions via covalent bonds throughout the entire lattice which ensures coherent, and thus fast charge transport. Conversely, segmented delocalization within organic semiconductor systems due to inevitable disorder only allows random charge hopping as a charge transport protocol. In a hopping transport regime, charge is strongly coupled with vibrations originating from structural relaxation around a localized charge. Charge should be thermally activated to overcome an energy barrier originating from vibronic coupling to hop from one site to another. So, charge transport within materials governed by hopping transport generally exhibit a positive relationship with temperature. For the semiconducting materials following band transport, however, temperature works in the opposite way. Thermally induced vibrations of molecules decrease the electronic coupling and interrupt charge movement. Except in a few high-crystallinity vacuum deposited organic small molecules,[27,31–33] charge transport within most of solution processed organic semiconducting materials follows slow hopping transport rather than fast band transport found in inorganic semiconductors.

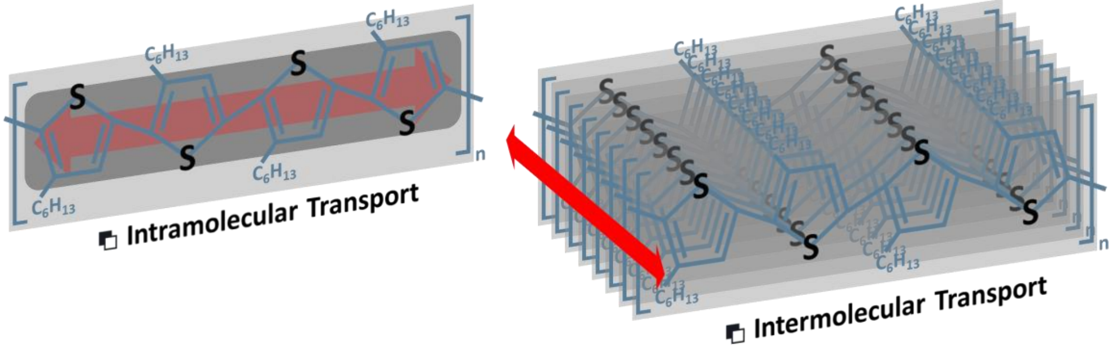

Figure 1.5 Schematic illustration of ‘intramolecular’ and ‘intermoelcular’ transport within organic conjugated materials.

Charge transport within organic electronic materials takes place in two directions. One direction of charge transport is ‘Intermolecular Charge Transport’ **(Figure 1.5)**. As name indicates, it represents charge transport from one molecule to another facilitated via π-stacking interactions, an attractive non-covalent interaction, between neighboring π clouds from conjugation. This mode of transport enables long range charge transport but is very slow compared to intramolecular transport. Another direction is along the conjugation backbone of a molecule which is referred to as ‘Intramolecular Charge Transport’ **(Figure 1.5)**. Conjugation within a molecule provides a pathway for intramolecular charge transport. In case of molecules with short and rigid conjugation backbone allowing full conjugation throughout entire backbone, intramolecular transport will follow very fast band-like transport. In a real-world situation, however, most molecules experience segmentation of conjugation along the backbone due to intrinsic steric hindrances and/or extrinsic factors such as molecular interaction with adjacent molecules (e.g. solvent molecules) **(Figure 1.6)**. So, charges need to hop from one conjugated segment to another. Still, transport speed is faster than intramolecular transport because charge is transported through uninterrupted conjugation within conjugated segment.

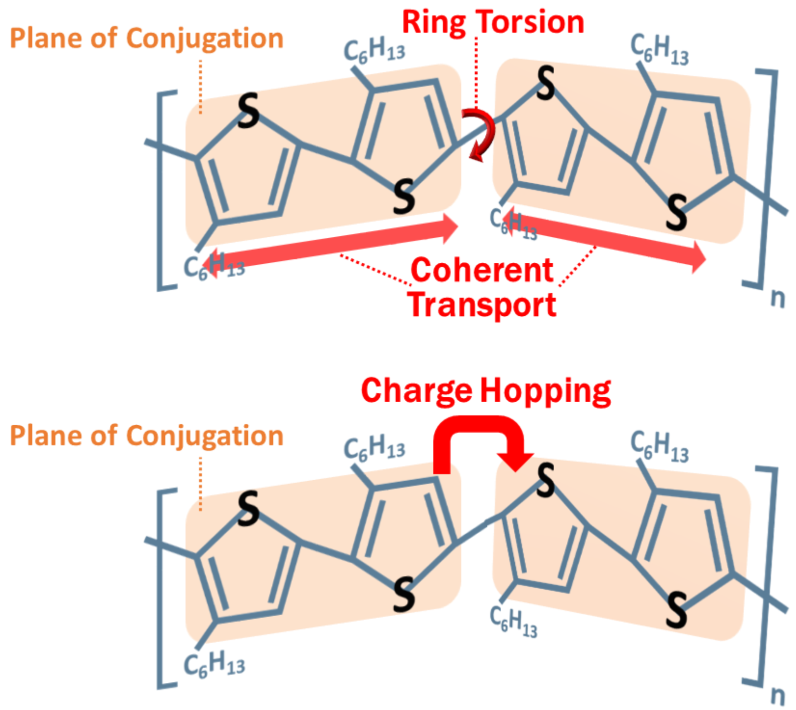

Figure 1.6 Pictorial explanation about fragmentation of conjugation backbone, a common obstacle experienced during charge carrier transport process within organic conjugated electronic materials.

In summary, both ‘intra’ and ‘inter molecular charge transport within organic electronic materials are mainly facilitated through charge hopping. Among those two modes of charge transport, intermolecular charge transport is a slower mode of transport, thus it is considered to be the rate determining step in macroscopic charge transport. As a consequence, promoting molecular organization of organic electronic materials is crucial to overcome intrinsically inferior charge carrier transport characteristics. Throughout this thesis, we will discuss methods and principles that can be implemented to adjust molecular interactions among components within solutions to enhance molecular ordering of organic semiconducting materials.

1.2.3 Charge Carrier Mobility: Quantification of Charge Carrier Transport Properties[4,5,19,25,28,34–37]

In the previous section, we covered fundamentals of charge transport, a determining factor used to judge performance of electronic devices, within organic semiconducting materials. Here, we are going to discuss the experimental methods to measure charge carrier mobility, a figure of merit representing efficiency of charge carrier transport. There are several mobility measurement methods such as measuring 'time of flight' (TOF), utilizing 'space-charge limited current' (SCLC) effect, and fabricating 'organic field effect transistor' (OFET). Among the several available methods, the charge mobility calculation method using an OFET configuration will be discussed in detail as OFET characteristics are the primary mean used in this thesis to determine charge carrier transport properties in organic semiconducting materials.

The OFETs can be classified into four different architectures (**Figure 1.7)**: (i) bottom gate, bottom contact (ii) bottom gate, top contact (iii) top gate, bottom contact (iv) top gate, top contact. In this thesis, OFET devices with bottom gate, bottom contact structure are fabricated to perform electrical characterization of organic electronic materials.

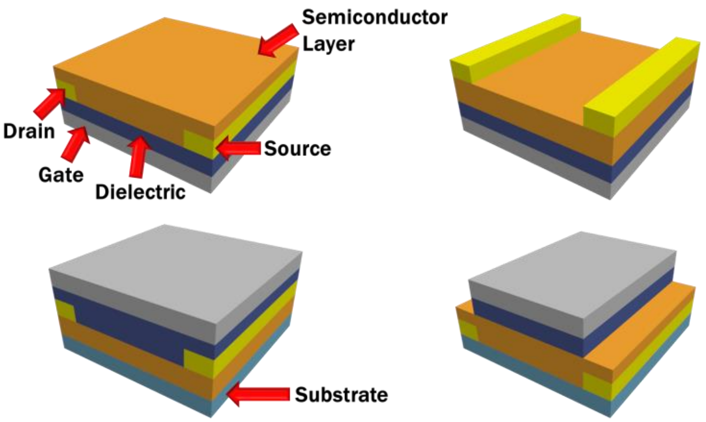

Figure 1.7 Four different configurations of OFET devices. Clockwise from top left; Bottom Contact Bottom Gate (BCBG), Top Contact Bottom Gate (TCBG), Top Contact Top Gate (TCTG), Bottom Contact Top Gate (BCTG).

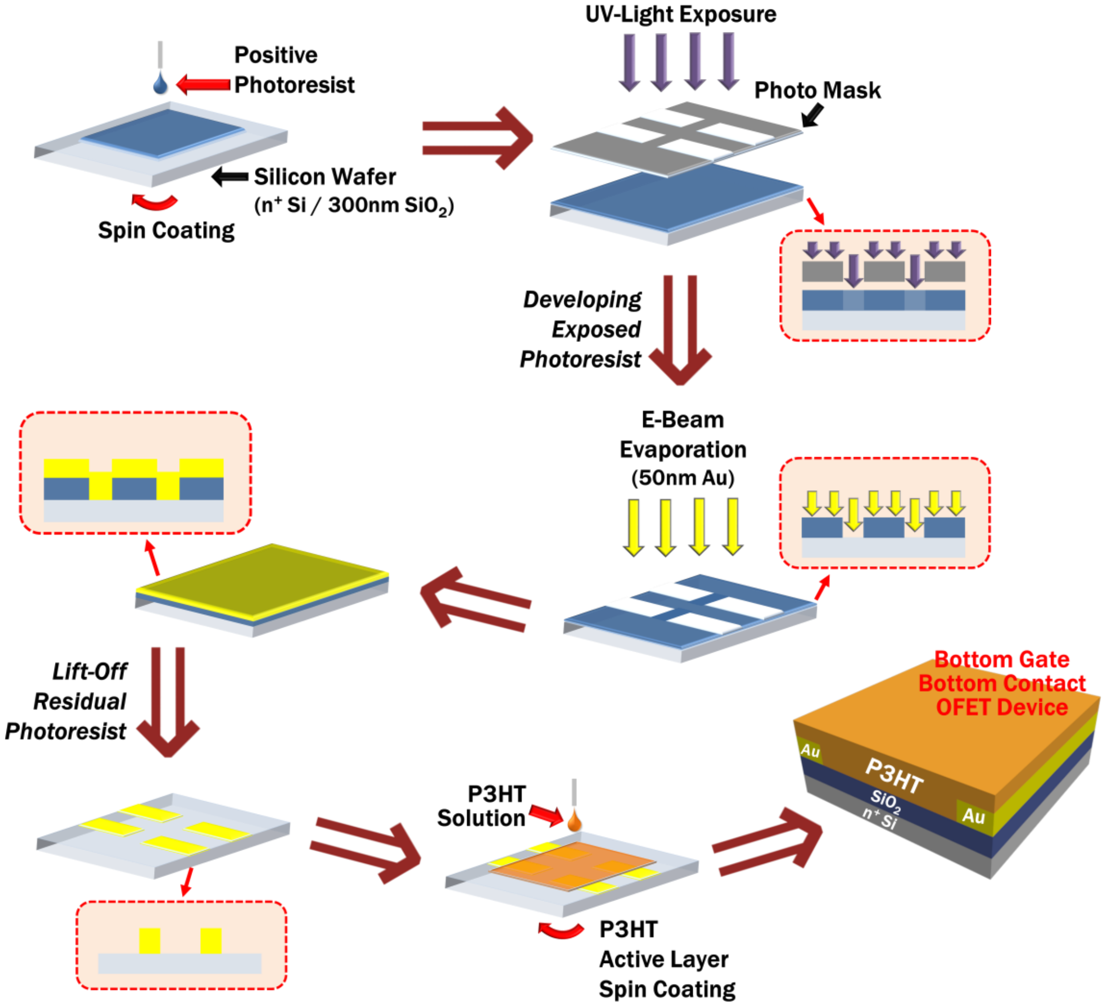

Figure 1.8 Scheme depicting fabrication process of OFET device used in this study.

The fabrication process for bottom gate bottom contact devices used in this study is as follows (**Figure 1.8)**: Highly n-doped silicon wafers with a thermally grown 300 nm thick SiO_2 dielectric surface are used as the substrate. The highly doped silicon substrate serves as the gate electrode with thermally grown SiO_2 as dielectric layer. Au is used for the source and drain contacts. The source and drain contacts are deposited using a standard photolithography based lift-off process inside a cleanroom followed by e-beam evaporation of Au. Positive photoresist (SC1318, Microposit) is spin-coated on top of n^+-Si/SiO_2 substrate. Then, long wave UV light (405nm) is exposed through photomask. After exposure, parts exposed to UV light become soluble to aqueous base developer (MF-319, Microposit) and the channel with a 50 μm gap is defined. Through an E-beam evaporation process, 50 nm of Au is deposited on top of the channel defined by the photoresist. As Au does not adhere well to a SiO_2 surface, 3 nm of Cr should be deposited as an adhesion layer before Au deposition. Immersion of the substrate for12 hr in an acetone bath lifts off residual photoresist and provides the near final device, lacking only the active semiconducting layer. Before deposition of the active semiconducting layer, all devices were cleaned for 30 min in a UV-ozone cleaner (Novascan PSD-UV) to completely remove any residual photoresist and other organic contaminants. OFET devices were prepared by spin-coating the semiconductor solutions onto pre-cleaned devices at a spin speed of 1500 rpm for 60 s in air. Finally, the devices were stored in a vacuum oven (1 Torr) overnight at 50 °C to remove residual solvent. Residual solvents within the spin-coated active layer can act as charge traps and interrupt charge hopping.

Now, we are going to cover the basic operation principles of OFET devices and details concerning charge mobility extraction methods based on a bottom gate, bottom contact device. The basic operating principle of an OFET device is quite simple (**Figure 1.9)**. Charge flow (current) from the source to drain electrodes is regulated by controlling the gate voltage. By applying bias to the gate electrode, an electric field is generated between the semiconductor layer and dielectric. Applied electric field induces dielectric polarization. As a result, charge carriers are accumulated in the interface region of the organic semiconductor and accumulated charges can flow upon application of bias from the source to drain electrode. Conversely, when there is no accumulation of charges, there

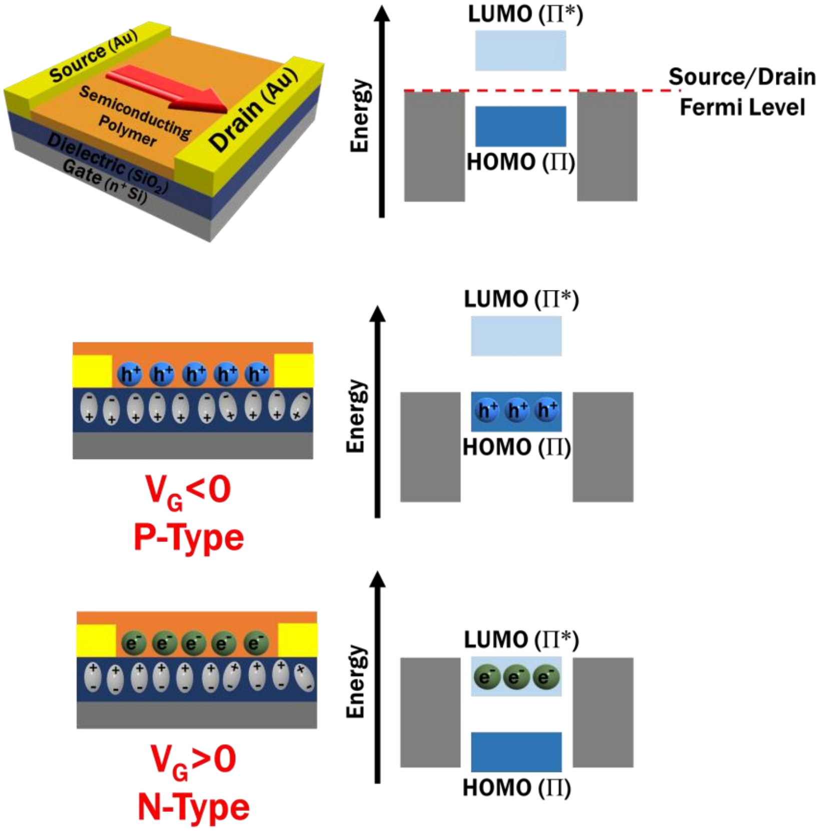

Figure 1.9 Band diagram and pictorial illustration about basic operation principles of bottom gate bottom contact OFET device.

will be no current from source to drain regardless how high a voltage is applied to source and drain electrode.

Figure 1.9 includes the band diagram illustrating the operating principle of the field effect transistor. The gate dielectric layer separates the gate electrode from the organic semiconductor. OFETs are operated in the accumulation mode of transistor operation whereby, the application of an electric field between the gate and organic semiconductors attracts charge carriers into a very thin region at the interface between the semiconductor and the dielectric. These accumulated charge carriers are responsible for the shift of HOMO and LUMO at the dielectric interface. Application of a negative gate bias causes the HOMO and LUMO levels to shift up such that the HOMO becomes resonant with the contact to the Fermi levels and electrons thus spill out of the organic semiconductor into the contacts, leaving behind holes in the channel region, which become mobile and flow under the application of a negative drain bias. In the case of a positive gate bias application, accumulated electrons at the interface shift the HOMO and LUMO energy levels down. Then, electrons can be injected into the LUMO energy level of the semiconductor from the Fermi level of the source and drain electrode so that electrons can be transported when positive bias is applied from source to drain. So, depending on the intrinsic charge carrier transport characteristics of the semiconducting material, operation should be carefully managed. For a P-channel material based device where hole transport is dominant, a negative gate bias should be applied to operate the device.

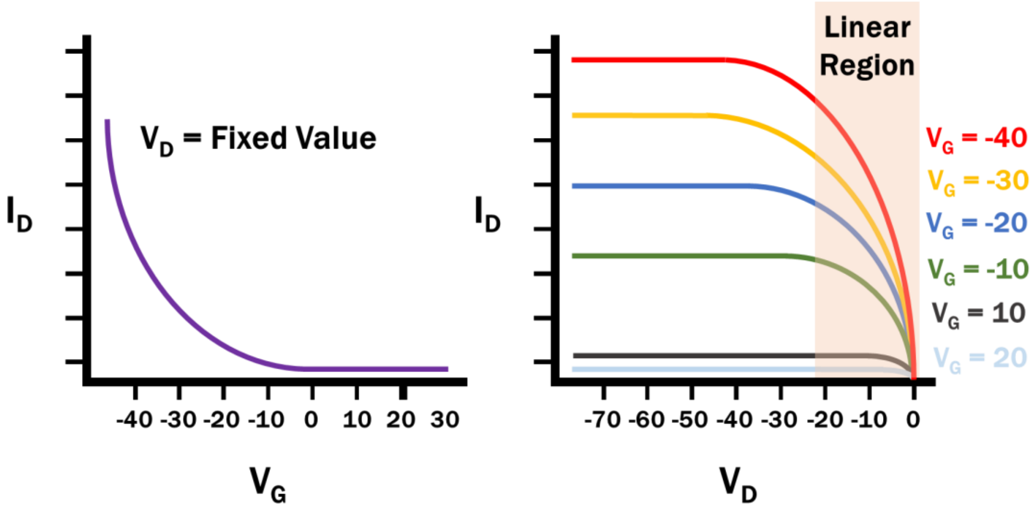

Figure 1.10 Representative transfer curve (I_D-V_G) and output curve (I_D-V_D) of common OFET devices.

Through operation of the OFET device, charge carrier transport characteristics within the active semiconducting layer can be extracted. Important parameters representing the charge carrier transport characteristics of organic semiconducting active layers are charge carrier mobility, threshold voltage, and on-off ratio. To characterize the device, two different methods to measure the devices are required. One measurement acquires multiple drain current (I_D) versus drain voltage (V_D) curves with varied gate voltage (V_G) and these curves are referred to as output curves. Another way measures I_D versus V_G with fixed V_D. The I_D-V_G curve obtained from operation is commonly referred to as a transfer curve. From the output curves of an OFET device, the boundary between the linear and saturation regions of device operation can be determined. Ideally, charge should be accumulated in the semiconducting layer once non-zero V_G is applied. However, due to various reasons, in most of cases V_G of a certain amount should be applied for charge accumulation. For example, presence of deep charge traps or band bending provoked by mismatch between semiconductor HOMO or LUMO and the electrode Fermi level requires non-zero extra voltage to accumulate conductible charge carriers within the semiconductor layer. This necessary voltage to turn on the OFET device is referred to as the threshold voltage (V_T).

An OFET device operates in the linear region when (V_G-V_T) >>V_D. During linear region operation, the charge concentration profile is uniform throughout source to drain. Bias applied from the source to drain is not large enough to generate a gradient of accumulated charges. Accordingly, I_D and V_D shows linear positive correlation in the linear region of operation. For charge carrier mobility calculations in the linear region, *Equation 1.1* can be used.

$$\mu_{Lin} = \left(\frac{L}{WV_DC_{OX}}\right)\left(\left.\frac{\partial I_D}{\partial V_G}\right|_{V_D}\right) \qquad \textit{Equation 1.1}$$

Where L and W are length and width of channel, V_D is drain voltage used during I_D-V_G operation, C_{OX} is capacitance of dielectric layer.

When (V_G-V_T) < V_D, the OFET device operates in the saturation region where V_D is large enough to induce a gradient of charges accumulated by (V_G-V_T) and I_D does not change as V_D changes. In this case, *Equation 1.2* should be used for the calculation of mobility from the transfer curve.

$$\mu_{Sat} = \left(\frac{2L}{WC_{OX}}\right)\left(\left.\frac{\partial \sqrt{I_D}}{\partial V_G}\right|_{V_D}\right)^2 \qquad \textit{Equation 1.2}$$

1.3 Solubility Parameters and Molecular Interactions[38–45]

Based on fundamental understanding of the charge transport mechanism within organic semiconductor materials, it can be concluded that organizing organic semiconductor molecules into ordered structures is essential to overcome inferior charge transport limited by intrinsic disorder. Once molecules are well packed together, more efficient intermolecular charge transport can take place. Organic semiconductor molecules are processed from solution. In solution state, ordering of organic semiconductor molecules is closely related to interaction between solute (organic semiconductor) and solvent and can be easily coupled with solubility of the solute. If solvent-solute interactions are stronger than solute-solute interactions, solute molecules are more likely to associate with solvent molecules rather than pack together to form ordered moieties. In this case, the solute is said ‘soluble’ with respect to the solvent. Conversely, when a solute-solute interaction is stronger, the molecules will pack together easily without interruption, and the solute will precipitate out of solution. So, molecular interactions amongst components in solution can be easily determined by examining their solubilities. However, as the term ‘solubility’ is too vague to be effectively utilized, in this thesis, Hansen solubility parameters will be adopted to quantify and understand molecular interactions between molecules.

1.3.1 Hildebrand Solubility Parameter

Hansen solubility parameters are a detailed, partitioned version of the classic Hildebrand solubility parameter. Thus, understanding the thermodynamic background behind the Hildebrand solubility parameter will be helpful to understand the concept of Hansen solubility parameters.[43,44]

Hildebrand used cohesive energy density to explain solubility. By measuring the energy required for vaporization, the total energy of bonds holding liquid molecules together can be directly measured. Hildebrand solubility parameter is defined by the following equation.

$$\delta^2 = \frac{\Delta E_{vap}}{V_M} \text{ (cal/cm}^3\text{)} \qquad \textit{Equation 1.3}$$

ΔE_{vap} is energy of vaporization and V_M is molar volume.

Gibbs Free Energy of mixing should be less than zero for spontaneous mixing.

$$\Delta G^M = \Delta H^M - T\Delta S^M \qquad \textit{Equation 1.4}$$

ΔG^M is free energy of mixing, ΔH^M is heat of mixing, T is temperature, and ΔS^M is entropy change in mixing process.

Hildebrand related heat of mixing is equal to the vaporization energy change in mixing and thus, a direct relationship between solubility parameters and Gibbs Free Energy of mixing can be obtained.

$$\Delta H^M \approx \Delta E^M = \emptyset_1 \emptyset_2 V_{M.avg}(\delta_1 - \delta_2)^2 \qquad \textit{Equation 1.5}$$

ΔE^M is vaporization energy change in mixing, $V_{M.avg}$ is average molar volume and Φ is volume fraction.

From *Equation 1.4* and *1.5*, we can conclude that the minimum difference between solubility parameters, δ_1 and δ_2, that makes ΔE^M ($\sim \Delta H^M$) equal to or less than $T\Delta S^M$ is required to make mixing spontaneous ($\Delta G^M < 0$). Finally, the method to calculate entropy of mixing is outlined below.

As we are dealing with a polymer solution, the Flory-Huggins equation can be used to calculate entropy of mixing. Flory-Huggins solution theory is based on dissymmetry in molecule size of a relatively long polymer chain and solvent. By making the assumption that one solvent molecule occupies one lattice site and one polymer chain occupies ‘x’ lattice sites, the following equation of entropy of mixing can be derived.

$$\Delta S^M = -R[n_1 ln\emptyset_1 + n_2 ln\emptyset_2] \qquad \textit{Equation 1.6}$$

R is the universal gas constant, n is the number of moles, and Φ is the volume fraction.

1.3.2 Hansen Solubility Parameters

Based on the Hildebrand solubility parameter, Hansen solubility parameters divided the combined molecular interactions (Cohesion energy) used for the Hildebrand solubility parameter into three significant interactions: nonpolar dispersion interaction (D), permanent dipole-permanent dipole interaction (P), and hydrogen bonding (H). So, the total cohesion energy can be written as a combination of D, P, and H.

$$\Delta E_v = \Delta E_D + \Delta E_P + \Delta E_H \qquad \textit{Equation 1.7}$$

By dividing both sides with molar volume V_M, we can conclude that

$$\delta^2 = \delta_D^2 + \delta_P^2 + \delta_H^2 \text{ (cal/cm}^3\text{)} \qquad \textit{Equation 1.8}$$

So, solubility parameters of materials can be expressed as a designated point in a 3D space of D, P, and H axes.

As previously discussed, solubility between two materials can be directly related to the difference between Hildebrand solubility parameters of materials. (*Equation 1.5*) Hansen solubility parameters which are derived from the Hildebrand solubility parameter follow the same analogy. So, solubility can be defined by the distance between two points in the 3D space of Hansen solubility parameters on the D, P and H axes. Farther distance can be interpreted as poorer solubility. This distance is quantified as the radius of interaction (R_A), but a factor of 4 is used for the dispersion interaction term for optimal fitting.

$$R_A = 4(\delta_{D1} - \delta_{D2})^2 + (\delta_{P1} - \delta_{P2})^2 + (\delta_{D1} - \delta_{D2})^2 \qquad \textit{Equation 1.9}$$

1.3.3 Measurement of Hansen solubility parameters and Hansen solubility sphere

Determination of Hansen solubility parameters greatly depends on the availability of data. Hansen published the original set of data including solubility of 90 organic solvents for 32 polymers in 1967. He started with saturated aliphatic hydrocarbons whose cohesion energy is heavily dominated by dispersion interactions. Hildebrand solubility parameters can be easily calculated by measuring the vaporization energy. In the case of aliphatic hydrocarbons, the measured Hildebrand parameter can be solely translated as the dispersion parameter. With base data of saturated aliphatic hydrocarbons as a starting point, Hansen adopted the theoretical calculation methodology outlined by Blanks and Prausnitz[46] to determine solubility parameters of other solvents. Hansen did rigorous fitting to satisfy actual polymer-solvent solubility experimental results. For over 40 years, Hansen's original work has been revised and supplemented by many experimental results and theoretical calculations adopting group contribution methodology. Today, software (HSPiP) which includes a tremendous number of tested Hansen solubility parameters is available. Using poly(3-hexylthiophene) (P3HT), a well-known semiconducting polymer, as an example, we are going to briefly cover how to find Hansen solubility parameters using HSPiP, a commercially available program. HSPiP includes huge database of HSPs and its own optimization algorithm.

First, solubility between P3HT and arrays of solvents with known Hansen solubility parameters should be tested. As HSPs are based on thermodynamic rules, judgment is made in only two ways; mixed ($\triangle G^M < 0$) or not mixed ($\triangle G^M > 0$). So, criteria defining mixing status should be smartly designed to obtain meaningful and useful HSPs result. As our goal is to utilize solubility parameters to investigate molecular interactions between P3HT and other materials, the color change of the solution is considered to work best as a judging parameter. An observed color change of a conjugated polymer solution indicates a change in the optical band gap initiated from ordered P3HT molecules induced via interactions with surrounding molecules. Change of transparency was also checked to follow molecular interaction driven P3HT mesoscale assembly. Mesoscale P3HT structures are large enough to scatter light. Transparent, orange colored P3HT solution was made by heating the solvent-solute mixture. Then, the solution was cooled to room temperature and aged for 1 hr. When there was no change in color or transparency after this procedure, the solvent used was classified as a 'good' solvent, while all others were marked as 'poor' solvents. By inserting the experimental data into the HSPiP software, fitting is done automatically in a way that "optimal" Hansen solubility parameters for the P3HT polymer and the minimum radius (R_0) only including 'good' solvents are calculated. Based on R_0 as the sphere radius and Hansen solubility parameters of P3HT as center point in 3D space, the Hansen solubility sphere for P3HT can be formulated. Any points within the sphere can be said to have good solubility relative to P3HT. This can be quantified as the relative energy difference (RED). RED is calculated by dividing R_A by R_0. When RED is less than 1, a given solvent is defined as 'good'. A larger RED predicts that P3HT will be less soluble in that system.

1.4 Material: Poly(3-Hexylthiophene)

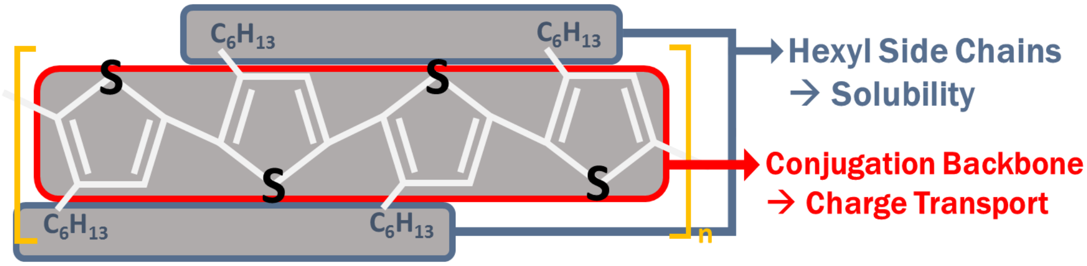

Figure 1.11-a Chemical structure of P3HT and function of individual components.

Poly(3-Hexylthiophene) (P3HT) is one of the earliest conjugated materials that have served as excellent model materials to understand the nature of charge transport in disordered organic semiconductors. In this thesis, P3HT will be used as a model material to study the assembly behavior of conjugated semiconducting materials and applications. P3HT consists of two main parts; insoluble thiophene conjugated backbone where charges are transported and hexyl side chains attached to thiophene backbone that impart solubility to the polymer system.

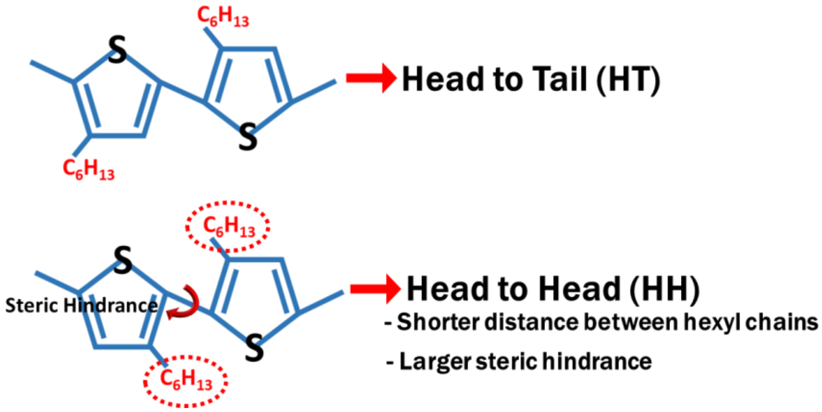

Figure 1.11-b HH and HT configuration of P3HT and pictorial explanation about intrinsic cause of ring torsion.

The alkyl substituents can be incorporated into a polymer chain with two types of arrangements, either head-to-tail (HT) or head-to-head (HH). A polymer with predominantly HT linkages is referred to as regioregular and percentage of HT configuration is marked as ‘regioregularity’ of the material. Regioregularity has a profound impact on charge transport in these materials. Higher regioregular P3HT has better ordering and crystallinity in the solid state because it experiences less steric hindrance provoked by the HH configuration of neighboring hexyl side chains. Steric hindrance causes ring torsion, thus inhibiting effective π-stacking among molecules. In the early stage of introduction, a field effect mobility of P3HT with low regioregularity is on the order of 10^{-5} $cm^2V^{-1}s^{-1}$. Highly regioregular P3HT (>95% HT regioregularity), commercially available today, is known to provide FET mobilities ranging from 10^{-3} to 10^{-2} $cm^2V^{-1}s^{-1}$.

CHAPTER 2

CONTROLLED ASSEMBLY OF POLY(3-HEXYLTHIOPHENE): MANAGING THE DISORDER TO ORDER TRANSITION ON THE NANO- THROUGH MESO-SCALES

2.1. Introduction

As strong candidates expected to enable practical applications in low-cost, flexible electronics, solution processible conjugated organic semiconducting materials have garnered much attention over the past decade. However, the inherently inferior charge carrier transport performance of organic semiconductors has led to a multitude of efforts focused on enhancing their transport properties.[4,5,19,47] These efforts have largely concentrated on the design and synthesis of alternative structures.[16,17,48] More recently, attention has turned to improving electronic performance via design and control of solution processing techniques. Methods focused on inducing ordering/crystallization of conjugated materials have effected significant performance improvements and are gaining traction due to their simplicity.[49–53] However, to date, most research related to crystallization of organic materials through solution processing methods has been confined to conjugated small molecules which are more easily crystallized than polymeric alternatives.[6,7,54] While recent reports have presented processing methods to induce semiconducting polymer ordering,[55,56] inquiries into underlying mechanisms are limited, even though discernment of the self-assembly process is critically important.

In this chapter, we systematically interpret and elicit control of the regio-regular poly(3-hexylthiophene) (P3HT) self-assembly process based on a 2-step crystallization model consisting of nucleation and growth steps. Starting from the demonstration of controlled P3HT molecular assembly into polycrystalline rod-like P3HT nanostructures with varied length, it is shown that the synergistic combination of ultrasonic irradiation and non-solvent addition[57,58] leads to molecular self-assembly of P3HT into rod-like polycrystalline meso-scale architectures through simple 2-step crystallization principles. Though commonplace in the crystallization community,[59–62] 2-step crystallization has yet to be introduced to analyze conjugated polymer ordering into nanostructured assemblies. Application of 2-step crystallization principles may provide a comprehensive platform for analysis and discussion of conjugated polymer self-assembly into polycrystalline moieties that have favorable charge transport characteristics.

Adventitious control of self-assembled P3HT nanostructures effects notable improvement in P3HT charge carrier mobility values up to 0.103±0.009 cm^2/V-s, vs. 0.025±0.007 cm^2/V-s for untreated samples were obtained. Through careful analysis of x-ray diffraction, UV-vis, and atomic force microcopy (AFM) morphological data, the important interplay between molecular level interactions and long range order for effective macro-scale charge carrier transport is articulated.

2.2 Result and Discussions

2.2.1 Controlled Assembly of P3HT Nanorods

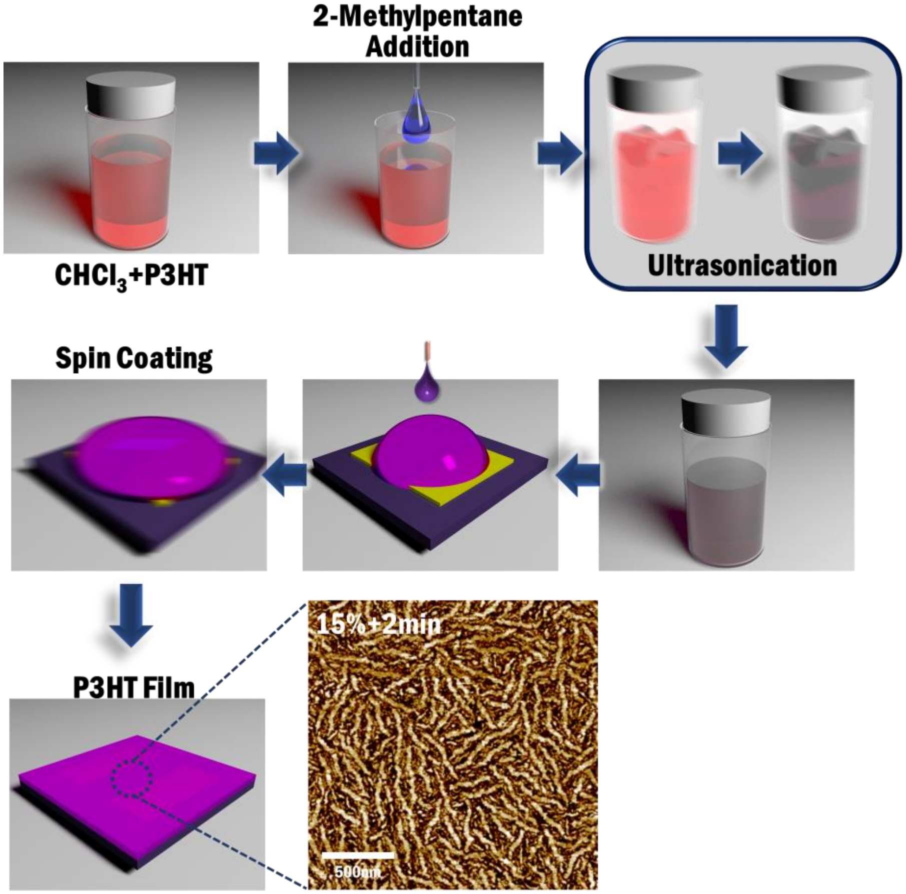

Figure 2.1 A schematic illustration of P3HT nanorod preparation through a combined ultrasonication/non-solvent addition approach.

The process used to induce controlled P3HT self-assembly into nanorod structures is depicted in **Figure 2.1**. Addition of non-solvent is well known to give significant effect on molecular assembly of organic conjugated material in solution state by modulating solubility of entire solvent system. For example, it is easy to anticipate that solution consisted of 80 % of good solvent and 20 % of non-solvent will dissolve more amount of solute compared to the solution with 50 % good solvent and 50 % non-solvent. In this study, Chloroform and 2-methylpentane were carefully chosen as the solvent and non-solvent, respectively: their boiling points are similar (2-methylpentane, bp 61 ° C; chloroform, bp 62 °C) and the two solvents do not significantly interact (*e.g.* hydrogen

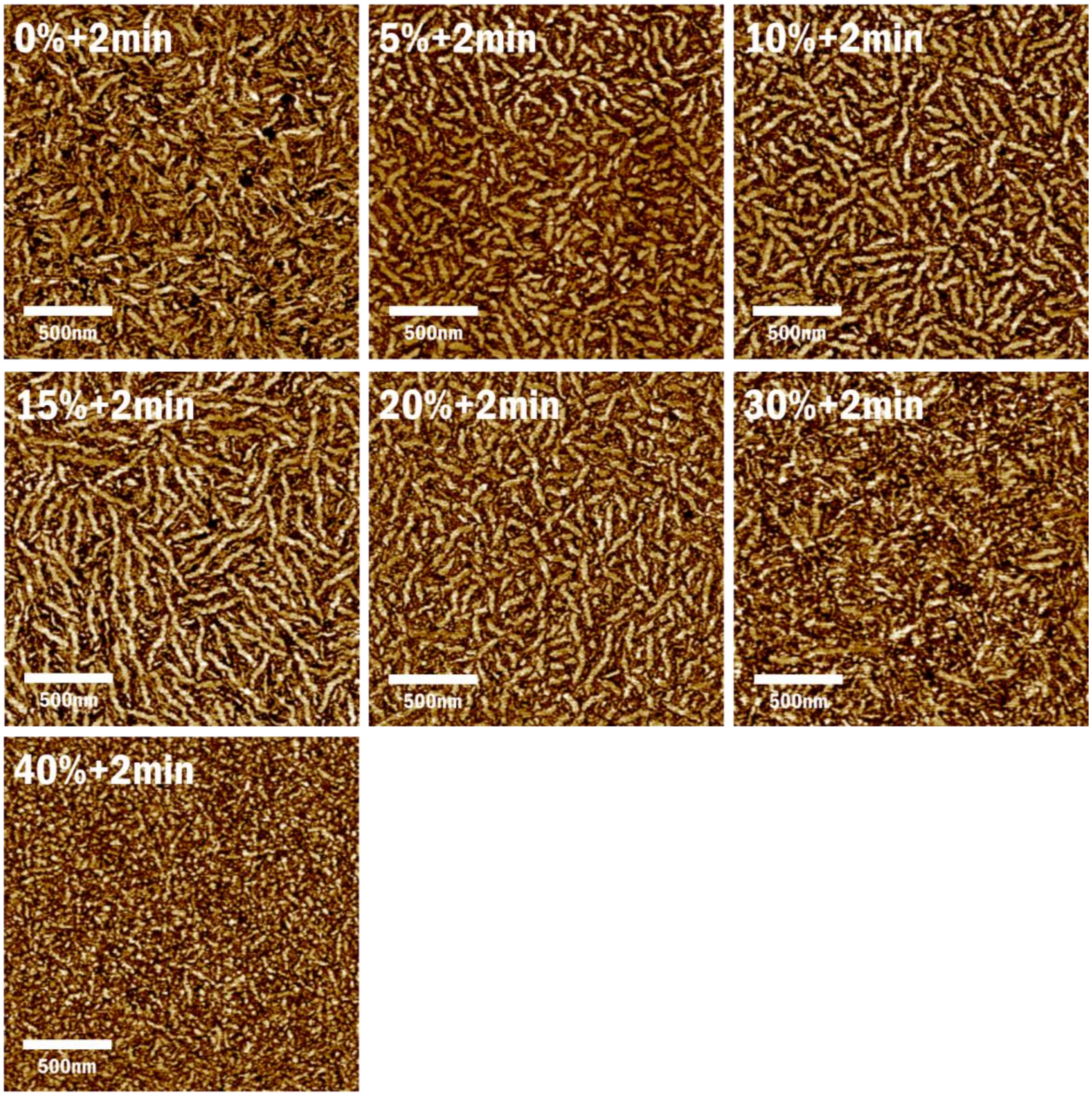

Figure 2.2 Tapping mode AFM phase images of P3HT films obtained by spin coating choloroform-P3HT solutions with varying proportions of non-solvent (2-methylpentane) followed by ultrasonication for 2min.

bonding) with each other. Thus, 2-methylpentane addition alters P3HT solubility, but has no impact on overall solvent volatility, one factor known to impact P3HT self-assembly during film formation.[63]

First, known amounts of 2-methylpentane were added to a P3HT/chloroform solution. This sequence facilitated selective control of solution solubility. After addition of poor solvent, the resultant P3HT solution was mediated by ultrasonic irradiation using a common bath type ultrasonicator. Ultrasonication is known to induce P3HT self-assembly with no change in molecular structure.[57,64] Finally, P3HT thin-films were fabricated from the corresponding solutions via spin coating. As discerned from atomic force microscopy (AFM) phase images (**Figure 2.2**), this step-wise methodology effected P3HT self-assembly into rod-like nanostructures whose dimensions could be modulated by varying the proportion of non-solvent.

For a fixed sonication time, solvent composition regulated final P3HT nanorod dimensions. Upon addition of 0 to 15 vol. % 2-methlypentane, nanorod length was significantly elongated from ~140 nm to ~360 nm, while further increases in the proportion of non-solvent led to drastic shortening of the assemblies. Average length of assembled nanorods was estimated from AFM images using image analysis program. Details regarding methodology are described in the experimental section.

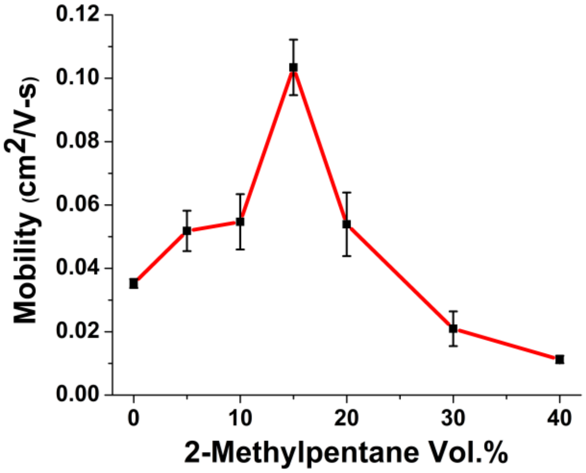

Figure 2.3-a Average field-effect mobilities of P3HT thin-films spin coated from Chloroform-P3HT solution with corresponding proportion of 2-methylpentane followed by 2min of ultrasonication. Mobilities were calculated in the linear regime of operation with V_{DS} = -3 V.

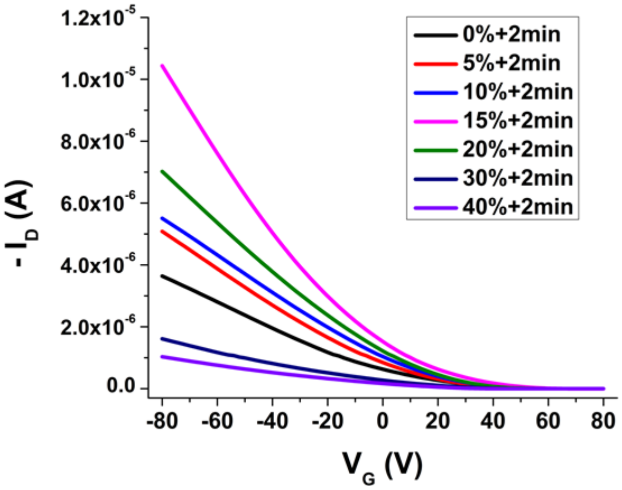

Figure 2.3-b Transfer characteristics of OFET devices fabricated with corresponding P3HT solution.

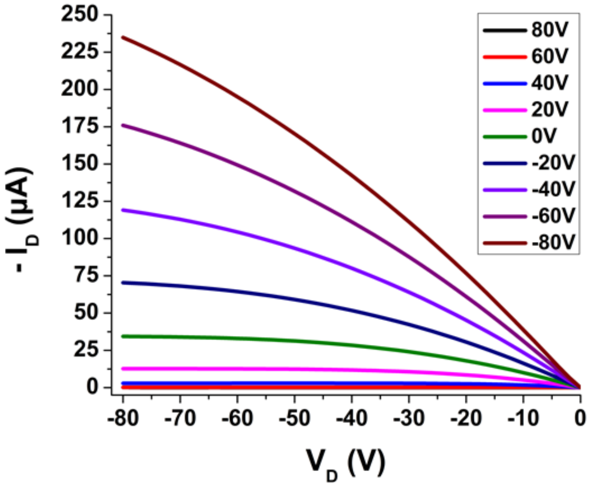

Figure 2.3-c Output characteristics for OFET devices fabricated with Chloroform-P3HT solution treated with 15 vol. % 2-methylpentane and 2 min ultrasonication.

As discerned from bottom gate, bottom contact organic field effect transistor (OFET) studies, P3HT charge carrier mobility increased gradually as a function of nanorod length. All the devices exhibited common OFET operation characteristic and representative device characteristic curves are presented below (**Figure 2.3-b, c**). Devices fabricated from ultrasonicated P3HT solution with 15 vol. % 2-methylpentaneaffords the longest P3HT nanorod assemblies and exhibited the highest average mobility, 0.103 cm^2/V-s, a value that is notably higher than that obtained for pristine P3HT films not subject to the added treatments (**Figure 2.3-a**). As nanorod length increased, mobility increased steeply. Presumably, films composed of a significant number of short assemblies leads to an increased number of boundaries between the more crystalline nanorods and amorphous-like matrix which serves to increase points of resistance impeding efficient charge transport.[65–67]

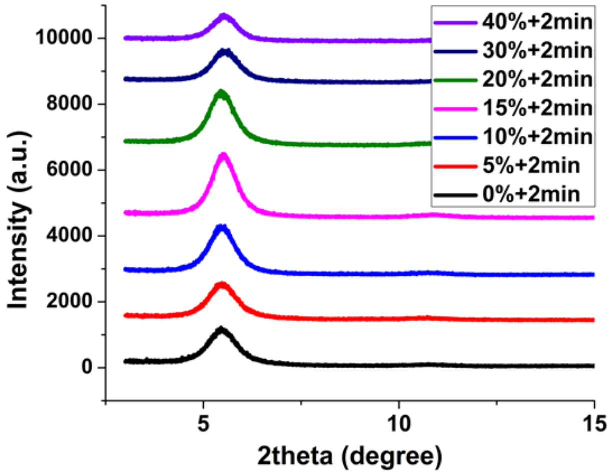

Figure 2.4-a Out-of-plane grazing incidence x-ray diffraction measurements for P3HT thin-films fabricated from chloroform-P3HT solutions with varied proportions of 2-methylpentane and a fixed 2 min ultrasonication time

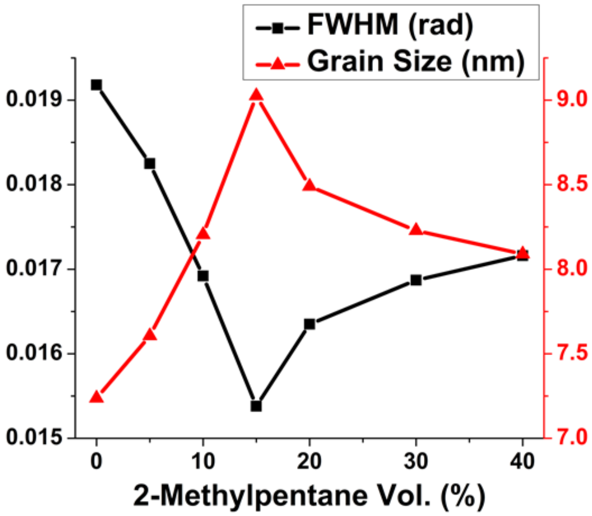

Figure 2.4-b Full width half max values of corresponding GIXRD profiles and calculated crystallite size.

Grazing incidence X-ray diffraction (GIXRD) results provide insight into nanorod crystallite packing (**Figure 2.4-a, b**). The full width half max (FWHM) of the (100) peak corresponding to lamellar packing of P3HT chains was analyzed, and the average crystallite size was calculated using the Scherrer equation.[68] Previous studies reported that pristine P3HT films are amorphous and show no (100) peak development,[57,69] and thus, the P3HT (100) FWHM is representative of crystallite size, where crystallites are presumed to consist of polymer nanorods. Significantly, crystallite size followed a trend similar to that of nanorod length; for up to 15 vol. % 2-methylpentane where nanorod length was observed to increase, crystallite size also increased. Further increases in non-solvent concentration led to a decrease in grain size, accompanied by an observed decrease in nanorod length. Given the direct correlation between nanorod length and thin-film crystallinity, it is extrapolated that the polymer nanorod assemblies are crystalline features, whereby crystallite size is proportional to nanorod length.

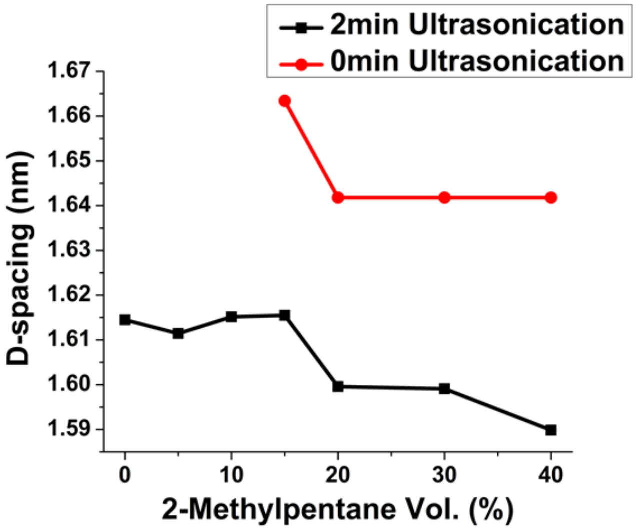

Figure 2.4-c (100) d-spacing values as a function of 2-methylpetane vol. % (fixed 2 min ultrasonication time) calculated from corresponding GIXRD data.

Comparison between films fabricated from solutions treated with and without ultrasonication showed significant difference in (100) d-spacing (spacing in lamellar packing direction), which clearly represents superior quality of molecular packing in P3HT nanorods fabricated through ultrasonication. Among samples from varied solubility and fixed ultrasonication time, there was a decreasing trend of (100) d-spacing as a function of poor solvent content.

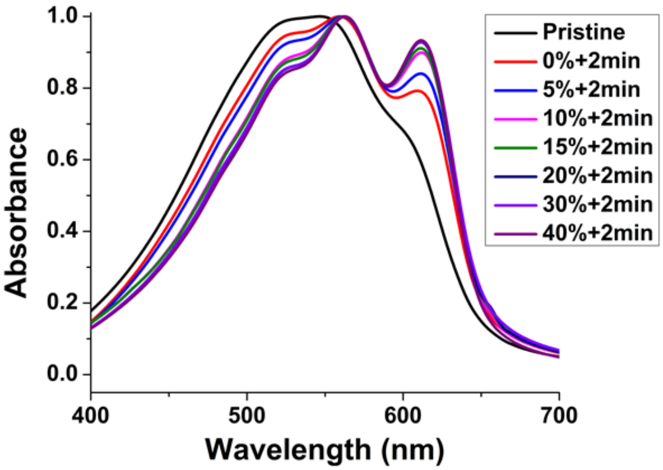

Figure 2.5-a Normailized UV-Vis absorption spectra of films fabricated from chloroform-P3HT solution with varied proportion of non-solvent (2-methylpentane) treated by ultrasonication for 2min.

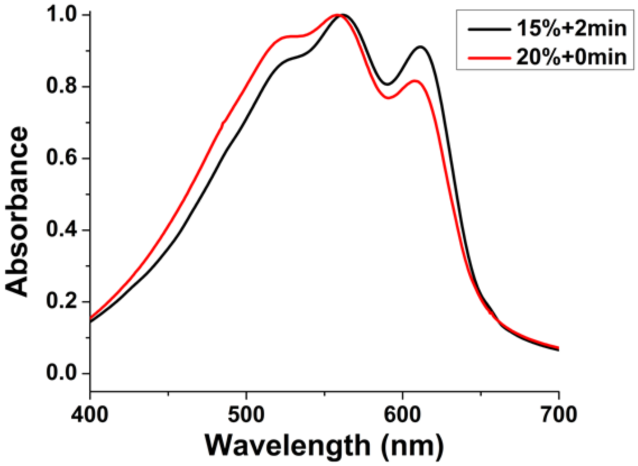

Figure 2.5-b Normailized UV-Vis absorption spectra of films fabricated from chloroform-P3HT solution with 15 vol. % 2-methylpentane treated by 2 min ultrasonication and with 20 vol. % 2-methylpentane.

From UV-vis spectroscopic data (**Figure 2.5-a**), the absorption band near 620 nm became more prominent, while that at about 550 nm representing the π-π* transition underwent a bathochromic shift as a function of 2-methylpentane volume fraction, indicative of enhanced intra- and inter-molecular interactions among P3HT chains.[70–73] The spectra continued to evolve with increased 2-methylpentane volume fraction up to 40 vol. %, where the system comprised very short P3HT nanorod-like structures. The data suggest that very short structures fabricated from 2 min ultrasonicated solutions containing 30 and 40 vol. % 2-mehtylpentane exhibit stronger intra- and inter-molecular interactions than much longer P3HT nanorods assembled in 15 vol. % 2-methylpentane solutions with 2 min ultrasonication (**Figure 2.5-b**).

While the UV-vis spectroscopic results suggest that the P3HT thin-films prepared from ultrasonicated solutions having a high volume fraction of non-solvent enjoy stronger molecular scale interactions, those interactions alone do not guarantee assembly of the nanostructures into longer, ordered, meso-scale constructs necessary for effective macroscale charge carrier transport. Coupled with electronic performance, GIXRD and UV-vis analysis underscores the importance of optimal nanostructure growth conditions. Within individual small meso-scale structures fabricated in ultrasonicated, high non-solvent content solutions, charge carrier transport may well be more effective due to stronger molecular-scale interactions than those found in the longer nanorod assemblies.[74–76] However, macroscale charge carrier mobility is significantly higher when the films comprise longer nanorods with somewhat weaker molecular level interactions. Unambiguously, long range order plays a significant role in defining semiconducting polymer transport characteristics, and is perhaps more important than molecular level interactions for efficient macroscopic charge carrier transport.

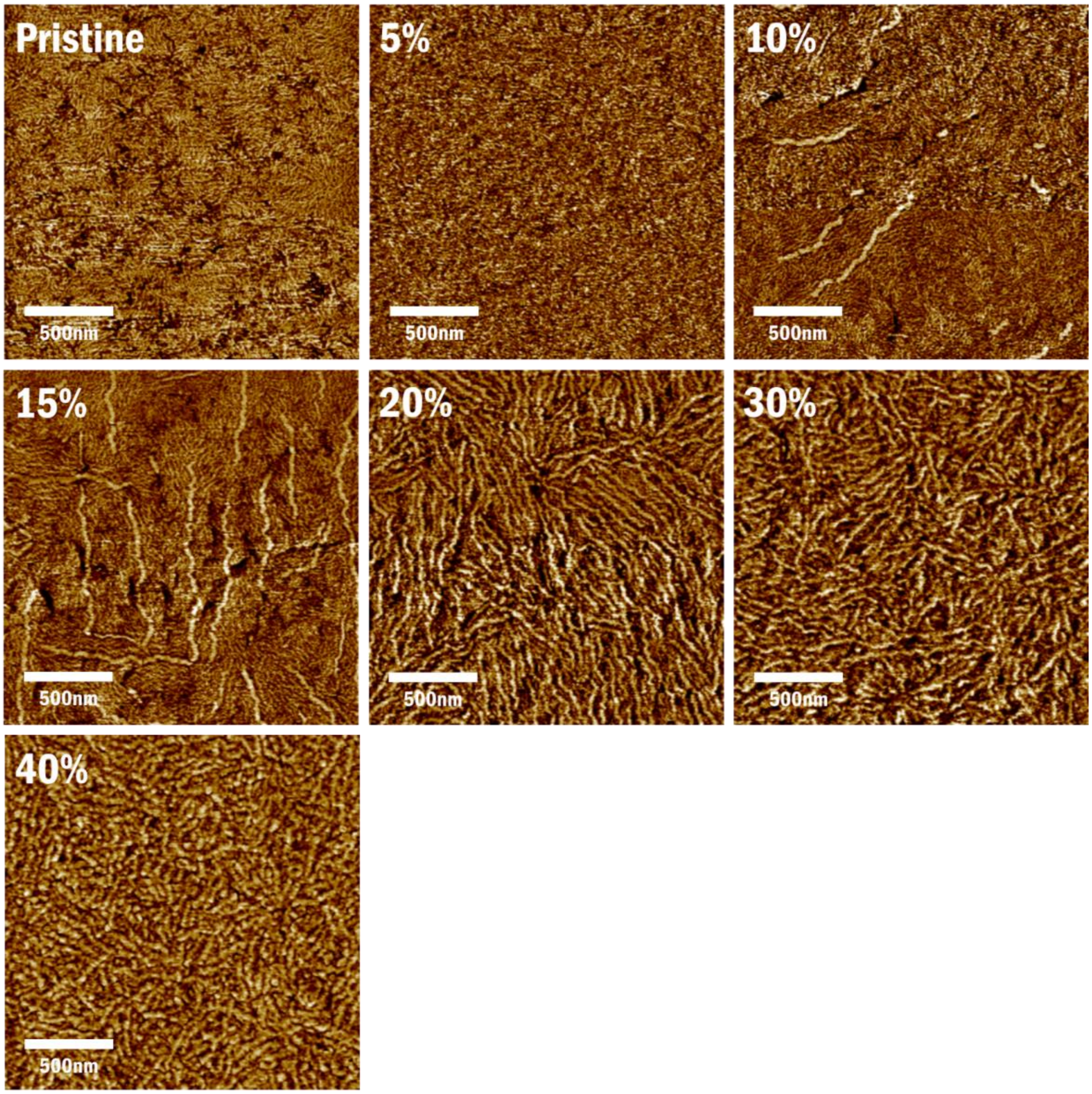

Figure 2.6 Tapping mode AFM images of P3HT thin films prepared via spin coating from $CHCl_3$ solution with defined proportions of 2-methylpentane

The influence of molecular level interactions on charge carrier transport properties should not however, be disregarded. **Figure 2.6** demonstrates that nanostructures with similar or slightly longer lengths can be created by modulating system solubility. P3HT nanostructures prepared through addition of 15 vol. % 2-methylpentane coupled with 2min ultrasonication (**Figure 2.2**) and nanostructures assembled via 20 % 2-

methylpentane addition alone (**Figure 2.6**) have almost identical length, thus suggesting a similar degree of charge transport resistance through boundaries between more crystalline nanorods and amorphous domains for both films. However, the hole mobility exhibited by devices fabricated from solutions prepared via addition of 20 % 2-methylpentane was only 0.042±0.005 cm^2/V-s, a value less than half that observed for films prepared by the synergistic solvent modulation/ultrasonication approach.

The large mobility gap observed for P3HT films comprising nanostructures with similar dimensions most likely derives from differences in their respective molecular level interactions. The intensity of the absorption band near 620 nm, indicative of the extent of molecular level interactions, is significantly more intense in the case where both solubility modulation and ultrasonication were employed. It is deduced that once P3HT self-assembles into nanorods with sufficient length to allow for long range order, molecular level interactions within individual meso-scale entities play a role in macro-scale charge transport. However, strong molecular level interactions in and of themselves, in the absence of concomitant long range order, cannot support efficient macroscopic charge transport. While both long range order and molecular level interactions are required for optimal charge carrier transport at the device level, each factor plays an important role, and both can be extrinsically influenced or tempered by a range of process variables for optimized transport. Here, solution characteristics and post-dissolution treatments such as ultrasonication were used to demonstrate the important relationship/tradeoff.

2.2.2 Mechanistic Elucidation of P3HT Molecular Assembly

To define optimum solution characteristics for explicit control of P3HT nanostructure dimensions, a mechanistical description of the self-assembly process is required. A 2-step crystallization model consisting of nucleation and growth steps is adopted to elucidate P3HT self-assembly. While established in other areas,[59–62] application of this model provides new insight into the crux of P3HT ordering/crystallization processes and significantly, similar processes that are generically operational in conjugated polymer systems.

The essential driving force for crystallization from solution relies on the degree of supersaturation.[59] In the meta-stable state, where a solution is moderately supersaturated (**Figure 2.7-a, b**), crystal growth is initiated from available nucleation sites. Within this meta-stable zone, crystal growth is favored over formation of nucleation sites. From the perspective of P3HT, polymer molecules would be consumed in crystal growth, which emanates from existing nucleation sites. In contrast to behavior within the meta-stable state, if the solution becomes further supersaturated it enters an unstable regime **(Figure 2.7-c)**, where nucleation dominates crystal growth, and most of the excess solute becomes subject to spontaneous nucleation.[59,77–79]

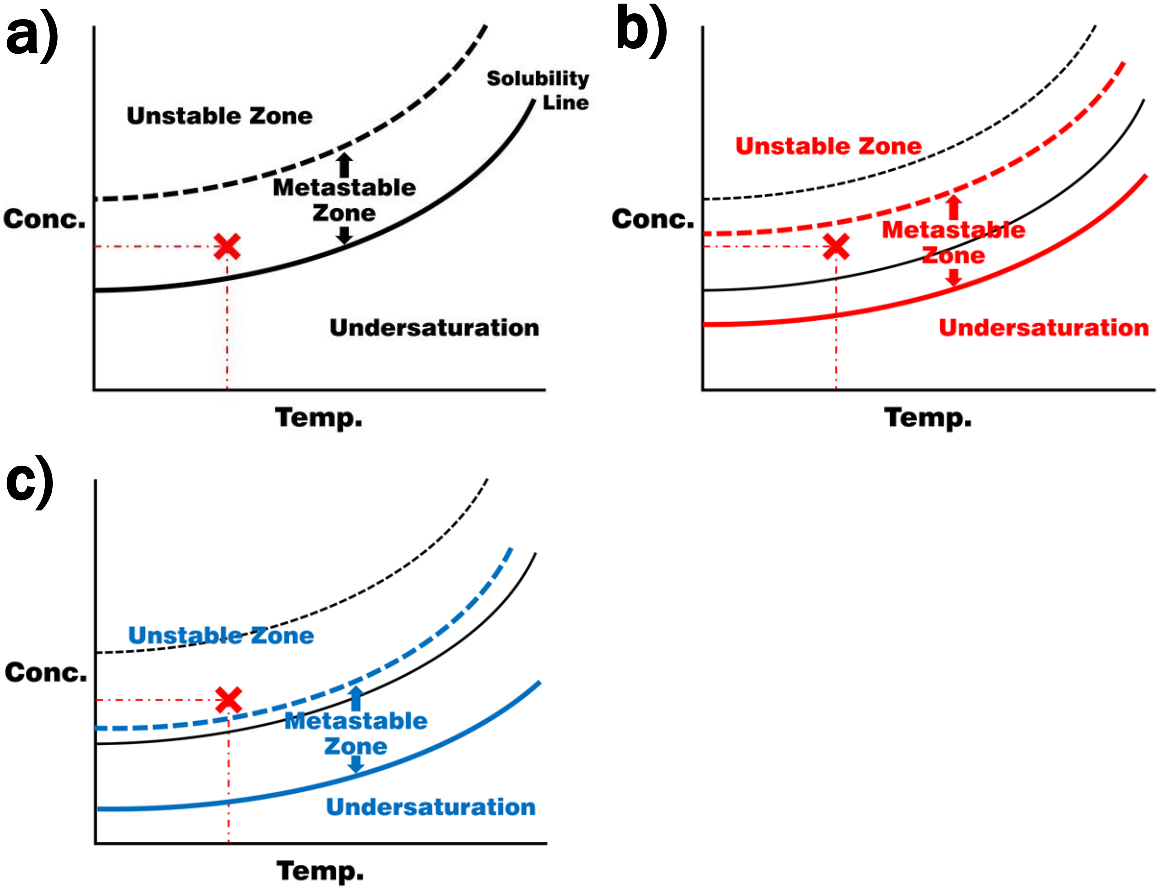

Figure 2.7-a~c Typical solubility curves depicting the meta-stable and unstable zone. The red X indicates a fixed value of solution temperature and concentration. a) Black lines represent the solubility curve for the solution under the initial moderately supersaturated conditions. b) The solubility curve of the solution after poor solvent addition is given in red lines. The red X resides in meta-stable zone. c) Further addition of poor solvent leads to conditions depicted with blue lines where the solution condition marked by red X enters the unstable zone.

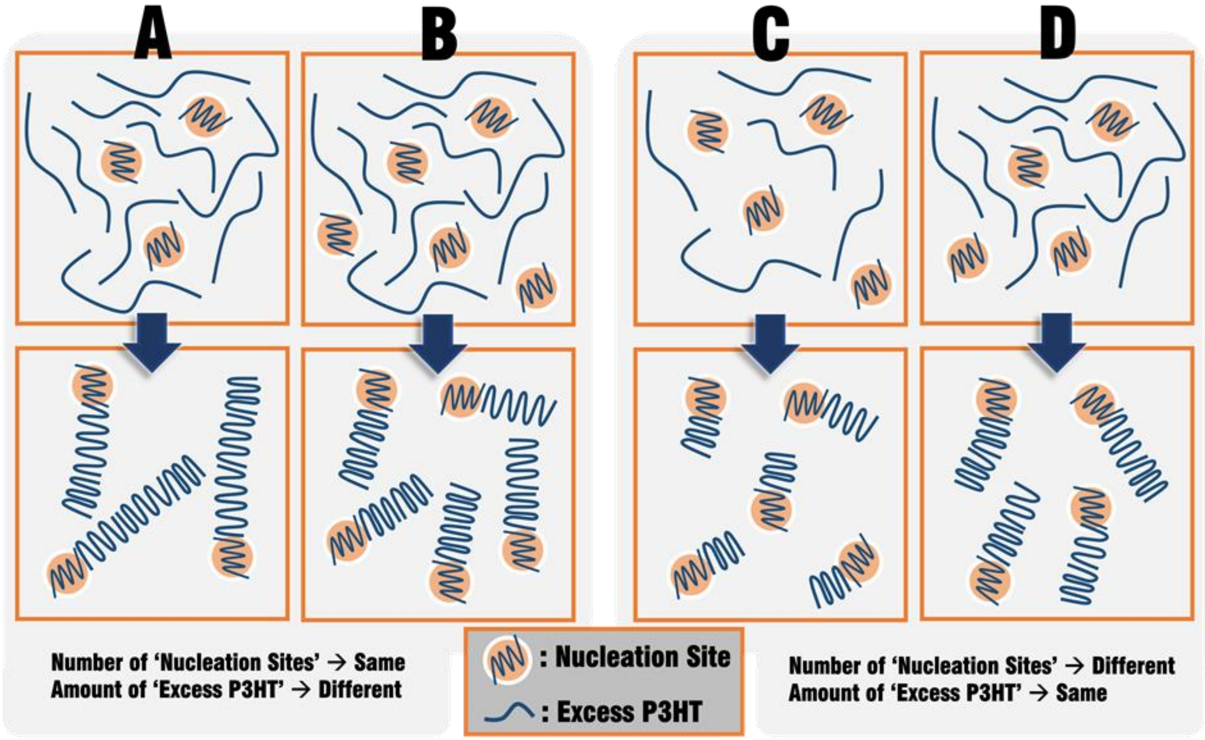

Figure 2.8 Schematic depicting four general cases of P3HT self-assembly based on the 2-step crystallization model.

Using the nucleation and growth crystallization model, **Figure 2.8** depicts four generic scenarios for P3HT nanorod assembly. Systems A and B have the identical number of P3HT chains available for ordering, though System B is comprised of more nucleation sites (seeds). Both are in same degree of supersaturation, however they differ in their respective fraction of nucleation sites. Applying the nucleation-growth model, formation of fewer yet longer nanorods is expected in system A vs. system B. Alternatively, systems C and D have the same number of nucleation sites but different quantities of available P3HT,. As a result, longer P3HT nanorods are expected to be assembled in system D.

The effects of non-solvent and ultrasonication must first be articulated separately. The AFM phase images of P3HT thin-films fabricated from solutions with varying proportions of 2-methylpentane (**Figure 2.6**) demonstrate the role and impact of non-solvent addition on P3HT nanorod formation. For up to 15 vol. % 2-methylpentane, there is obvious growth of P3HT nanorod assemblies reaching 760 nm in length with a gradual increase in the number of features from none to 15 counts, following anticipated crystallization behavior in the meta-stable zone where growth and nucleation are favored and suppressed, respectively. Increasing the non-solvent volume fraction above 15 vol. % results in formation of an abruptly larger number of P3HT nanorods with shorter length, indicating domination of nucleation over growth. Transition from 15 % to 20 % provokes steep increase in number of nanorod assembly from 15 to 176 counts accompanying decrease in length from 760 nm to 400 nm. In this region, the P3HT solution falls into the unstable region where excessive nucleation takes place, thus a large number of small features are formed, as per the example scenario of systems A vs B (**Figure 2.8**).

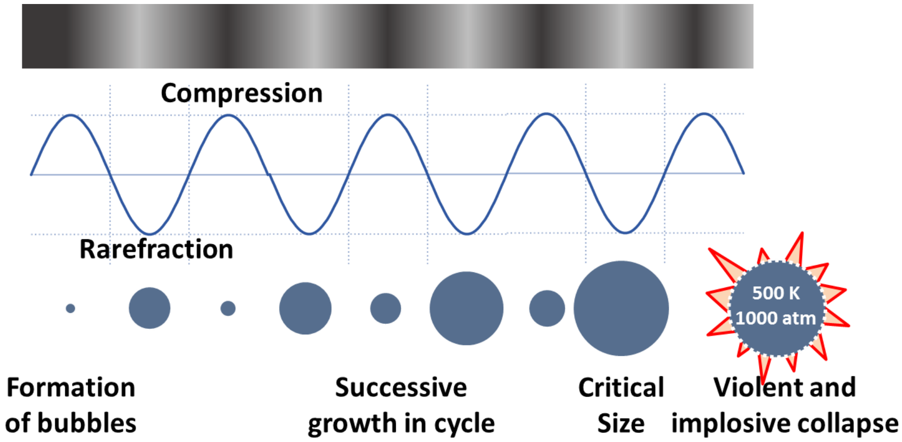

Figure 2.9 Scheme illustrating formation and collapse cycle of cavitation induced by ultrasound irradiation.

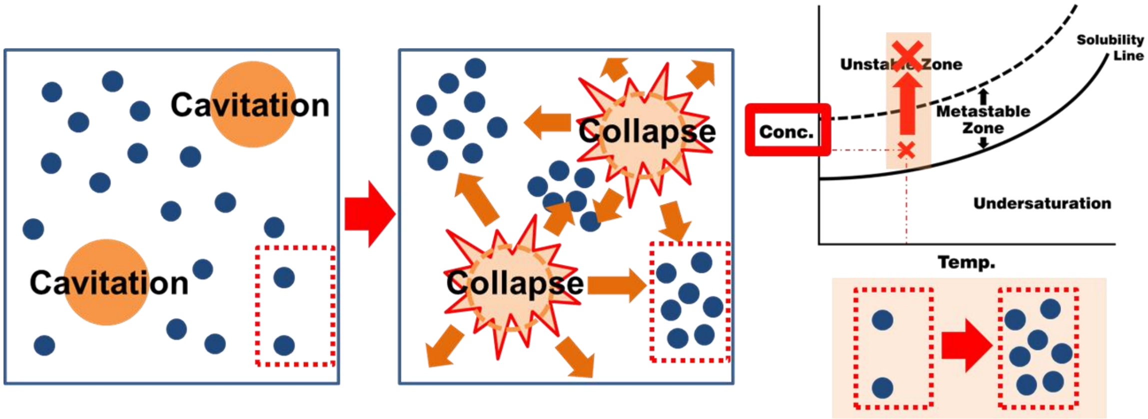

Figure 2.10 Scheme describing creation of nucleation induced by cavitation collapse.

Ultrasonication of a solution effects cavitation due to rapid expansion and compression of the liquid molecules in a process induced by the applied acoustic waves.[80,81] Microbubbles form and grow as the expansion and compression cycles are repeated, and finally collapse (**Figure 2.9**). When the microbubbles rupture, the surrounding liquid molecules near the microbubble wall experience very high pressure, which forces a localized portion of liquid near the microbubble to become highly supersaturated. As a result of this localized increased degree of supersaturation, nucleation sites are formed (**Figure 2.10**).[80–85]

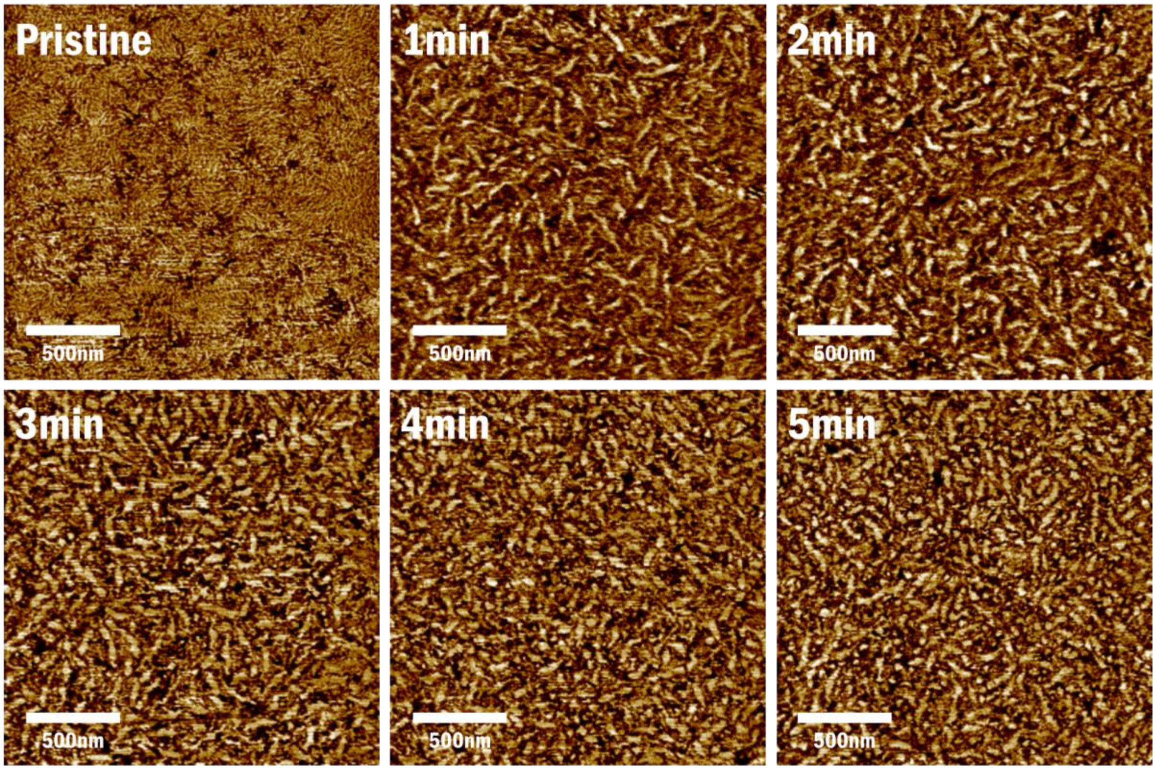

Figure 2.11 Tapping mode AFM images of P3HT thin films prepared via spin coating from $CHCl_3$ solution after ultrasonication for the indicated times.

Examination of AFM phase images of P3HT thin-films fabricated from chloroform solution with varied ultrasonication time (**Figure 2.11**), confirms this phenomenon. As ultrasonication time increases, the number of small nanorods gradually increases as a result of an increased number of nucleation sites. Within 2 um by 2 um AFM image, nanorods count grows from 178 to 350 when ultrasonication time varies from 1 min to 5 min. The size of nanorods fabricated via ultrasonication is relatively small, because without poor solvent mediation, the pristine P3HT-chloroform solution does not have a high degree of supersaturation and availability of excess solute is insufficient for further growth. Thus, through ultrasonic irradiation, the formation of nucleation sites for P3HT nanorod assembly can be promoted and controlled. On the other hand, 2-methylpentane addition provides a means to control the degree of supersaturation. Solubility modulation within the meta-stable zone stimulates nanorod growth, while extreme modulation of solubility forces the solution into the unstable regime and triggers spontaneous nucleation.

The 2-step crystallization model can be applied to P3HT self-assembly via sequential non-solvent addition and ultrasonication by revisiting **Figure 2.2**. Ultrasonication of P3HT-chloroform for 1~3 min promotes a degree of nucleation that is well balanced for subsequent growth. However, P3HT in pristine chloroform solution is in a low degree of supersaturation, and the conjugated polymer experiences only limited growth into small nanostructured assemblies (**Figure 2.11**). As the degree of supersaturation is modulated through 2-methylpentane addition, nanostructure growth is enhanced and significantly longer assemblies are formed, exactly resembling the system C vs. D scenario (**Figure 2.8).** Above 15 % non-solvent, the solution experiences an increased degree of supersaturation which exceeds that desired for the meta-stable state, and nucleation dominates growth (**Figure 2.7-c**). As a result, large quantities of shorter P3HT nanorods are formed (**Figure 2.6**). Ultrasonication of solutions that have been excessively driven into supersaturation leads to even more extensive nucleation. For instance, note that P3HT solutions with 30 and 40 vol. % 2-methylpentane produce thin-films with nanorods having average length of 310 nm and 240 nm, respectively, which are far shorter than those of 15 vol. % 2-methylpentane sample consisting 760 nm length nanorods (**Figure 2.6**); ultrasonication of solutions in unstable state for 2 min results in films composed of even shorter P3HT assemblies (**Figure 2.2)**.

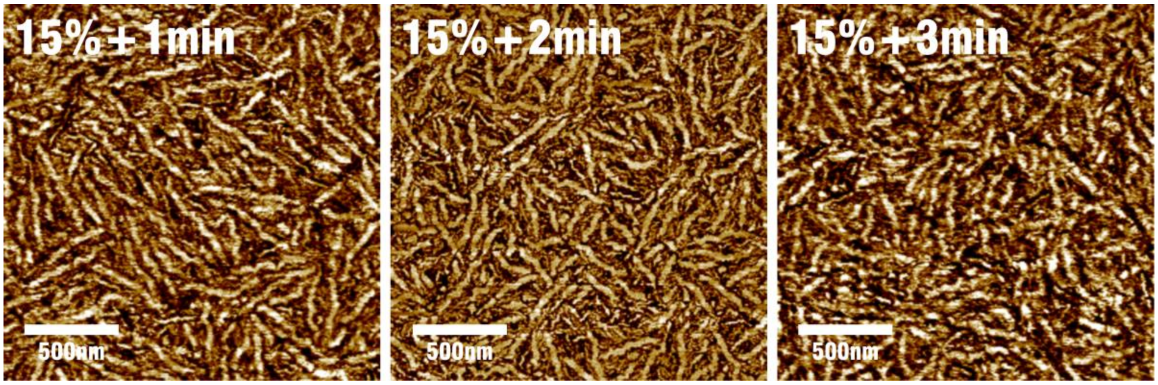

Figure 2.12 AFM phase images of P3HT thin-films prepared via spin coating from $CHCl_3$/2-methylpentane (85/15 v/v) solution with the defined ultrasonication time

An experimental protocol was designed to confirm the validity of the 2-step crystallization model for P3HT self-assembly. Specifically, the volume fraction of 2-methylpentane was maintained at 15%, while ultrasonication time was varied from 1 to 3 min. This approach controlled the degree of supersaturation, and thus the 2-step crystallization model predicts the formation of shorter nanorods when ultrasound is applied for longer times, simply because ultrasonication stimulates nucleation site formation. The experimental results exactly followed these expectations. **Figure 2.12** depicts AFM images of P3HT thin-films prepared from the solvent blend as a function of sonication time. With increased sonication time, length of assembled polymer nanorods decreased from 420 nm to 210 nm. As shown in **Figure 2.11**, the number of nucleation sites gradually increases with increased ultrasonication time. Thus, with a fixed proportion of 2-methylpentane, the length of the nanorod assemblies should shorten as the amount of excess P3HT available for growth from each nucleation site decreases.

Through systematic study and analysis of the AFM morphological images, verification that the assembly process of P3HT into nanorod structures follows a 2-step crystallization model was obtained. Moreover, the individual contributions of ultrasonication and non-solvent addition, specifically 2-methylpentane, on P3HT nanorod formation were elucidated.

2.3 Conclusion

Synergistic use of solubility modulation and ultrasonication, facilitates the controlled assembly of highly-ordered P3HT nano-structures, where the length of rod-like assemblies could be systematically modulated. P3HT thin-films comprised of nano-rod structures assembled in solution through the synergistic approach exhibited hole mobilities reaching an average of 0.103 cm^2/V-s vs. only 0.025 cm^2/V-s for the untreated counterparts. Analysis of the results suggests a new processing methodology for enhanced electronic performance, and importantly allows mechanistic interpretation of P3HT self-assembly. The simple yet powerful 2-step crystallization model consisting of nucleation and growth steps was applied, for the first time, to describe P3HT self-assembly. Arrays of experimental results confirmed the validity of the 2-step crystallization approach to understanding self-assembly processes of the conjugated polymer into mesoscale entities. Length and density of self-assembled rod-like P3HT nanostructures created in solution through non-solvent addition, ultrasonication, and sequential combination of both treatments exactly followed model predictions. Modulation of solution solubility informs optimal/favorable solution conditions for nanostructure growth, while ultrasonication plays a significant role in creating nucleation sites. Moreover, experimental protocols fixing solution solubility but varying ultrasonication time were designed to validate the proposed mechanistic model.

The experimental results were in agreement with the predictions, further supporting the model as a straight forward, yet powerful platform to provide new insights into conjugated polymer self-assembly into meso-scale structures. Systematic analysis of AFM images, GIXRD, UV-Vis, and mobility data highlights the existence and significance of interplay between long range ordering and molecular level interactions for efficient charge carrier transport. Long range order, as discerned from conjugated polymer nanorod length, is a necessary but insufficient requirement. The importance of molecular level interactions for effective macroscopic charge carrier transport was also elucidated. However, in the absence of adequate structures of a critical length, the degree of long range order becomes dominant. The insights provided here will substantially impact the design and development of solution based conjugated polymer processes for flexible electronic and photonic applications.

2.4 Experimental Section

Materials: P3HT was purchased from Reike Metals Inc. and used without further purification. The P3HT used in this study had a M_w of 90 kDa, polydispersity of 2.3, and 96% regioregularity. Chloroform (Anhydrous) and 2-methylpentane (Anhydrous) were purchased from Sigma Aldrich.

Controlled assembly of P3HT nanorods in solution: A combination of 2-methylpentane addition and ultrasonication was used to fabricate P3HT nanorods in solution. First, a chloroform-P3HT solution was prepared: 10 mg of P3HT was introduced into 2 ml of chloroform in a 20 ml borosilicate glass vial. The vial was capped and placed on top of a hot plate at ~55 °C for 30 min to ensure complete dissolution of P3HT. After the complete dissolution of P3HT, the solution was allowed to cool to room temperature. Then, the designated amount of 2-methylpentane was slowly added to the chloroform-P3HT solution. The as-prepared solution was then ultrasonicated for the specified time using a tabletop bath-type ultrasonicator (Bransonic 2510, 40 kHz, 130 W) filled with tap water (23 °C). Ultrasound is acoustic soundwave. So, focused spot should be located for maximized effect. To achieve maximum ultrasound power near the water surface, water level should be carefully adjusted. Simultaneously, it is recommended to use as large amount of water as possible to maintain water temperature during ultrasound application (As mentioned in main text, temperature is one of very important parameters judging degree of saturation). Approximately 1.5 L of water was enough for specific ultrasound bath used in this study. In this study, during ultrasonication, vial was tilted ~ 45 ° in a way that bottom edge of vial locates on top of the spot where ultrasound is generated. Then, distance from ultrasound generating spot was adjusted to find sweet spot. The dissolution and ultrasonication processes were performed in air.

Estimation of average P3HT nanorod length: Image analysis program (ImageJ 1.60) was used to obtain spatial data from AFM images. First, scale has been set by converting pixel into nanometer. 2 um by 2 um AFM image has 2160 pixel by 2160 pixel and pixel can be easily converted into actual length. Then, threshold of images were adjusted to vary the masking of crystalline area and built-in particle analysis function of program was used to mask the crystalline area for data acquisition.

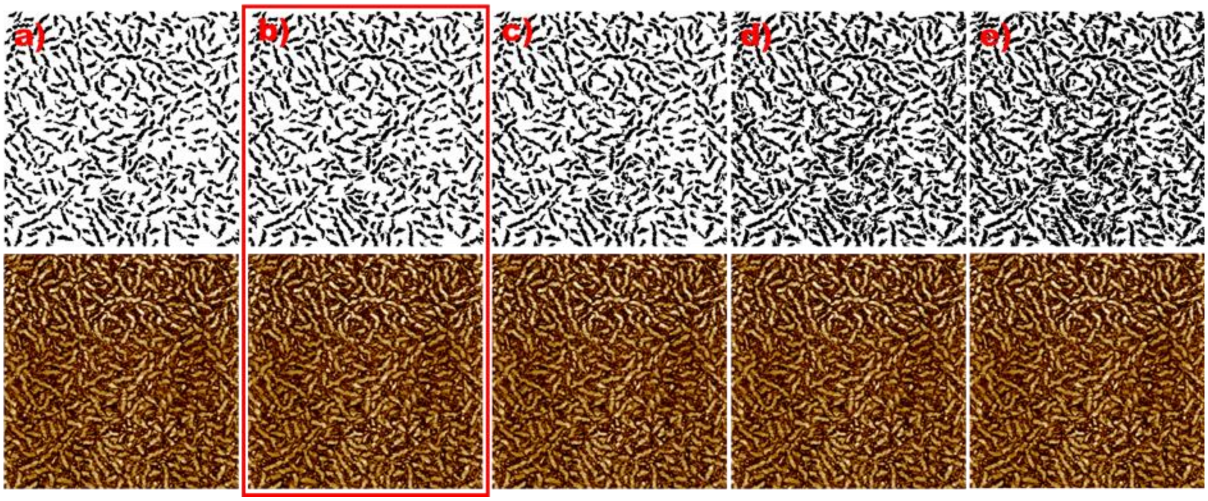

Figure 2.12 Top line: Processed image using image analysis software. Different threshold values are applied for a)~e). Bottom line: Original AFM image of sample made from 5 vol. % 2-methylpentane added solution with 2 min ultrasonication

Among various masked images with differentiated threshold values, the one that resembles the original image the most was selected. **Figure 2.12** shows the selection procedure. Minimum size and circularity filters were used to minimize background disturbance. Even though masking of crystalline areas could be successfully completed, the built-in particle analysis function couldn’t effectively distinguish closely neighboring moieties and gave inaccurate count data. So, we utilized total area data occupied by the masked portion obtained through particle analysis function which should be accurate when proper masking of entities have been done. Among arrays of masked images, the most resembling image was selected for total occupied area data acquisition. Finally, average nanorod length was calculated from dividing the occupied area by the number of nanorods and by the width of the nanorods. Nanorod width was assumed to be same within each AFM image and average width of 5 nanorods was used as the representative width for each image. The number of nanorods was manually counted in most cases;

while the software count function could be used for some images including very short rods such as some samples only treated with ultrasonication and 40 vol. % 2-methylpentane with 2 min ultrasonication sample.

Organic Field-Effect Transistor (OFET) Fabrication and Characterization: The OFET devices with bottom-gate, bottom-contact structure were fabricated to perform electrical characterization of P3HT films fabricated from solutions prepared as above. Highly n-doped silicon wafers with a thermally grown 300 nm thick SiO_2 dielectric surface were used as the substrate. The highly doped silicon substrate served as the gate electrode with the thermally grown SiO_2 as the dielectric layer. Au/Cr was used for the source and drain contacts. The source and drain contacts were fabricated using a standard photolithography based lift-off process inside a cleanroom, followed by E-beam evaporation (Denton Explorer) of 50 nm Au contacts with 3 nm of Cr as the adhesion layer. Before spin-coating P3HT solutions, all devices were cleaned for 30 min in a UV-ozone cleaner (Novascan PSD-UV) to completely remove any residual photoresist and other organic contaminants. OFET devices were prepared by spin-coating (WS-650MZ-23NPP, Laurell) the solutions onto pre-cleaned devices at a spin speed of 1500 rpm for 60 s in air, and tested in nitrogen ambient using an Agilent 4155C semiconductor parameter analyzer. The devices were stored in a vacuum oven (1 Torr) overnight at 50 ° C to remove residual solvent. The field-effect hole mobility was calculated in the saturation regime of transistor operation ($V_D = -3$ V) by plotting the drain current (I_D) versus gate voltage (V_G) and fitting the data to the following equation:

$$I_D = \mu C_{OX} \frac{W}{L} (V_G - V_T) V_D$$

where W (2000 μm) and L (50 μm) are the transistor channel width and length, respectively, V_T is the threshold voltage, and C_{OX} is the capacitance per unit area of the silicon dioxide gate dielectric (1.15×10^{-8} F/cm^2). For each condition, five OFET devices were fabricated and tested for calculation of average mobility.

UV–Vis Spectra of P3HT: The solid state UV–Vis spectra were obtained using an Agilent 8510 Spectrophotometer. Corresponding P3HT films were spin coated onto pre-cleaned glass slides.

Grazing Incidence X-Ray Diffraction (GIXRD): Out-of-plane grazing incidence X-ray diffraction data were obtained using a Panalytical X'Pert Pro system equipped with a Cu X-ray source operating at 45 kV and 40 mA. Grazing incidence angle was fixed at 0.2 ° and the detector was scanned from 3 ° to 30 °. Samples for GIXRD measurements were prepared by spin coating corresponding P3HT solutions on sliced n-doped silicon wafer with 300nm thermally grown SiO_2, identical to that used for fabricating OFET substrates. Substrates were cleaned using the same procedure used for OFET devices.

Atomic Force Microscopy (AFM): The AFM measurements were performed on the area between the source and drain channels of OFET devices after finishing electrical performance measurements of the corresponding devices. An ICON dimension scanning probe microscope (Bruker) operated in tapping mode with a silicon tip (NCS-14, Mikromasch) was used for all AFM measurement.

CHAPTER 3

HANSEN SOLUBILITY PARAMETERS AS A CRITERION FOR OPTIMIZING ULTRASOUND MEDIATED P3HT PROCESSING

3.1 Introduction

Inferior intrinsic electrical properties of organic semiconducting materials has been a major obstacle in the field of organic electronics.[3,4,6,7,19] As a result, significant research efforts have been focused on overcoming such issues and a range of approaches including solution processing techniques[57,64,69,73,86] and novel deposition techniques[15,87,88] have been reported as very effective methods to enhance organic semiconducting materials performance attributes. The one common route has been to induce ordering of the organic semiconducting molecules. However, these techniques are not universal methods suitable in all the conditions. Depending on the components and composition of the target system such as solvent, solute, and concentration, a processing technique that works successfully in certain conditions might not be effective in other conditions.[64,69,89]

In this study, we introduce ‘solubility’ as a determining factor to optimize impact of ultrasound irradiation, one very effective solution processing technique, on poly(3-hexylthiophene) (P3HT) molecular assembly in different conditions. Hansen Solubility Parameters (HSPs) were adopted to quantify solubility for effective optimization, and meaningful results could be obtained. First, the feasibility of the ultrasound irradiation process on P3HT solution systems were tested with several ‘good’ solvents. It was found that only the P3HT solution system based on $CHCl_3$ as main solvent was responsive to ultrasound irradiation. Through HSPs analysis, solubility of solutions used for the test could be quantified and interestingly, the solubility of P3HT in $CHCl_3$ was the poorest among tested solvents. The result indicates a determinant influence of solubility on efficacious molecular ordering through ultrasound treatment. One step forward, through systematic solubility modulation based on HSPs analysis, we could successfully demonstrate assembly of mesoscale P3HT structures from P3HT solution systems which were initially irresponsive to ultrasound treatment. This impressive result confirms the importance of solubility as a processing parameter and it also demonstrates the useful application of HSPs as a simple but useful processing optimization platform.

3.2 Results and Discussion

3.2.1 Impact of Solubility on Molecular Ordering of P3HT

Several organic solvents known to provide good solubility towards P3HT were tested to investigate their feasibility as approaches for P3HT assembly into supramolecular structures via ultrasonication. Examples include carbon disulfide (CS_2), chloroform ($CHCl_3$), trichloroethylene (TCE), and chlorobenzene (CB). P3HT solutions having a concentration of 5 mg/ml were prepared by dissolving 10 mg of P3HT into 2 ml of solvent. Each solution was ultrasonicated for 5 min in an ultrasonic bath. Interestingly, the P3HT/$CHCl_3$ system was the only system showing a response to ultrasound irradiation. Among 4 different P3HT solutions, only the P3HT/$CHCl_3$ solution exhibited a color change from orange to purple upon ultrasound irradiation. Color change (chromism) is a simple but powerful indication of mesoscale assembly of conjugated molecules.[30,71,90,91] In the case of P3HT, color of the initial solution before any treatment is orange. If molecules are assembled into larger structures within the solution during/after processing, ultrasonication in this case, solution color should be red-shifted. The color shift of the solution originates from a narrowed HOMO-LUMO energy gap for P3HT after processing. Ordered conjugated polymer chains consisting of mesoscale assemblies enjoy less interrupted conjugation compared to free polymer chains floating inside solution, thus the HOMO-LUMO energy gap is narrowed. As HOMO-LUMO energy gap becomes narrower, lower energy (longer wavelength, more reddish) region of light will be absorbed, thus the color of solution blue-shifts. Moreover, the P3HT/$CHCl_3$ solution was the only system showing a change in transparency. Before ultrasonication, all 4 P3HT solutions were transparent, orange in color. After ultrasound treatment, the P3HT/$CHCl_3$ solution not only experienced a color change to purple but it also became cloudy. This phenomenon is another useful indicator to check formation of mesoscale assemblies in solution. Assembled mesoscale P3HT moieties are large enough to scatter light. As a consequence, the solution becomes opaque.

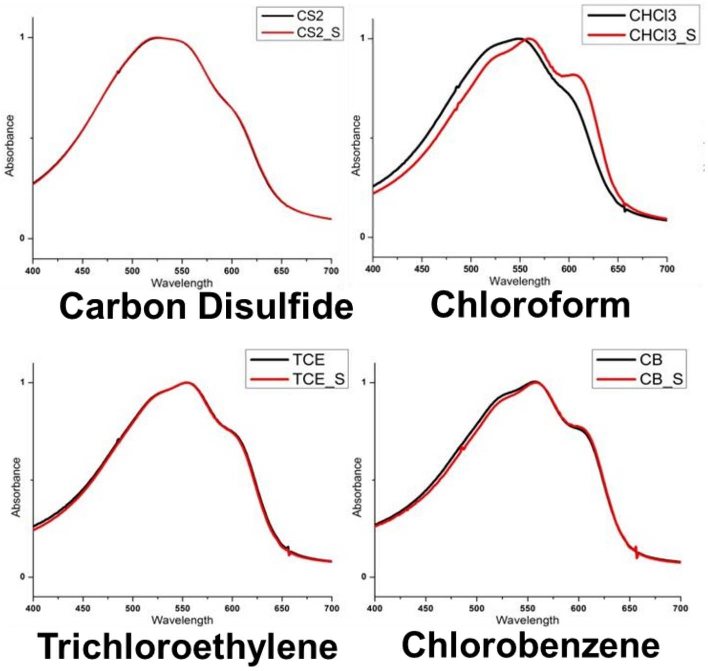

Figure 3.1 UV-Vis spectra of P3HT films made from four different kinds of solvents. *Black line*, films made from solution without ultrasonication. *Red line*, films made from solution after ultrasonication

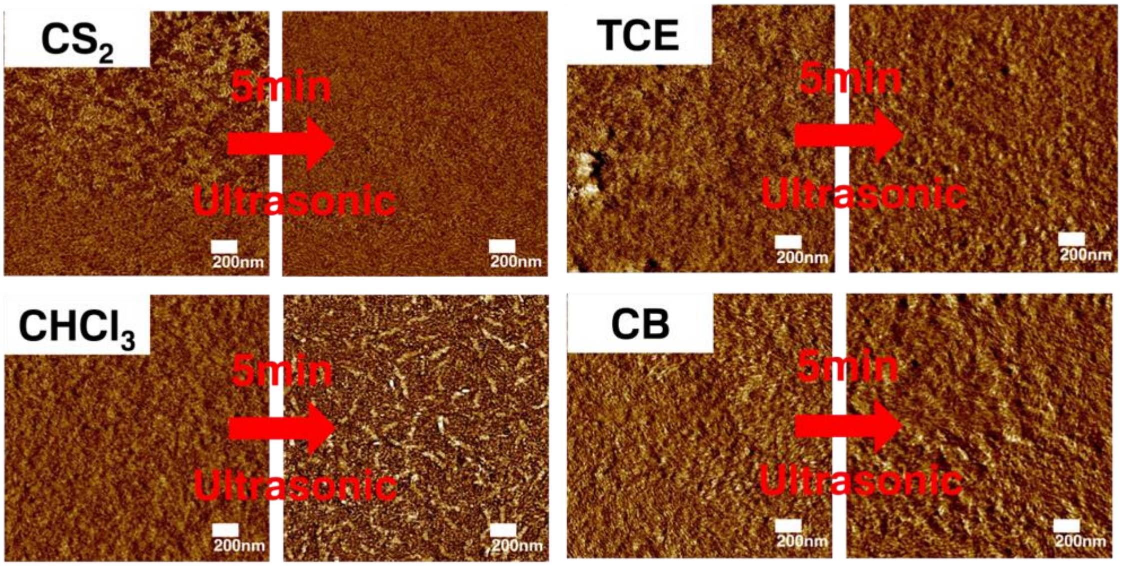

Figure 3.2 AFM images of P3HT films made from four different kinds of solvents. Before and after ultrasound treatments were compared.

Analysis of P3HT films fabricated out of corresponding P3HT solutions exhibits corresponding results **(Figure 3.1)**. The $CHCl_3$ system only showed a red shift of the π-π^* band around 500~550 nm in UV-Vis absorption spectra which clearly agrees with results from the observation of solution color change. Moreover, atomic force microscopy (AFM) also confirmed these results **(Figure 3.2)**. Among thin films fabricated from ultrasonicated P3HT solution, only the ultrasonicated $CHCl_3$/P3HT film included noticeable assemblies of P3HT molecules. So, what would be the determining factor that makes $CHCl_3$/P3HT as the only solution system accompanying molecular assembly through ultrasonication?

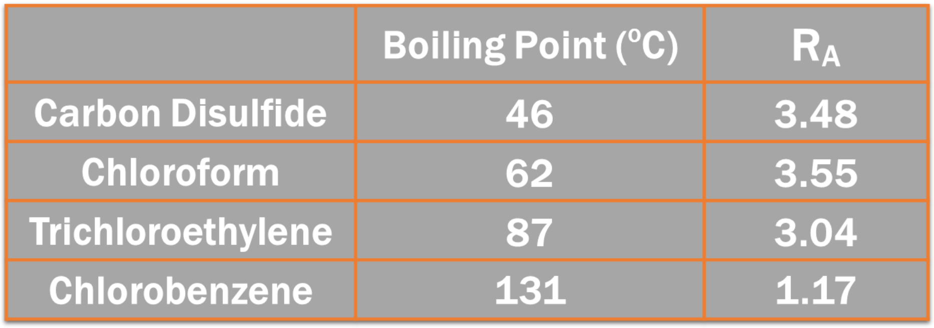

	Boiling Point (°C)	R_A
Carbon Disulfide	46	3.48
Chloroform	62	3.55
Trichloroethylene	87	3.04
Chlorobenzene	131	1.17

Figure 3.3 Boiling point and radius of interaction (R_A) of solvents used

As a first thought, solvent boiling point (BP) was considered as the origin of this phenomenon. BP is related to the intermolecular forces within a solvent medium. If the BP of one solvent is high, it can be said that interactions between the solvent molecules are strong so that more external energy is required for dissociation of molecules. Thus, it was postulated that high BP solvents with stronger intermolecular interactions will show weaker molecular vibration/movement during ultrasonic irradiation, impeding efficient formation of cavitation which induces ordering of the semiconducting polymer. However, this analogy does not hold true for CS_2, a good solvent with the lowest BP among the solvents investigated here. CS_2/P3HT solutions do not exhibit any change upon ultrasonication. While the molecular interaction analogy cannot be totally ignored, it can be concluded that BP is not the determining factor in whether a certain solvent will respond to ultrasonication or not. The effect of solubility was investigated next.

The solubility of each solvent was quantified through HSP analysis. As a first step, HSP of P3HT was determined based on solubility tests including 20 different solvents. Then, the radius of interaction (R_A) between each of the solvents and P3HT was calculated. P3HT/$CHCl_3$ had the largest R_A value suggesting the poorest solubility.

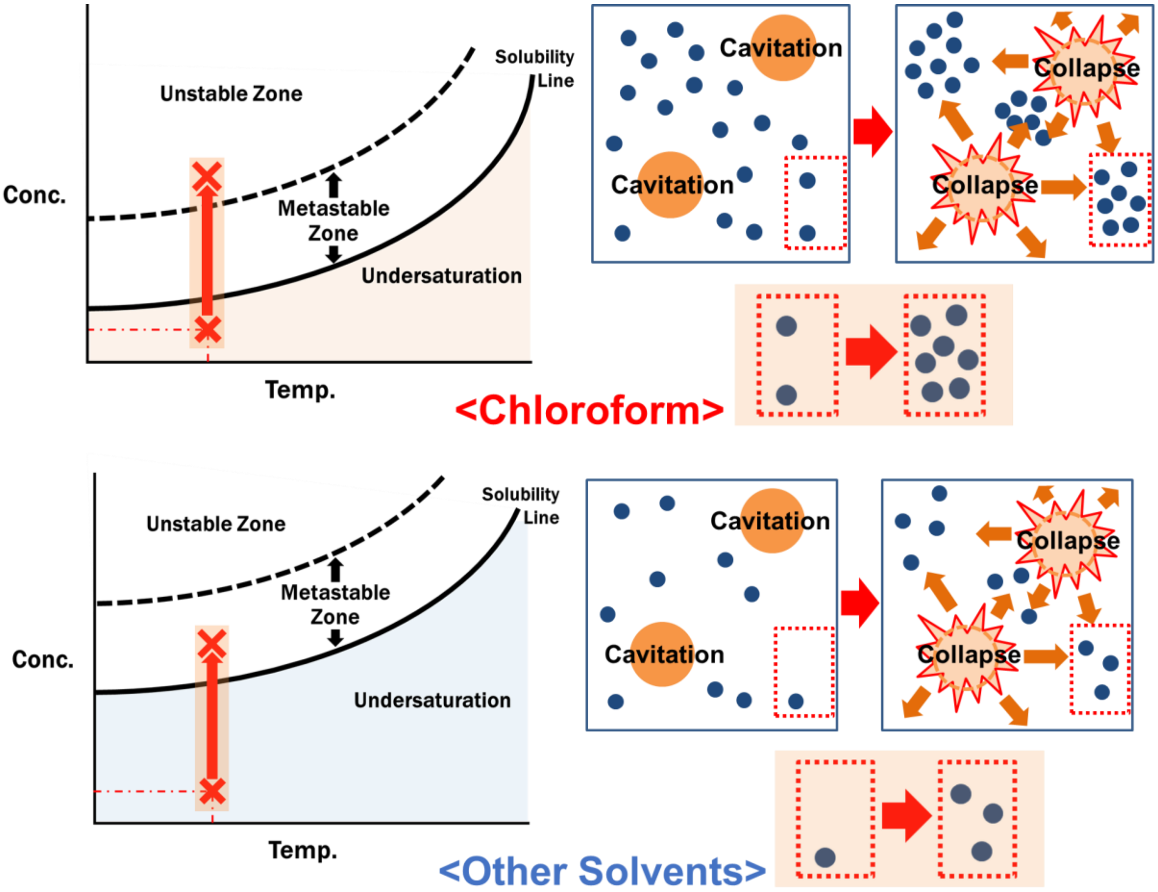

Figure 3.4 Schematic description about effect of ultrasound induced cavitation on local supersaturation in P3HT solution system

In the previous chapter, the degree of supersaturation was presented as the main driving force guiding molecular assembly of organic semiconducting materials in solution. Exactly the same principle applies in this case. Ultrasound irradiation promotes cavitation within the solution.[83,92–94] Cavitation collapses at a certain point and tremendous pressure is applied to a local area surrounding cavitation **(Figure 3.4)**. As a result, the local area experiences an abrupt increase in concentration and suddenly falls into the supersaturated region, thus leading to the creation of nucleation sites. In solution systems where the solubility is too ‘good’, there is a good possibility that the solution system is not saturated (undersaturated) **(Figure 3.4)**. Ultrasound irradiation guides molecular assembly by provoking local supersaturation via cavitation effects. So, if the solution is too undersaturated, the local concentration change caused by ultrasound is not sufficient to reach the supersaturated state. As a result, no molecular assembly takes place. In other words, degree of ‘good’ is crucial and it can be quantified through HSPs analysis. Based on experimental results and HSPs calculation, it can be concluded that only P3HT/$CHCl_3$ solution system resides within an effective degree of solubility where ultrasonication can induce local supersaturation.

	R_A
2-MP	9.79
CB	1.17
CB + 20% 2MP	2.20
CB + 35% 2MP	3.53
CB + 45% 2MP	4.47

Figure 3.5 Radius of interaction (R_A) of 2MP and CB/2MP mixtures with varied amount of 2MP

3.2.2 Optimization of Ultrasonication Process Using HSPs

Next, through HSP calculations, the solubility of the solution system was modulated in the poorer direction to check whether HSPs can be utilized as an optimization parameter or not. Varied amounts of 2-methypentane (2MP), a poor solvent to P3HT, was added to the chlorobenzene (CB)/P3HT solution system where no change could be found after ultrasound irradiation. Surprisingly, CB/2MP/P3HT solution system started to show a response to ultrasound irradiation when the amount of 2-methylpentane was controlled to reach the R_A value of $CHCl_3$/P3HT.

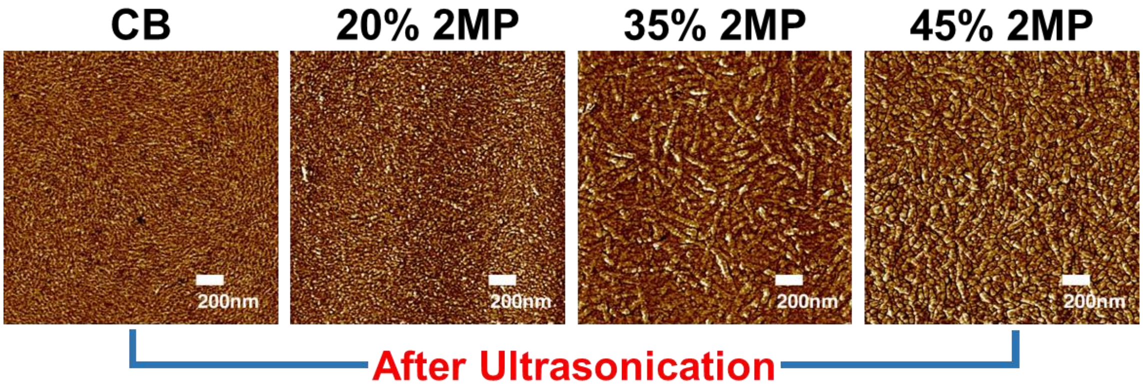

Figure 3.6 AFM images of P3HT films from ultrasonic treated CB/2MP/P3HT solution.

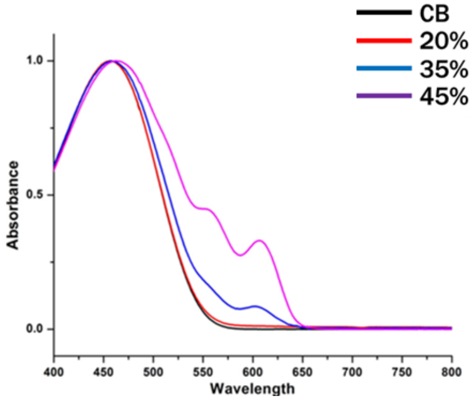

Figure 3.7 UV-Vis spectra of ultrasonicated solutions prepared with varied CB/2MP ratios.

The impact of solubility is clearly observed in both AFM images and UV-Vis absorption spectra of the solutions **(Figure 3.6, 3.7)**. For pure CB (0 % 2MP), no ordered structures were apparent upon ultrasonication. However, upon 35 % addition of 2MP where R_A equals 3.53 (R_A of P3HT = 3.55), the P3HT/CB system began to exhibit a response. Exactly the same trend could be observed in the solution UV-Vis spectra, peak development at ~500 nm indicating molecular ordering could be observed after 35 % addition of 2MP.

3.3 Conclusion

Through tests of 4 different solution systems known as having ‘good’ solubility to P3HT, the impact of solubility on the ultrasound induced molecular ordering process could be studied. Among 4 solution systems, only $CHCl_3$/P3HT system responded to ultrasound irradiation. With simply a conventional definition of ‘good’ and ‘bad’ solvents, the phenomenon couldn’t be explained. However, through adoption of HSP, the degree of solubility could be successfully quantified and the impact of solubility on the ultrasonication process was confirmed. $CHCl_3$ had poorest solubility towards P3HT among 4 different ‘good’ solvent; and relatively poorer solubility was the driving force which made ultrasound irradiation effective. Moreover, HSPs were utilized to optimize the ultrasonication process. By systemically modulating solubility of the chlorobenzene/P3HT solution system based on HSP analysis, the solution system could be modulated to experience molecular assembly through ultrasonication. A controlled amount of 2-Methylpetane, a poor solvent to P3HT, was added to adjust the solubility of the solution system to reach that of $CHCl_3$. With the adjustment, the system responded to ultrasonication. As a result, apparent molecular assembly of P3HT in ultrasonicated CB/2MP/P3HT solution and corresponding film could be confirmed through UV-Vis absorption spectra and AFM.

3.4 Experimental Section

Materials: P3HT and all the solvents used in this study were purchased from Sigma Aldrich and used without further purification. The P3HT used in this study had Mn of 40.3 kDa and Regioregularity of 92 %.

UV–Vis Spectra of P3HT: The solid state UV–Vis spectra were obtained using an Agilent 8510 Spectrophotometer. Corresponding P3HT films were spin coated onto pre-cleaned glass slides.

Atomic Force Microscopy (AFM): The AFM measurements were performed on glass slide coated with corresponding P3HT films. Veeco Digital Instruments Dimension 3100 scanning probe microscope operating in tapping mode with a silicon tip (NSC14, MikroMasch).

CHAPTER 4

ELASTOMER–POLYMER SEMICONDUCTOR BLENDS FOR HIGH PERFORMANCE STRETCHABLE CHARGE TRANSPORT NETWORKS

4.1 Introduction

Organic/polymeric semiconducting materials offer the prospect of increased mechanical ductility as compared to inorganic semiconductors. As a result, stretchable electronics has captured the interest of many researchers exploring avenues to applications such as wearable electronics, biomedical devices, sensors, etc.[95,96] With regard to the active material, efforts have focused primarily on maximizing semiconductor performance through design of new materials[97–102] and applicable processing techniques.[50,51,54–56,73,87,103,104] However, only few investigations have given attention to consequences of improved semiconductor performance on intrinsic mechanical stretchability of polymer semiconducting materials. Since 2010,[105] studies have begun to appear that suggest a negative relationship between semiconductor crystallinity, molecular ordering and charge carrier mobility with ductility.[105–109] However, these investigations all relied upon direct comparisons between materials that were *not identical*. Thus, the impact of molecular ordering on the mechanical properties of organic/polymeric semiconducting materials remains an open question.

Here, we systemically interrogated the mechanical resiliency of poly(3-hexylthiophene) (P3HT) films under mechanical strain, whereby the identical batch of polymer was processed using methods known to create thin-films with different degrees of molecular ordering.[57,86] The results revealed significant deterioration in materials ductility as a direct function of enhanced ordering. Further, the efficacy of the recently reported use of an elastomer/P3HT blend to fabricate stretchable semiconducting films was also examined. Shin, *et al.*[110] reported that a blend of P3HT and polystyrene-block-poly(ethylene-co-butylene)-block-polystyrene (SEBS) enabled films with no apparent degradation in active material charge transport performance upon stretching. The P3HT/SEBS film exhibited a mobility of ~0.007 $cm^2V^{-1}s^{-1}$, before and during stretching up to 100% of its original length. Unfortunately, data for a P3HT control was not presented; however, the blend film mobility is comparable to that found here for pristine P3HT (*vide infra*).

Ready access to process methodologies that effect different levels of molecular ordering[57,86] allowed investigation into the impact of a simple mixing approach to facilitate enhanced ductility without loss of electrical performance. Using pre-processed P3HT solutions, to which were added polydimethylsiloxane (PDMS) elastomer solutions, P3HT/PDMS semiconducting composite films boasting significantly improved resistance to external strain were fabricated. The stretchable composite films prepared with pre-processed semiconductor exhibited improved electrical performance (0.18 ± 0.03 $cm^2V^{-1}s^{-1}$) compared to control, non-PDMS containing samples (0.088 ± 0.014 $cm^2V^{-1}s^{-1}$). For comparison, a PDMS blend of pristine, untreated P3HT was electrically inactive (pristine

P3HT mobility was 0.004±0.0005 $cm^2V^{-1}s^{-1}$). Characterization of the solutions and solidified films using UV-Vis spectroscopy confirmed improved semiconductor molecular ordering upon elastomer blending which explains enhanced semiconducting performance of the composite. Hansen solubility parameter (HSP) analysis and solution evaporation experiments further substantiated the results. The results presented here suggest a cost effective, viable approach to achieve flexible, bendable and stretchable, semiconducting materials and devices. They provide a viable platform towards integrated, 4D electronic and photonic circuits.

4.2 Result and Discussion

4.2.1 Relationship between polymer semiconductor molecular ordering and mechanical ductility

The relationship between semiconducting polymer crystallinity, mobility and mechanical behavior was probed directly by using P3HT solutions that had undergone pre-deposition processing.[57,86] The selected approaches provided means to modulate conjugated polymer molecular ordering, thin-film crystallinity and resultant macroscale mobility by over one order of magnitude.[57,86] Three distinct process protocols for regioregular (RR) P3HT (96 % RR, MW 69 K, PDI 2.3) were used; namely, pristine P3HT in chloroform ($CHCl_3$), ultrasonicated (2 min) P3HT in $CHCl_3$ solution, and P3HT-

$CHCl_3$ solution treated sequentially with poor solvent addition (15 vol.% 2-methylpentane) and ultrasonication (2 min) (**Figure 4.1-a~c**).

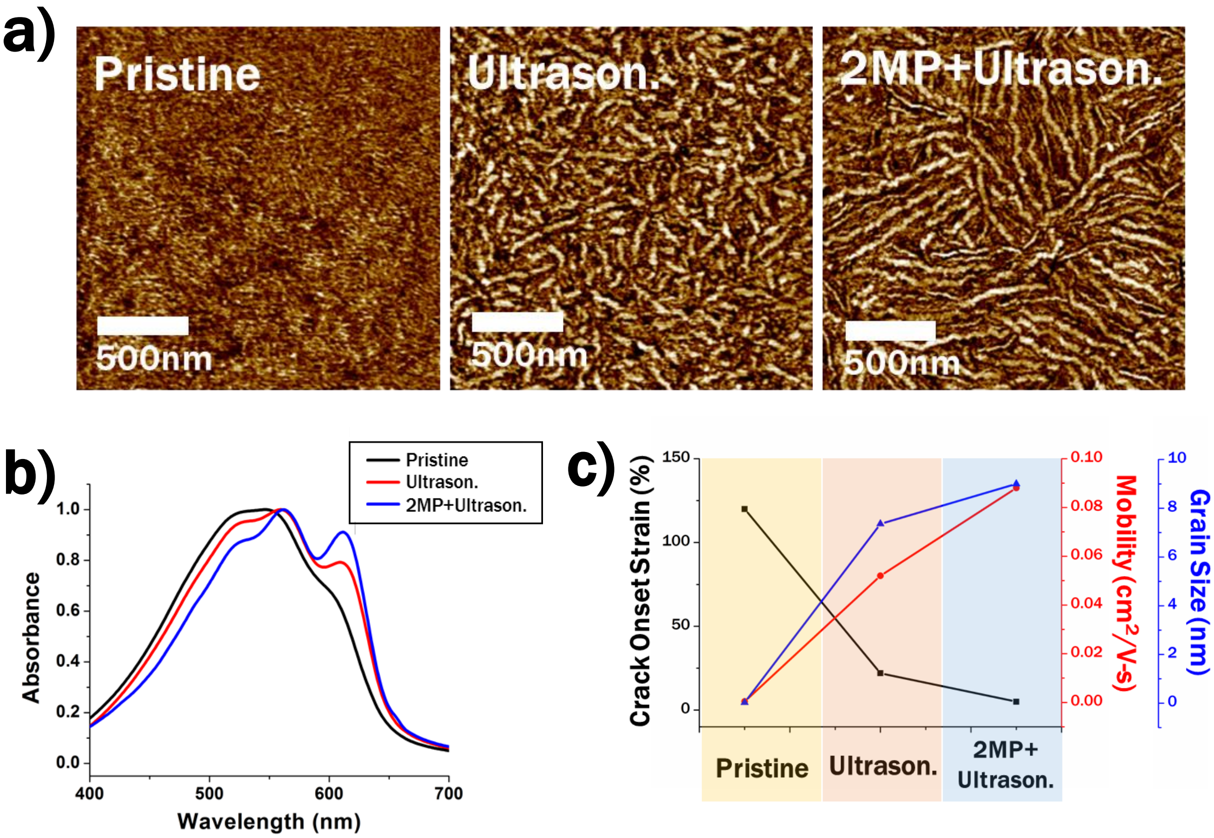

Figure 4.1-a~c a) AFM phase images, b) Film UV-Vis absorption spectra, and c) Crack onset strain, Crystallite grain size, and hole mobility of P3HT films fabricated from pristine, 2 min ultrasonicated, and 15 vol. % 2-methylpentane added then 2 min ultrasonicated P3HT solutions.

P3HT thin-films derived from both ultrasonicated solutions appeared distinctly more ordered/crystalline than films obtained from untreated polymer solution. Atomic force microscopy (AFM) images of the corresponding films are presented in **Figure 4.1-a**, where the self-assembled P3HT mesoscale features are visibly larger in films prepared from solutions treated with both poor solvent and ultrasonication. **Figure 4.1-b** depicts thin-film UV-vis absorption spectra, in sequential manner from untreated, ultrasonicated, to poor solvent/ultrasonicated samples. The observed red-shift and development of low energy bands support the premise that the degree of polymer chain ordering is enhanced in the sequence shown.[72,76,111,112] Further, crystallite grain size (calculated in the (100) lamellar packing direction from the FWHM of grazing incidence x-ray diffraction patterns) increased for the same sample sequence (**Figure 4.1-c**). Organic field effect transistor (OFET) devices were fabricated from each solution to validate the morphological effects on the charge transport characteristics. A trend, similar to that determined for molecular ordering, was obtained for macroscale hole mobility. Pristine P3HT exhibited a mobility of 0.004 ± 0.00056 $cm^2V^{-1}s^{-1}$, the ultrasonicated sample mobility was 0.052 ± 0.0066, and films derived from the poor solvent/ultrasonicated solutions had mobilities of 0.088 ± 0.014 $cm^2V^{-1}s^{-1}$ (**Figure 4.1-c**).

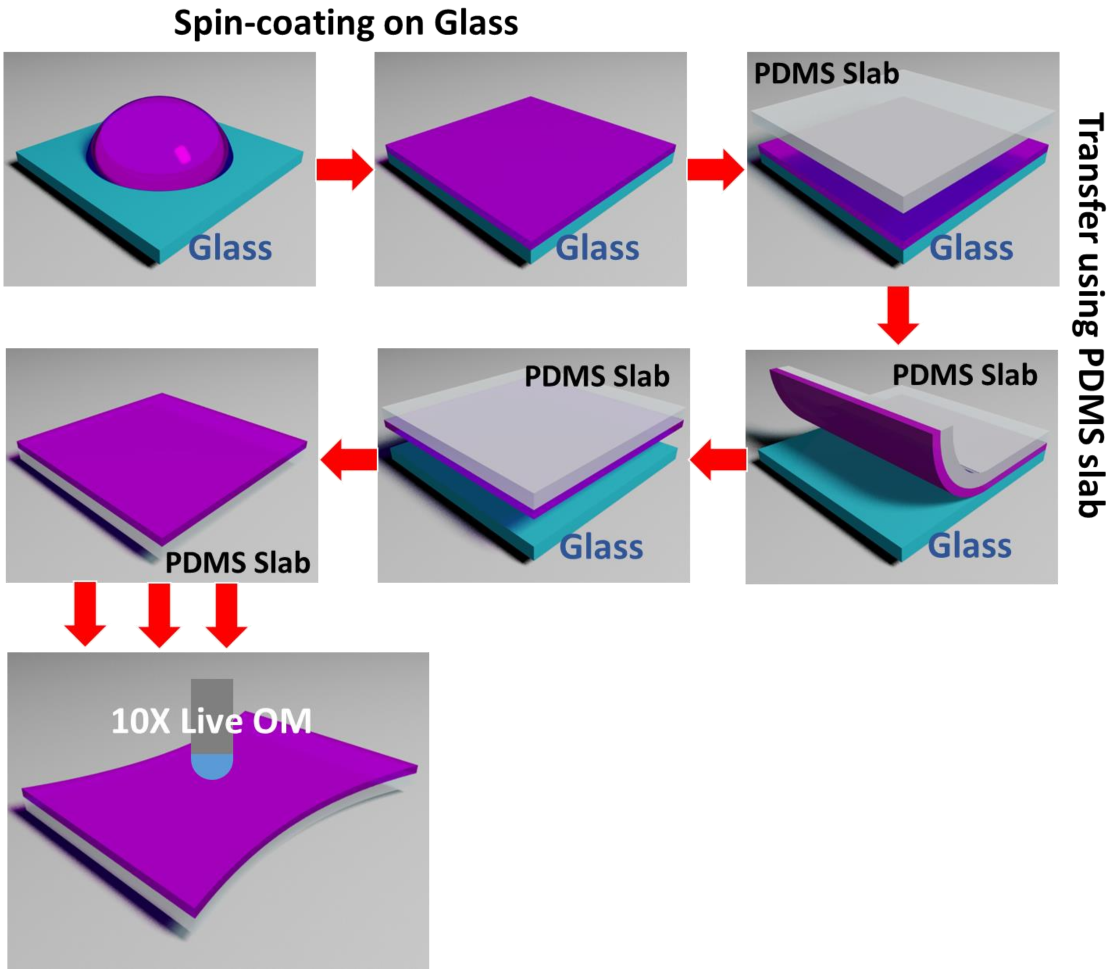

Figure 4.2 Scheme depicting experimental procedures of measuring mechanical ductility of semiconducting films.

Figure 4.2 depicts the experimental details associated with subsequent interrogation of the mechanical integrity of the array of P3HT films prepared as above. Recall that thin-film molecular ordering positively correlates with electrical performance. By using the identical batch of semiconducting polymer, it was possible to probe the relationship between polymer semiconductor molecular ordering and mechanical ductility. Experimentally, the corresponding P3HT solutions were first spin-coated onto pre-cleaned glass substrate, after which, each deposited film was transferred to a PDMS slab. Then, the as transferred P3HT on PDMS samples were stretched using a linear micro-stage, and simultaneously observed under a CCD camera equipped with a 10 X optical zoom lens. This technique allowed observation of the onset of microscopic crack generation, a defect that is expected to have negative consequences on charge transport within flexible/stretchable microelectronic devices.

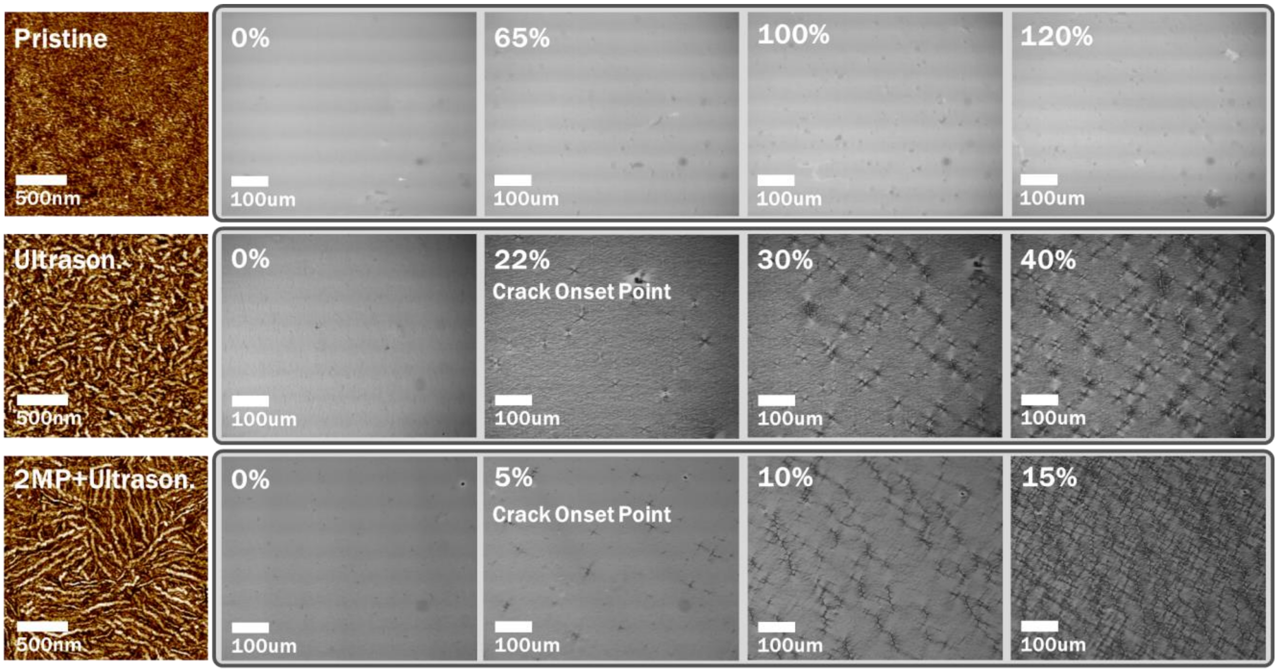

Figure 4.3-a~c Optical microscopy images of P3HT films fabricated from a) pristine, b) 2 min ultrasonicated, c) poor solvent (2-methylpentane) treated and ultrasonicated P3HT solutions under specified amount of strain.

Microscopic fracture upon film elongation was discerned to occur at significantly lower % strain level in more ordered, higher mobility P3HT films. As seen in **Figure 4.3-a**, no fractures were observed for amorphous, pristine polymer films even after being pulled to 120 % strain. Cracks with size on the order of 10 µm were apparent for films obtained from ultrasonicated solutions after only 22 % strain. Distinct cracks occurred after only 5 % strain for the P3HT films processed to exhibit the highest mobility and crystallinity (**Figure 4.3-c**). The results from these studies, for the first time, confirm that improvement in the charge transport characteristics of organic semiconducting materials through enhanced molecular ordering/thin-film crystallinity has direct, negative consequences on ductility (**Figure 4.3-a~c**, **Figure 4.1-c**).

4.2.2 Mechanical and Electrical Property Enhancement in Elastomer-Processed P3HT Composite

The results presented above underscore the need to identify a viable approach to access ordered, crystalline high mobility organic/polymer semiconducting systems that additionally are ductile and stretchable. Studies have shown that P3HT can be blended successfully with insulating polymers such as polystyrene (PS),[113,114] poly(methyl methacrylate) (PMMA)[115,116], and even SEBS block copolymer[110]. In each case, semiconducting performance was retained, and in the cases of PS and PMMA, ambient device stability improved. These observations suggest the possibility of identifying a host matrix that could first impart stretchable characteristics to a blend. Second, appropriate selection of a host matrix could simultaneously impart the necessary molecular interactions with the semiconducting component to induce conjugated polymer molecular ordering and resultant increased charge carrier mobility so that blend composite enjoying both stretchability and high charge carrier transport . One attractive candidate for such a host is polydimethyl siloxane (PDMS), a readily available, low cost elastomer, which undergoes curing at low temperatures.

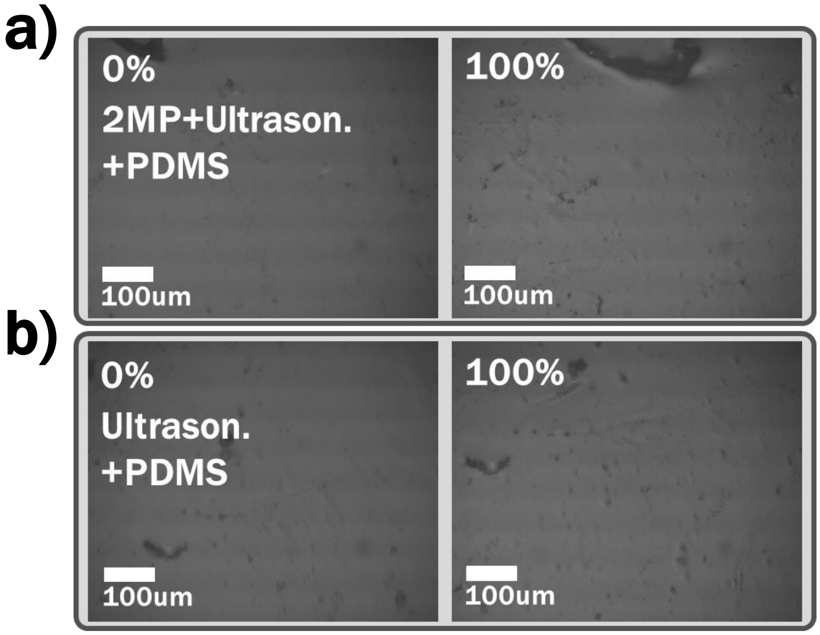

Figure 4.4-a, b Optical microscopy images of P3HT/PDMS composite semiconducting films under strain. Films were fabricated from a) poor solvent treated then ultrasonicated P3HT solution mixed with PDMS, b) ultrasonicated P3HT solution mixed with PDMS.

P3HT/PDMS composite films were fabricated as follows. First, P3HT/$CHCl_3$ solutions were prepared, followed by poor solvent (2-methylpentane) addition and ultrasonication, as described above. Concurrently, PDMS elastomer resin and cross-linker were mixed in a 10:1 weight ratio and diluted with chloroform. Subsequently, the two solutions were mixed, and films were fabricated by spin-coating onto device substrates for electrical characterization and glass substrates for mechanical property determination. The P3HT to PDMS weight ratio in the final mixed solution was 0.75:100. While films prepared from P3HT solutions treated with addition of poor solvent and ultrasonication exhibited poor mechanical integrity upon subjection to external strain (crack onset point at 5 % strain), mixing identically treated P3HT solutions with PDMS in $CHCl_3$, created films with radically different mechanical behavior. No microscopic fractures were observed even after stretching to 100 % strain (**Figure 4.4-a**). The same trend was observed for ultrasonicated semiconductor/PDMS blends (**Figure 4.4-b**).

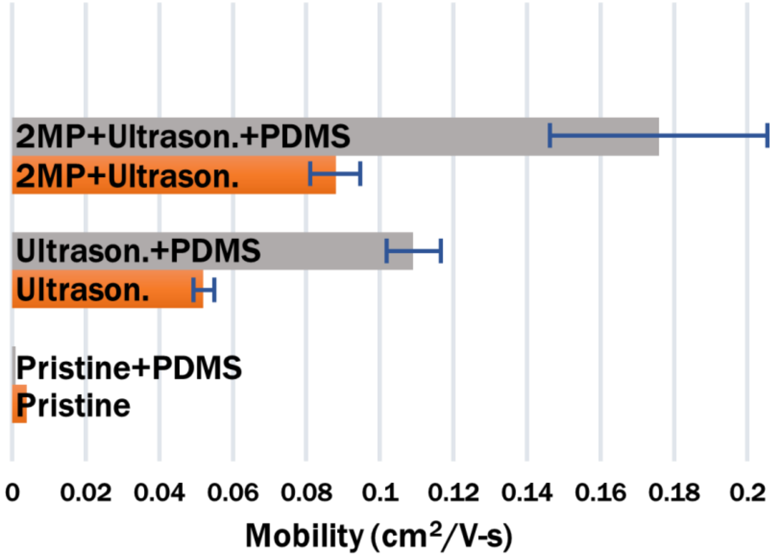

Figure 4.5-a Chart comparing hole mobility of processed P3HT/PDMS composite film and single component P3HT films with same processing condition.

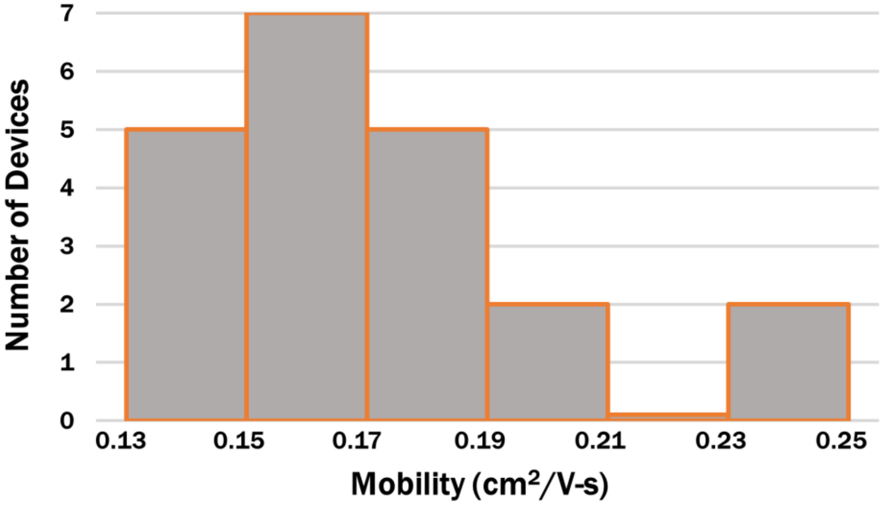

Figure 4.5-b Histogram representing distribution of hole mobility value of 21 devices fabricated with poor solvent treated, ultrasonicated P3HT solution mixed with PDMS solution in chloroform.

In terms of charge transport performance, surprisingly, the ductile P3HT/PDMS blend films prepared from processed P3HT solutions exhibited significantly enhanced charge transport performance compared to the fragile respective controls (**Figure 4.5-a**). Hole mobility of semiconducting film was determined using a bottom gate bottom contact OFET configuration. All of measured OFET devices exhibited typical transfer and output curves. Representative curves are presented below (**Figure 4.6-a, b**). Average hole mobility for devices fabricated from blends where P3HT had been treated with poor solvent/ultrasonication was 0.18±0.03 $cm^2V^{-1}s^{-1}$ with a maximum value as high as 0.24 $cm^2V^{-1}s^{-1}$. The average hole mobility was almost 2 times higher than that obtained for control P3HT films prepared from similarly treated solutions (0.088±0.014 $cm^2V^{-1}s^{-1}$). For comparison, untreated, pristine P3HT films exhibited a factor of 44 lower hole mobility (0.004±0.0005 $cm^2V^{-1}s^{-1}$). Improved performance was also observed with the ultrasonicated samples. Average hole mobilities for films of ultrasonicated P3HT and ultrasonicated P3HT/PDMS blends were 0.052±0.007 $cm^2V^{-1}s^{-1}$ and 0.11±0.016 $cm^2V^{-1}s^{-1}$, respectively. Importantly, no charge transport behavior was observed for PDMS blends prepared with a pristine P3HT solutions, parent semiconductor control samples exhibited some mobility (approximately 0.004 $cm^2V^{-1}s^{-1}$).

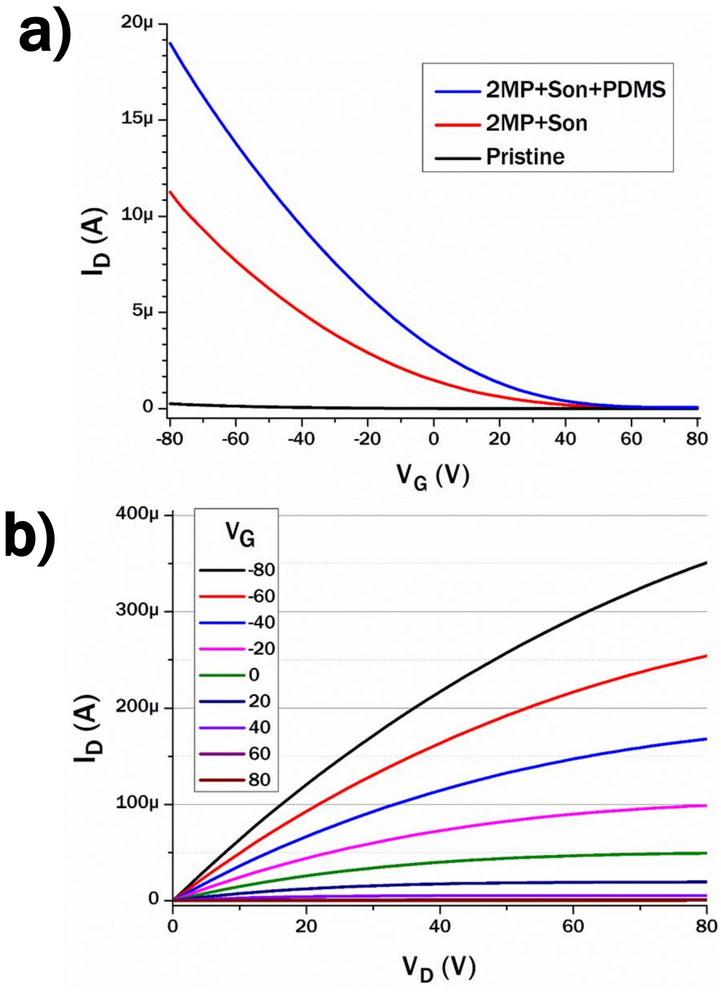

Figure 4.6-a, b a) Representative transfer curves of OFET devices based on corresponding processing condition. b) Representative output curve of processed P3HT/PDMS OFET device.

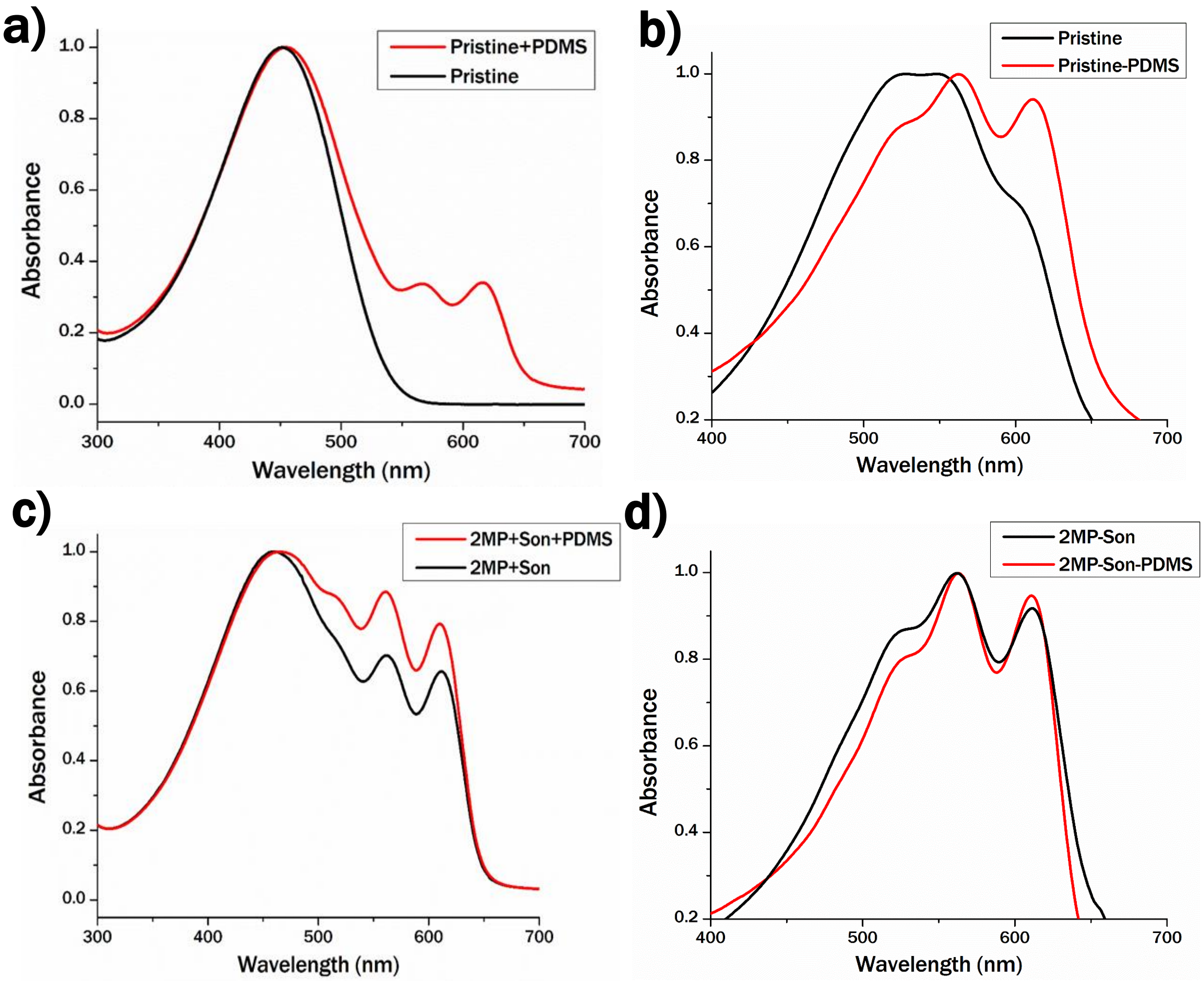

Figure 4.7-a~d UV-Vis absorption spectra comparing before and after mixing PDMS/Chloroform solution with a) pristine and b) poor solvent treated then ultrasonicated P3HT solution. c), d) are film UV-Vis spectra of films fabricated from same conditions as a), b)

To investigate the origins of P3HT/PDMS composite film electrical performance enhancement, UV-Vis spectra of the P3HT/PDMS solutions and resultant films were analyzed to interrogate possible differences in molecular organization, a critical factor determining charge transport efficiency in organic semiconducting films. First, pristine P3HT solutions were compared before and after mixing with PDMS. In the presence of

PDMS, the P3HT absorbance underwent a red-shift coincident with development of low energy bands (**Figure 4.7-a**), suggesting improved conjugated polymer molecular ordering.[72,76,111,112] The same trend was observed upon mixing of pre-processed P3HT solutions with the elastomer (**Figure 4.7-b**).

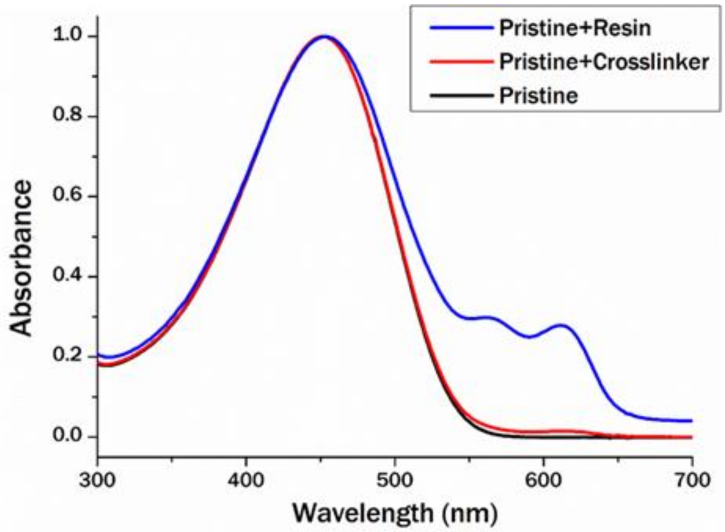

Figure 4.8 UV-Vis absorption spectra of P3HT solutions with PDMS resin and crosslinker separately.

As shown in **Figure 4.8**, the P3HT spectral changes arise strictly from interactions with PDMS, not the crosslinking agent. Solidified thin-films prepared from the blends not only underwent a red-shift of the P3HT π-π* band, but the low energy bands were noticeably more intense than found for the pristine P3HT samples (**Figure 4.7-c, d**). Thus UV-Vis analysis suggests that PDMS plays a critical role in P3HT molecular organization and concomitant impact on blend charge carrier mobility.

The impact of PDMS on semiconductor molecular ordering was rationalized through Hansen solubility parameter (HSP) analysis. HSPs for each polymer were calculated based on the experimental polymer solubilities in an array of solvents with known HSPs (**Figure 4.9** and **Figure 4.10**). The Hansen radius (R_0) for a given material spans a space that includes possible chemically compatible HSP coordinates. When the distance between two materials in Hansen 3D space (R) is within R_o, the materials in question can be assumed to be chemically compatible, i.e., possess favorable interactions.[42] The R value between PDMS and P3HT was estimated as 7.35, while R_0 for PDMS and P3HT was 5.6 and 3.6, respectively. The value of R higher than R_0 of PDMS and P3HT suggests that PDMS is not within compatible range of P3HT, also P3HT is not compatible with PDMS. So, it can be concluded that the interaction between the two blend components acts unfavorable manner, which would be expected to promote ordering of semi-crystalline P3HT molecules.

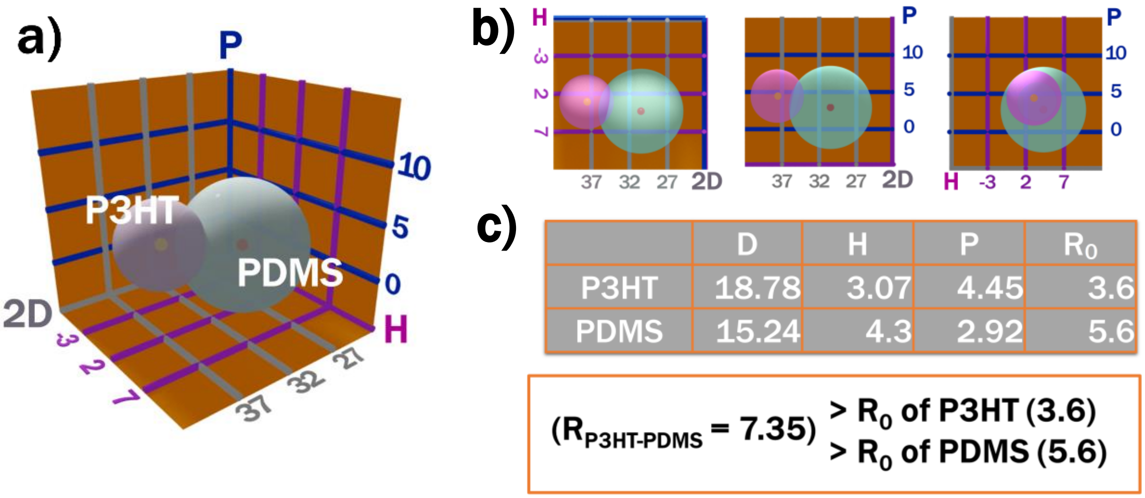

	D	H	P	R_0
P3HT	18.78	3.07	4.45	3.6
PDMS	15.24	4.3	2.92	5.6

($R_{P3HT\text{-}PDMS}$ = 7.35) > R_0 of P3HT (3.6)
> R_0 of PDMS (5.6)

Figure 4.9-a~c a) Hansen spheres of P3HT (Red Sphere) and PDMS (Green Sphere) constructed on Hansen 3D space. Each axis represents 3 different components consisting Hansen solubility parameters (Dispersion, Polar, and Hydrogen-bonding related cohesion energy). b) Hansen spheres observed in different perspectives. c) Hansen solubility parameters of P3HT and PDMS

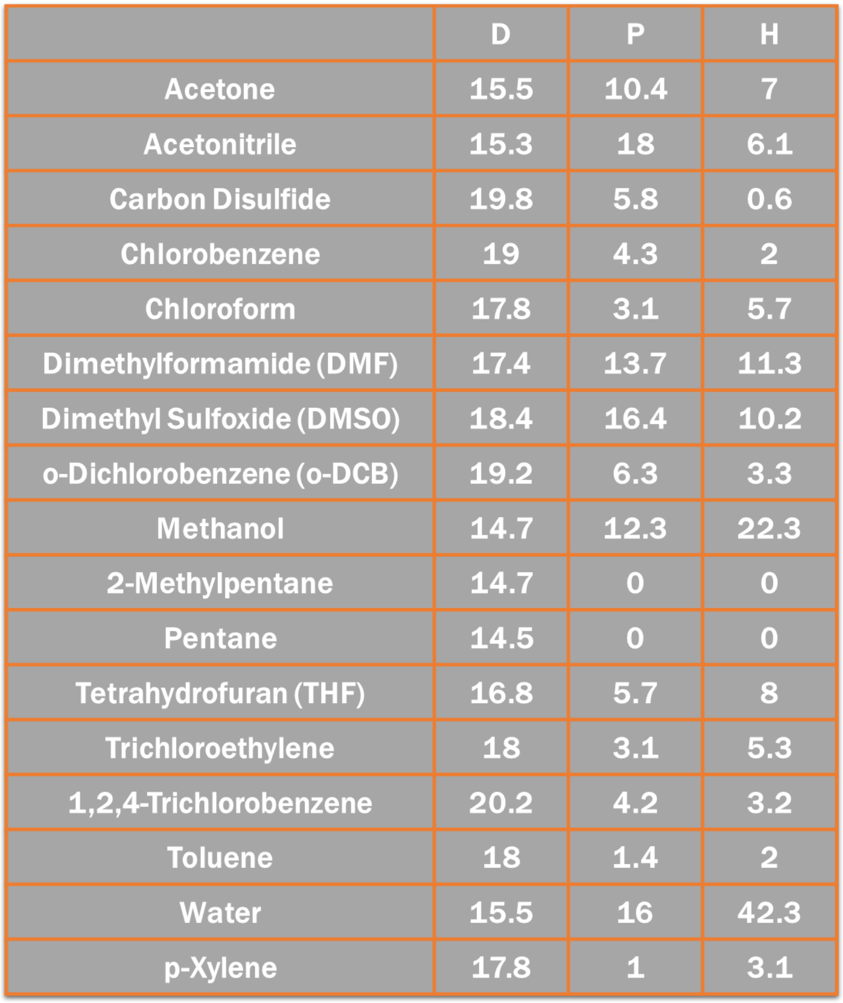

	D	P	H
Acetone	15.5	10.4	7
Acetonitrile	15.3	18	6.1
Carbon Disulfide	19.8	5.8	0.6
Chlorobenzene	19	4.3	2
Chloroform	17.8	3.1	5.7
Dimethylformamide (DMF)	17.4	13.7	11.3
Dimethyl Sulfoxide (DMSO)	18.4	16.4	10.2
o-Dichlorobenzene (o-DCB)	19.2	6.3	3.3
Methanol	14.7	12.3	22.3
2-Methylpentane	14.7	0	0
Pentane	14.5	0	0
Tetrahydrofuran (THF)	16.8	5.7	8
Trichloroethylene	18	3.1	5.3
1,2,4-Trichlorobenzene	20.2	4.2	3.2
Toluene	18	1.4	2
Water	15.5	16	42.3
p-Xylene	17.8	1	3.1

Figure 4.10 Table of solvents used for solubility test for Hansen solubility parameters calculation of P3HT and PDMS.

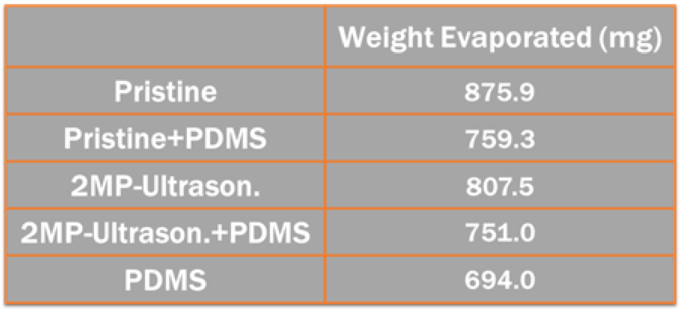

	Weight Evaporated (mg)
Pristine	875.9
Pristine+PDMS	759.3
2MP-Ultrason.	807.5
2MP-Ultrason.+PDMS	751.0
PDMS	694.0

Figure 4.11 Table representing weight of solvent ($CHCl_3$) evaporated after 14 hrs on top of 50 °C hot plate. Corresponding solutions were put in 2 ml vials. Difference of initial and final weight was measure to calculate the weight of evaporation.

Another factor known to impact conjugated polymer organization is solvent evaporation rate.[63,69,117] Slow solvent evaporation allows more times for polymer chains to be organized into ordered structures until solidification of film and polymer chains are fixed. In the case of both pristine and processed P3HT solutions, the presence of PDMS led in longer retention of solvent after film deposition (**Figure 4.11**). In combination with unfavorable interactions with PDMS, a decreased solvent evaporation rate may help provide for an environment whereby P3HT chains can interact in such way to lead to improved molecular ordering and thus enhanced charge carrier transport characteristics. The process is expected to be similar to using a solvent vapor annealing approach.[118]

The nanoscale morphologies of both the air and substrate interfaces of single component and blend films were interrogated using Atomic Force Microscopy (AFM). In contrast to P3HT films prepared from polymer solutions sequentially treated with poor solvent and ultrasonication, whose air and substrate interfaces appeared essentially identical (**Figure 4.12-a**); PDMS/P3HT blend films exhibited starkly different morphologies (**Figure 4.12-b**). The air interface presented a featureless morphology, largely identical to that of a PDMS film cast from diluted PDMS/$CHCl_3$ solution (**Figure 4.12-b inset**). In contrast, the substrate interface exhibited highly networked, well-defined P3HT structures.

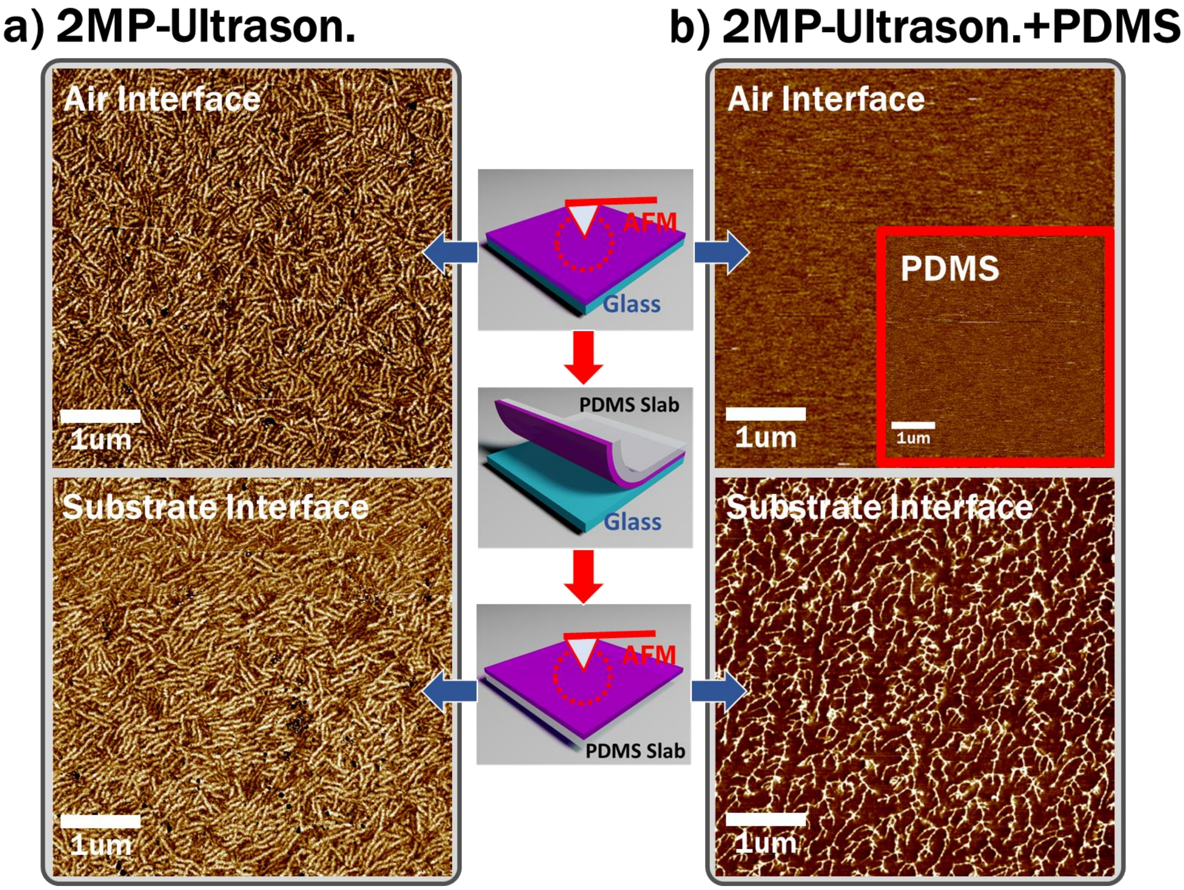

Figure 4.12-a, b AFM phase images of semiconducting film made from a) P3HT solution processed through poor solvent mediation and ultrasonication. b) poor solvent, ultrasound treated P3HT solution mixed with PDMS. Phase images of air interface were taken on top of glass. Then, same films were transferred to PDMS slab and phase images of substrate interface were taken. Phase image of PDMS film fabricated from PDMS/CHCl3 solution is inserted as inset.

AFM phase imaging, in combination with the OFET results points to vertical phase separation of the blend components, with P3HT preferentially residing at the substrate interface. Considering the low proportion of P3HT in the blend (0.75:100 w/w P3HT to PDMS), the semiconductor must also form a percolation network from the source to drain electrodes. From prior investigations, it has been shown that vertical phase separation of insulating polymer/organic semiconducting polymer composite systems can be induced and surface energy is believed to play a critical role.[115,116]

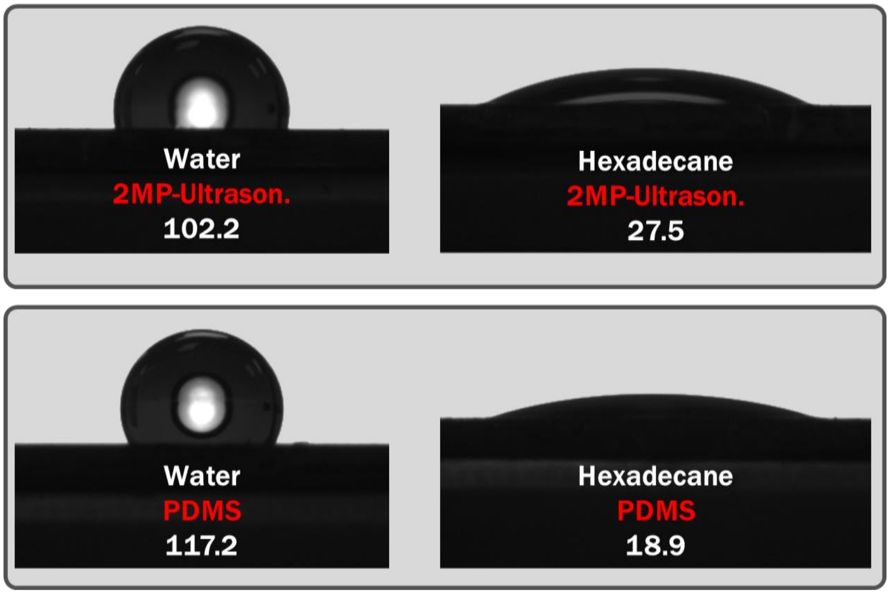

Figure 4.13 Contact angle measurement of a) P3HT film fabricated from 2-methylpentane treated then ultrasonicated P3HT solution b) PDMS film made from PDMS/CHCl3 solution. Water and hexadecane was used for measurement.

Here, processed P3HT which is relatively hydrophilic compared to PDMS (**Figure 4.13**), appears to preferentially migrate towards the SiO_2 interface. Conceivably, the difference in density between P3HT (1.1 g/cm^3)[119] and PDMS (0.92 g/cm^3)[120] might also drive semiconductor segregation towards the substrate.

Examination of **Figure 4.12**, also reveals highly networked P3HT nano- to microscale features at the film/substrate interface, which are quite different from the rod-like mesoscale structures present in the control films. The networked and branched moieties are reminiscent of dendritic crystals. Dendritic crystallization is known to take place when crystallization (molecular assembly in the case of P3HT) is carried out under diffusion-limited conditions.[121–124] Conceivably, the decrease in $CHCl_3$ evaporation rate in the presence of PDMS (**Figure 4.11**), leads to retention of solvent after film deposition. Thus, limited quantities of solvent allowing continued P3HT assembly which ultimately evaporates upon curing and presence of PDMS molecules limiting P3HT diffusion during continued assembly, may synergistically drive the semiconductor to adopt a dendritic like morphology.

The networked dendritic-like structure observed with the processed P3HT/PDMS blend may also help explain the observed increase in mechanical integrity upon external strain of processed P3HT/PDMS blend films compared to the more fragile films obtained from control solutions. The concept of fractal design has recently been introduced as a mechanism to enhance the mechanical integrity of stretched films and devices.[125,126] Conceptually, dendritic crystals provide for a natural fractal framework. Thus, the dendritic assembly of the semiconducting polymer within the elastomer blend film may well contribute to both the electrical and mechanical resiliency of the film. Molecular interactions drive conjugated polymer organization into a networked web, and the elastomer host matrix provides for intrinsic mechanical integrity upon stretching.

4.3 Conclusion

A definitive, direct relationship between the degree of semiconducting polymer molecular ordering/crystallinity and thin-film mechanical integrity upon external strain was determined. ‘Pre-processing’ of P3HT/$CHCl_3$ solutions allowed access to semiconducting thin-films having varied degrees of molecular ordering/crystallinity and charge carrier transport mobilities that spanned over one order of magnitude. Thin polymer film ductility deteriorated substantially as the degree of ordering improved. Given the positive impact of ordering/crystallinity on charge transport, a polymer blend approach was designed to resolve the dilemma posed by the inverse relationship between thin-film electrical performance and semiconducting polymer mechanical integrity. It was demonstrated that simple mixing of processed solutions of P3HT with solutions of PDMS elastomer afforded stretchable composite films that showed enhanced macroscopic charge carrier mobility. Specifically, the use of ‘pre-deposition processing’ techniques known to facilitate enhanced P3HT alignment/ordering/crystallinity with concomitant improvements in charge carrier mobility, afforded blend films exhibiting even higher levels of improvement. In the best case, a P3HT/PDMS blend prepared with ‘pre-deposition processed’ P3HT solution exhibited a hole mobility up to 44 times greater than pristine, untreated semiconducting polymer.

These results suggest that judicious choice of semiconducting material, inert polymer and solvent, coupled with evaluation of the intrinsic molecular interactions between each of the components will enable the design and development of truly flexible, bendable, and stretchable devices for a wide range of applications, including wearable electronics and biomedical devices. It is anticipated that such devices could be further integrated with alternate materials to allow for “shape-change” device architectures.

4.4 Experimental Section

Materials: P3HT (MW 69 kDa, polydispersity 2.3, 96% regioregularity) was purchased from Reike Metals Inc. and used without additional purification. Sylgard 184 PDMS elastomer kit from Dupont was used for fabricating PDMS slabs for film transfer and P3HT/PDMS mixtures. Chloroform (Anhydrous) and 2-Methylpentane were purchased from Sigma Aldrich.

Preparation of P3HT/PDMS Blend Solutions: Pristine P3HT chloroform solution was prepared at a concentration of 5mg/ml. Both the ultrasonicated and non-solvent/ultrasonicated solutions were prepared using literature procedures [57,86]. In both cases, the sonication time was 2 min. In the case of the latter, 15 vol. % of non-solvent (2-methylpentane) was added to the P3HT chloroform solution just prior to sonication. Simultaneously, PDMS solutions were prepared in the following manner. In 15ml of chloroform, 3 g of PDMS resin and 0.3 g of crosslinker was added and solution was vigorously shaken using Vortex Genie® for 30 s. Finally, 1ml of as-prepared P3HT solutions and 3ml of PDMS solution were mixed.

PDMS Slab for Film Transfer: PDMS slab having thickness of ~0.5cm was fabricated by mixing PDMS resin and crosslinker in 10:1 weight ratio. After thorough mixing, mixture was poured onto plastic plate and cured in a vacuum oven for 2 hours at 50 °C.

Semiconducting Thin Film Mechanical Property Test: Custom built linear stage with controller and sample holder was used for mechanical property test of semiconducting thin films. Samples were prepared by laminating semiconducting films spin-coated on top of glass substrate to PDMS slab. Prepared sample (Laminated semiconductor film on top of PDMS slab) was stretched using linear stage under X10 live CCD microscope connected to computer. Microscope was focused on the top surface of sample (semiconducting film part).

Organic Field-Effect Transistor (OFET) Fabrication and Characterization: Bottom-gate, bottom-contact OFET devices were fabricated to perform electrical characterization of P3HT/PDMS blend films. N-doped silicon wafers with a thermally grown 300 nm thick SiO_2 surface layer were used as the substrate. Doped silicon served as the gate electrode and SiO_2 served as the dielectric layer. Standard photolithography based on S1813 photoresist (MicroChem Corp.) was performed, followed by E-beam evaporation (Denton Explorer) of 50 nm Au contacts with 3 nm of Cr as the adhesion layer. Before spin-coating P3HT solutions, all devices were cleaned for 30 min in a UV-ozone cleaner (Novascan PSD-UV) to completely remove any residual photoresist and other organic contaminants. OFET devices were prepared by spin-coating (WS-650MZ-23NPP, Laurell) the relevant P3HT or P3HT/PDMS blend solutions onto pre-cleaned devices at a spin speed of 1500 rpm for 60 s in air. The devices were stored in a vacuum oven (1 Torr) for two days at 50 ℃ to remove residual solvent and the devices were then tested inside a nitrogen filled glove box using an Agilent 4155C semiconductor parameter analyzer. The field-effect hole mobility was calculated in the linear regime of transistor operation ($V_D = -3$ V) by plotting the drain current (I_D) versus gate voltage (V_G) and fitting the data to the following equation:

$$\mathrm{I}_D = \mu \mathrm{C}_{OX} \frac{W}{L} (V_G - V_T) V_D$$

where W (2000 μm) and L (50 μm) are the transistor channel width and length, respectively, V_T is the threshold voltage, and C_{OX} is the capacitance per unit area of the silicon dioxide gate dielectric (1.15×10^{-8} F/cm^2).

UV–Vis Spectra of P3HT: An Agilent 8510 Spectrophotometer was used to obtain both solution and solid state UV-Vis absorption spectra. Corresponding P3HT films were spin coated onto pre-cleaned glass slides.

Atomic Force Microscopy (AFM): An ICON dimension scanning probe microscope (Bruker) operated in tapping mode. NCS-14 from Mikromasch was used for AFM measurement of thin films on silicon substrate and NCS-15 for films on PDMS substrate.

CHAPTER 5

FUTURE WORKS

5.1 Understanding Inter-Moiety Charge Transport within Conjugated Polymer System

In previous section, through synergistic combination of solution processing techniques, molecular assembly of a model conjugated polymer, P3HT, could be successfully controlled. As a consequence, significant enhancement in macroscopic charge carrier mobility within conjugated polymer thin film was achieved. Here, we are proposing a further investigation of conjugated polymer thin film consisted of well-ordered moieties and amorphous region as a mean to expand our understanding of charge carrier transport property within and among the ordered P3HT nanostructures. In this study, processed P3HT solution containing more ordered P3HT nanorods and amorphous P3HT chains will be separated and electrical/photophysical properties of each component will be interrogated. As a preliminary study, centrifugal filtration was adopted to extract/concentrate P3HT nanorods from P3HT solution treated with combinational treatment of ultrasound and poor-solvent 2-methylpentane. First, 2 min of ultrasonication of $CHCl_3$-P3HT solution coupled with 15 vol.% addition of 2-methylpentane provided long P3HT nanorods as observed in previous section. Treated P3HT solution was then went through filtration using centrifugal filter. As assembled P3HT nanorods usually exceeds length of 200 nm, centrifugal filter with $CHCl_3$ resistant PVDF membrane

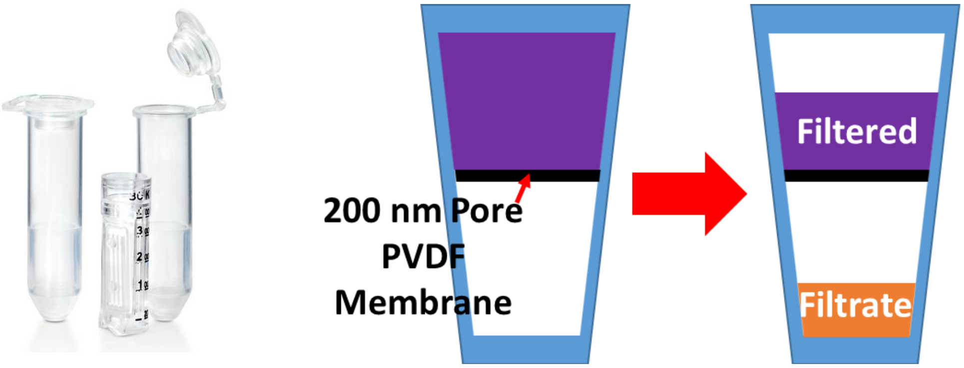

Figure 5.1 a) Actual photo of centrifugal filter system b) Scheme describing centrifugal filtration process

having 200 nm pore size was selected. Result was quite intriguing, through simple one step centrifugal filtration, assembled P3HT nanorods could be effectively segregated from amorphous chains. Color of ‘filtered’ P3HT solution at the top compartment above membrane, where original processed P3HT solution was poured, was stayed purple and opaque after filtration process while color of ‘filtrate’ solution at the bottom was

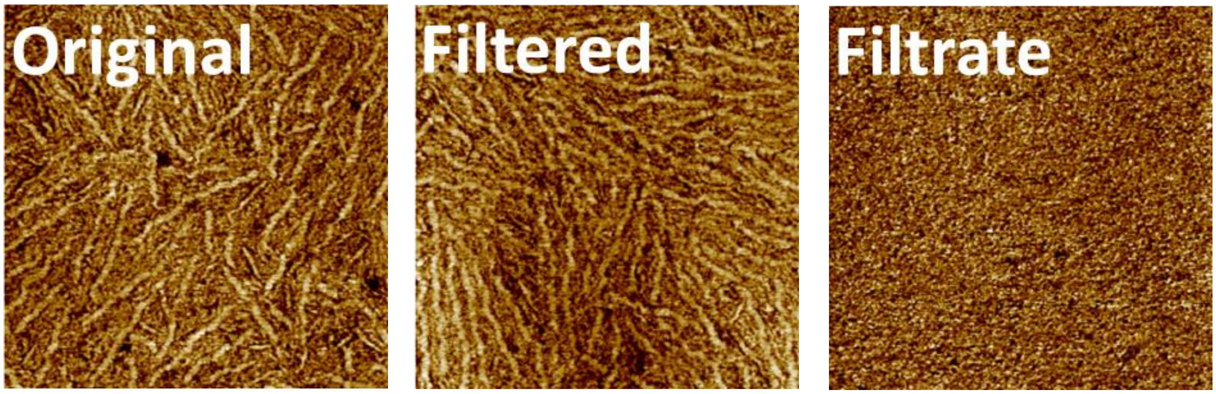

Figure 5.2 AFM phase images of P3HT films fabricated from left) P3HT solution treated with 2 min ultrasonication and 15 vol.% addition of 2-methylpentane middle) filtered P3HT solution right) filtrate P3HT solution

transparent orange. This clearly indicates successful separation of mesoscale, ordered P3HT nanorods inducing both color shift into purple and light scattering. AFM phase images of thin films fabricated from corresponding solution clearly followed expectation from a visual observation. P3HT thin film spin-coated from filtered solution included higher number of P3HT nanorods but with approximately same length when compared to original processed P3HT solution. Conversely, no ordered moiety could be observed in AFM phase image of P3HT film made from filtrate solution, concluding perfect segregation of mesoscale P3HT assemblies.

Utilizing effective segregation of ordered structures from amorphous polymer chains, electrical and photophysical properties of P3HT nanorods and amorphous chains might be elaborated. Number density of P3HT nanorods inside filtered solution is expected to be easily controlled by varying centrifugal speed for filtration. The comparison among P3HT films including differentiated number of P3HT nanorods having approximately same degree of ordering might provide us a crucial hint to understand more details about charge carrier transport from one ordered moiety to another.

5.2 Impact of Mesoscale Anisotropic Alignment on Mechanical Integrity of Conjugated Polymer Thin Films

Ordered, rod-like P3HT nanostructures, demonstrated in the previous chapter, have higher degree of orientation in terms of molecular packing when compared to randomly entangled amorphous P3HT polymers chains. So, macroscopic molecular orientation in specific direction can be achieved if larger scale, ordered moieties are aligned.

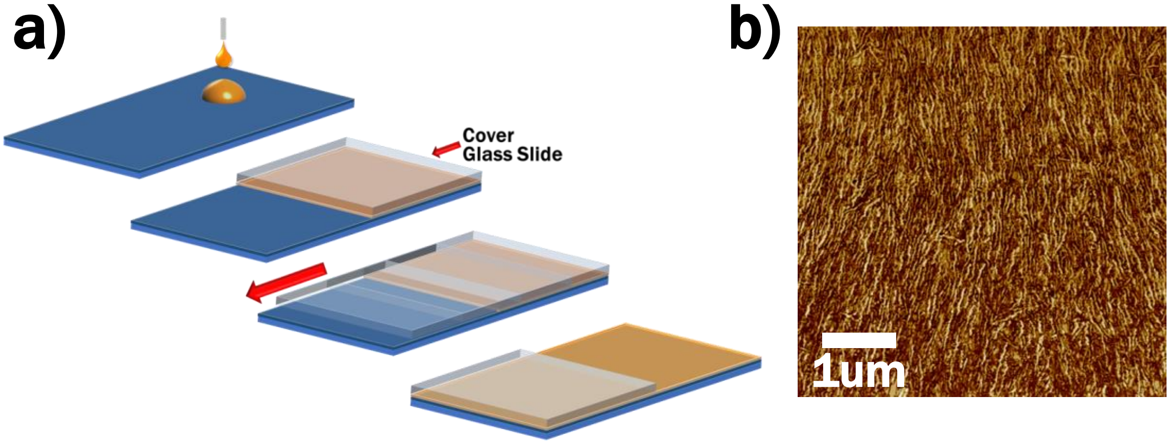

Figure 5.3 a) Scheme describing experimental procedure inducing couette-flow to processed P3HT solution. b) AFM phase image of resultant film with aligned P3HT nanorods.

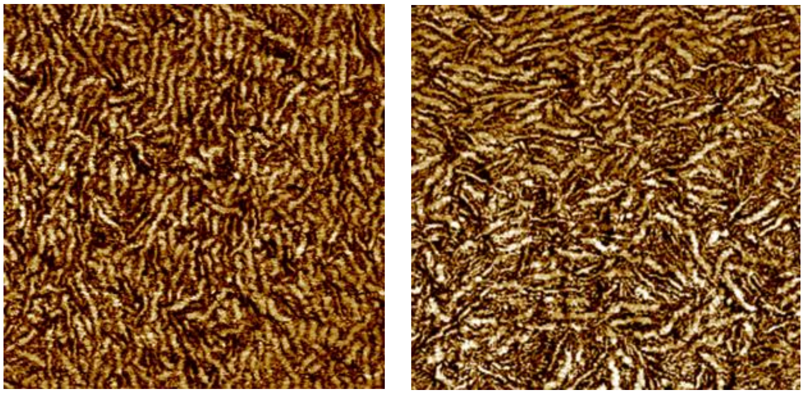

Figure 5.4 AFM phase images of P3HT films consisted of a) vertically aligned P3HT nanorods b) horizontally aligned P3HT nanorods

Rod-like, ordered P3HT moieties could be successfully aligned by inducing couette-flow using cover glass as a top plate. P3HT solution processed with ultrasound and poor solvent addition, containing high aspect ratio P3HT nanorods, was sandwiched between OFET device and cover glass. Then, cover glass was slowly removed at the speed of 20 um/sec while bottom substrate, which is OFET device was fixed. As a result, P3HT nanorods could be aligned in a large scale. From AFM phase images of resultant P3HT films, clear alignment of P3HT nanorods can be confirmed. Identical method was applied to align P3HT nanorods with lower aspect ratio, which were assembled only through ultrasound irradiation **(Figure 5.4)**. Result was also identical. P3HT nanorods were organized following direction of induced flow. Based on successful demonstration of inducing mesoscale P3HT structure alignment, thus giving macroscale orientation to P3HT molecules, relationship between macroscale direction of molecular orientation and directional external strain will be interrogated. External strain will be applied orthogonal and parallel to the direction of P3HT nanorods alignment.

REFERENCES

(1) Shirakawa, H.; Louis, E. J.; MacDiarmid, A. G.; Chiang, C. K.; Heeger, A. J. Synthesis of Electrically Conducting Organic Polymers: Halogen Derivatives of Polyacetylene, (CH) X. *J. Chem. Soc. Chem. Commun.* **1977**, 578.

(2) MacDiarmid, A. G. Nobel Lecture: "Synthetic Metals": A Novel Role for Organic Polymers. *Rev. Mod. Phys.* **2001**, *73*, 701–712.

(3) Kline, R. J.; McGehee, M. D. Morphology and Charge Transport in Conjugated Polymers. *J. Macromol. Sci. Part C Polym. Rev.* **2006**, *46*, 27–45.

(4) Klauk, H. Organic Thin-Film Transistors. *Chem. Soc. Rev.* **2010**, *39*, 2643–2666.

(5) Sirringhaus, H. Device Physics of Solution-Processed Organic Field-Effect Transistors. *Adv. Mater.* **2005**, *17*, 2411–2425.

(6) Mas-Torrent, M.; Rovira, C. Role of Molecular Order and Solid-State Structure in Organic Field-Effect Transistors. *Chem. Rev.* **2011**, *111*, 4833–4856.

(7) Wen, Y.; Liu, Y.; Guo, Y.; Yu, G.; Hu, W. Experimental Techniques for the Fabrication and Characterization of Organic Thin Films for Field-Effect Transistors. *Chem. Rev.* **2011**, *111*, 3358–3406.

(8) Huebler, A. C.; Doetz, F.; Kempa, H.; Katz, H. E.; Bartzsch, M.; Brandt, N.; Hennig, I.; Fuegmann, U.; Vaidyanathan, S.; Granstrom, J.; *et al.* Ring Oscillator Fabricated Completely by Means of Mass-Printing Technologies. *Org. Electron.* **2007**, *8*, 480–486.

(9) Voigt, M. M.; Guite, A.; Chung, D.-Y.; Khan, R. U. A.; Campbell, A. J.; Bradley, D. D. C.; Meng, F.; Steinke, J. H. G.; Tierney, S.; McCulloch, I.; *et al.* Polymer Field-Effect Transistors Fabricated by the Sequential Gravure Printing of Polythiophene, Two Insulator Layers, and a Metal Ink Gate. *Adv. Funct. Mater.* **2010**, *20*, 239–246.

(10) Schmidt, G. C.; Höft, D.; Haase, K.; Bellmann, M.; Kheradmand-Boroujeni, B.; Hassinen, T.; Sandberg, H.; Ellinger, F.; Hübler, A. C. Fully Printed Flexible Audio System on the Basis of Low-Voltage Polymeric Organic Field Effect Transistors with Three Layer Dielectric. *J. Polym. Sci. Part B Polym. Phys.* **2015**, *53*, 1409–1415.

(11) OLED-info. OLED Encapsulation: Technological introduction and market status http://www.oled-info.com/oled-encapsulation.

(12) Park, S.-H. K.; Oh, J.; Hwang, C.-S.; Lee, J.-I.; Yang, Y. S.; Chu, H. Y. Ultrathin Film Encapsulation of an OLED by ALD. *Electrochem. Solid-State Lett.* **2005**, *8*, H21.

(13) Ghosh, A. P.; Gerenser, L. J.; Jarman, C. M.; Fornalik, J. E. Thin-Film Encapsulation of Organic Light-Emitting Devices. *Appl. Phys. Lett.* **2005**, *86*, 223503.

(14) Mitani, M.; Endo, T.; Taniguchi, Y.; Katou, T.; Shimoto, S.; Ohno, T.; Tsuboi, S.; Okada, T.; Azuma, K.; Kawachi, G.; *et al.* Ultrahigh-Performance Polycrystalline Silicon Thin-Film Transistors on Excimer-Laser-Processed Pseudo-Single-Crystal Films. *Jpn. J. Appl. Phys.* **2008**, *47*, 8707–8713.

(15) Yuan, Y.; Giri, G.; Ayzner, A. L.; Zoombelt, A. P.; Mannsfeld, S. C. B.; Chen, J.; Nordlund, D.; Toney, M. F.; Huang, J.; Bao, Z. Ultra-High Mobility Transparent Organic Thin Film Transistors Grown by an off-Centre Spin-Coating Method. *Nat. Commun.* **2014**, *5*, 3005.

(16) Wu, W.; Liu, Y.; Zhu, D. Pi-Conjugated Molecules with Fused Rings for Organic Field-Effect Transistors: Design, Synthesis and Applications. *Chem. Soc. Rev.* **2010**, *39*, 1489–1502.

(17) Cheng, Y.-J.; Yang, S.-H.; Hsu, C.-S. Synthesis of Conjugated Polymers for Organic Solar Cell Applications. *Chem. Rev.* **2009**, *109*, 5868–5923.

(18) Kline, R. J.; Delongchamp, D. M.; Fischer, D. A.; Lin, E. K.; Richter, L. J.; Chabinyc, M. L.; Toney, M. F.; Heeney, M. Critical Role of Side-Chain Attachment Density on the Order and Device Performance of Polythiophenes. *Macromolecules* **2007**, *40*, 7960–7965.

(19) Sirringhaus, H. 25Th Anniversary Article: Organic Field-Effect Transistors: The Path Beyond Amorphous Silicon. *Adv. Mater.* **2014**, *26*, 1319–1335.

(20) *Organic & Printed Electronics Products and Related Components, a Global Market Survey*; 2015.

(21) Harrop, P. *Printed, Organic & Flexible Electronics Forecasts, Players & Opportunities*; 2012.

(22) McMurry, J. *Organic Chemistry*; 8th ed.; Cengage Learning, 2011.

(23) Fleming, I. *Molecular Orbitals and Organic Chemical Reactions, Student Edition*; Wiley-VCH Verlag GmbH & Co. KGaA, 2009.

(24) Ballhausen, C. A.; Gray, H. B. Molecular Orbital Theory: An Introductory Lecture Note and Reprint Volume, 1965.

(25) Mullen, K. *Electronic Materials : The Oligomer Approach*; Wiley-VCH Verlag GmbH & Co. KGaA, 1998.

(26) Hutchison, G. R.; Ratner, M. a; Marks, T. J. Intermolecular Charge Transfer between Heterocyclic Oligomers. Effects of Heteroatom and Molecular Packing on Hopping Transport in Organic Semiconductors. *J. Am. Chem. Soc.* **2005**, *127*, 16866–16881.

(27) Yamashita, Y.; Tsurumi, J.; Hinkel, F.; Okada, Y.; Soeda, J.; Zajączkowski, W.; Baumgarten, M.; Pisula, W.; Matsui, H.; Müllen, K.; *et al.* Transition between Band and Hopping Transport in Polymer Field-Effect Transistors. *Adv. Mater.* **2014**, *26*, 8169–8173.

(28) Coropceanu, V.; Cornil, J.; Filho, D.; Olivier, Y.; Silbey, R.; Bredas, J.-L. Charge Transport in Organic Semiconductors. *Chem. Rev.* **2012**, *312*, 1–65.

(29) Lin, L. *Theoretical Modeling of Intra- and Inter-Molecular Charge Transport*; 2012.

(30) Brown, P.; Thomas, D.; Köhler, A.; Wilson, J.; Kim, J.-S.; Ramsdale, C.; Sirringhaus, H.; Friend, R. Effect of Interchain Interactions on the Absorption and Emission of poly(3-Hexylthiophene). *Phys. Rev. B* **2003**, *67*, 064203.

(31) Liu, C.; Minari, T.; Lu, X.; Kumatani, A.; Takimiya, K.; Tsukagoshi, K. Solution-Processable Organic Single Crystals with Bandlike Transport in Field-Effect Transistors. *Adv. Mater.* **2011**, *23*, 523–526.

(32) Krupskaya, Y.; Gibertini, M.; Marzari, N.; Morpurgo, A. F. Band-Like Electron Transport with Record-High Mobility in the TCNQ Family. *Adv. Mater.* **2015**, *27*, n/a – n/a.

(33) Minder, N. A.; Ono, S.; Chen, Z.; Facchetti, A.; Morpurgo, A. F. Band-like Electron Transport in Organic Transistors and Implication of the Molecular Structure for Performance Optimization. *Adv. Mater.* **2012**, *24*, 503–508.

(34) Coropceanu, V.; Cornil, J.; da Silva Filho, D. A.; Olivier, Y.; Silbey, R.; Brédas, J.-L. Charge Transport in Organic Semiconductors. *Chem. Rev.* **2007**, *107*, 926–952.

(35) Brédas, J.-L.; Beljonne, D.; Coropceanu, V.; Cornil, J. Charge-Transfer and Energy-Transfer Processes in Pi-Conjugated Oligomers and Polymers: A Molecular Picture. *Chem. Rev.* **2004**, *104*, 4971–5004.

(36) Newman, C. R.; Frisbie, C. D.; da Silva Filho, D. A.; Brédas, J.-L.; Ewbank, P. C.; Mann, K. R. Introduction to Organic Thin Film Transistors and Design of N-Channel Organic Semiconductors. *Chem. Mater.* **2004**, *16*, 4436–4451.

(37) Kymissis, I. *Organic Field Effect Transistors*; Integrated Circuits and Systems; Springer US: Boston, MA, 2009.

(38) Sandler, S. I. *Chemical, Biochemical, and Engineering Thermodynamics*; 4th ed.; Wiley-VCH Verlag GmbH & Co. KGaA, 2006.

(39) Prausnitz, J.; Lichtenthaler, R.; Azevedo, E. G. *Molecular Thermodynamics of Fluid-Phase Equilibria*; 3rd Editio.; Prentice Hall, 1998.

(40) Stefanis, E.; Panayiotou, C. Prediction of Hansen Solubility Parameters with a New Group-Contribution Method. *Int. J. Thermophys.* **2008**, *29*, 568–585.

(41) Abbott, S.; Hansen, C. M. *Hansen Solubility Parameters in Practice Complete with Software , Data and Examples*; 2008.

(42) Hansen, C. M. 50 Years with Solubility Parameters—past and Future. *Prog. Org. Coatings* **2004**, *51*, 77–84.

(43) Hansen, M. The Universality of Solubility Parameter.

(44) Hansen, C. M. Solubility Parameters. **1995**.

(45) Miller-Chou, B. a.; Koenig, J. L. A Review of Polymer Dissolution. *Prog. Polym. Sci.* **2003**, *28*, 1223–1270.

(46) Blanks, R. F.; Prausnitz, J. M. Thermodynamics of Polymer Solubility in Polar and Nonpolar Systems. *Ind. Eng. Chem. Fundam.* **1964**, *3*, 1–8.

(47) Huang, Y.; Kramer, E. J.; Heeger, A. J.; Bazan, G. C. Bulk Heterojunction Solar Cells: Morphology and Performance Relationships. *Chem. Rev.* **2014**.

(48) Wang, C.; Dong, H.; Hu, W.; Liu, Y.; Zhu, D. Semiconducting Π-Conjugated Systems in Field-Effect Transistors: A Material Odyssey of Organic Electronics. *Chem. Rev.* **2012**, *112*, 2208–2267.

(49) Mei, Y.; Loth, M. A.; Payne, M.; Zhang, W.; Smith, J.; Day, C. S.; Parkin, S. R.; Heeney, M.; McCulloch, I.; Anthopoulos, T. D.; *et al.* High Mobility Field-Effect Transistors with Versatile Processing from a Small-Molecule Organic Semiconductor. *Adv. Mater.* **2013**, *25*, 4352–4357.

(50) Diemer, P. J.; Lyle, C. R.; Mei, Y.; Sutton, C.; Payne, M. M.; Anthony, J. E.; Coropceanu, V.; Brédas, J.-L.; Jurchescu, O. D. Vibration-Assisted Crystallization Improves Organic/dielectric Interface in Organic Thin-Film Transistors. *Adv. Mater.* **2013**, *25*, 6956–6962.

(51) Diao, Y.; Tee, B. C.-K.; Giri, G.; Xu, J.; Kim, D. H.; Becerril, H. A.; Stoltenberg, R. M.; Lee, T. H.; Xue, G.; Mannsfeld, S. C. B.; *et al.* Solution Coating of Large-Area Organic Semiconductor Thin Films with Aligned Single-Crystalline Domains. *Nat. Mater.* **2013**, *12*, 665–671.

(52) Giri, G.; Verploegen, E.; Mannsfeld, S. C. B.; Atahan-Evrenk, S.; Kim, D. H.; Lee, S. Y.; Becerril, H. A.; Aspuru-Guzik, A.; Toney, M. F.; Bao, Z. Tuning Charge Transport in Solution-Sheared Organic Semiconductors Using Lattice Strain. *Nature* **2011**, *480*, 504–508.

(53) Li, H.; Tee, B. C.-K.; Giri, G.; Chung, J. W.; Lee, S. Y.; Bao, Z. High-Performance Transistors and Complementary Inverters Based on Solution-Grown Aligned Organic Single-Crystals. *Adv. Mater.* **2012**, *24*, 2588–2591.

(54) Treat, N. D.; Nekuda Malik, J. A.; Reid, O.; Yu, L.; Shuttle, C. G.; Rumbles, G.; Hawker, C. J.; Chabinyc, M. L.; Smith, P.; Stingelin, N. Microstructure Formation in Molecular and Polymer Semiconductors Assisted by Nucleation Agents. *Nat. Mater.* **2013**, *12*, 628–633.

(55) Luo, C.; Kyaw, A. K. K.; Perez, L. A.; Patel, S.; Wang, M.; Grimm, B.; Bazan, G. C.; Kramer, E. J.; Heeger, A. J. General Strategy for Self-Assembly of Highly Oriented Nanocrystalline Semiconducting Polymers with High Mobility. *Nano Lett.* **2014**, *14*, 2764–2771.

(56) Tseng, H.-R.; Phan, H.; Luo, C.; Wang, M.; Perez, L. A.; Patel, S. N.; Ying, L.; Kramer, E. J.; Nguyen, T.-Q.; Bazan, G. C.; *et al.* High-Mobility Field-Effect Transistors Fabricated with Macroscopic Aligned Semiconducting Polymers. *Adv. Mater.* **2014**, *26*, 2993–2998.

(57) Aiyar, A. R.; Hong, J.-I.; Nambiar, R.; Collard, D. M.; Reichmanis, E. Tunable Crystallinity in Regioregular Poly(3-Hexylthiophene) Thin Films and Its Impact on Field Effect Mobility. *Adv. Funct. Mater.* **2011**, *21*, 2652–2659.

(58) Park, Y. D.; Lee, H. S.; Choi, Y. J.; Kwak, D.; Cho, J. H.; Lee, S.; Cho, K. Solubility-Induced Ordered Polythiophene Precursors for High-Performance Organic Thin-Film Transistors. *Adv. Funct. Mater.* **2009**, *19*, 1200–1206.

(59) De Yoreo, J. J. Principles of Crystal Nucleation and Growth. *Rev. Mineral. Geochemistry* **2003**, *54*, 57–93.

(60) Vekilov, P. G. Nucleation. *Cryst. Growth Des.* **2010**, *10*, 5007–5019.

(61) Ryu, B. H.; Ulrich, J. Controlled Nucleation and Growth of Protein Crystals by Solvent Freeze-Out. *Cryst. Growth Des.* **2012**, *12*, 6126–6133.

(62) Erdemir, D.; Lee, A. Y.; Myerson, A. S. Nucleation of Crystals from Solution: Classical and Two-Step Models. *Acc. Chem. Res.* **2009**, *42*, 621–629.

(63) Chang, J.-F.; Sun, B.; Breiby, D. W.; Nielsen, M. M.; Sölling, T. I.; Giles, M.; McCulloch, I.; Sirringhaus, H. Enhanced Mobility of Poly(3-Hexylthiophene) Transistors by Spin-Coating from High-Boiling-Point Solvents. *Chem. Mater.* **2004**, *16*, 4772–4776.

(64) Aiyar, A. R.; Hong, J.-I.; Izumi, J.; Choi, D.; Kleinhenz, N.; Reichmanis, E. Ultrasound-Induced Ordering in poly(3-Hexylthiophene): Role of Molecular and Process Parameters on Morphology and Charge Transport. *ACS Appl. Mater. Interfaces* **2013**, *5*, 2368–2377.

(65) Kelley, T. W.; Frisbie, C. D. Gate Voltage Dependent Resistance of a Single Organic Semiconductor Grain Boundary. *J. Phys. Chem. B* **2001**, *105*, 4538–4540.

(66) Rivnay, J.; Jimison, L. H.; Northrup, J. E.; Toney, M. F.; Noriega, R.; Lu, S.; Marks, T. J.; Facchetti, A.; Salleo, A. Large Modulation of Carrier Transport by Grain-Boundary Molecular Packing and Microstructure in Organic Thin Films. *Nat. Mater.* **2009**, *8*, 952–958.

(67) Street, R.; Northrup, J.; Salleo, A. Transport in Polycrystalline Polymer Thin-Film Transistors. *Phys. Rev. B* **2005**, *71*, 165202.

(68) Holzwarth, U.; Gibson, N. The Scherrer Equation versus the "Debye-Scherrer Equation". *Nat. Nanotechnol.* **2011**, *6*, 534.

(69) Chang, M.; Choi, D.; Fu, B.; Reichmanis, E.; Engineering, B.; Science, M.; States, U. Solvent Based Hydrogen Bonding : Impact on Poly (3-Hexylthiophene) Nanoscale Morphology and Charge. *ACS Nano* **2013**, 5402–5413.

(70) Nagarjuna, G.; Baghgar, M.; Labastide, J. A.; Algaier, D. D.; Barnes, M. D.; Venkataraman, D. Tuning Aggregation of poly(3-Hexylthiophene) within Nanoparticles. *ACS Nano* **2012**, *6*, 10750–10758.

(71) Winokur, M. J.; Spiegel, D.; Kim, Y.; Hotta, S.; Heeger, A. J. Structural and Absorption Studies of the Thermochromic Transition in poly(3-Hexylthiophene). *Synth. Met.* **1989**, *28*, 419–426.

(72) Clark, J.; Silva, C.; Friend, R.; Spano, F. Role of Intermolecular Coupling in the Photophysics of Disordered Organic Semiconductors: Aggregate Emission in Regioregular Polythiophene. *Phys. Rev. Lett.* **2007**, *98*, 206406.

(73) Chang, M.; Lee, J.; Kleinhenz, N.; Fu, B.; Reichmanis, E. Photoinduced Anisotropic Supramolecular Assembly and Enhanced Charge Transport of Poly(3-Hexylthiophene) Thin Films. *Adv. Funct. Mater.* **2014**.

(74) Huang, J.; Kertesz, M. Validation of Intermolecular Transfer Integral and Bandwidth Calculations for Organic Molecular Materials. *J. Chem. Phys.* **2005**, *122*, 234707.

(75) Troisi, A.; Orlandi, G. Dynamics of the Intermolecular Transfer Integral in Crystalline Organic Semiconductors. *J. Phys. Chem. A* **2006**, *110*, 4065–4070.

(76) Yamagata, H.; Pochas, C. M.; Spano, F. C. Designing J- and H-Aggregates through Wave Function Overlap Engineering: Applications to poly(3-Hexylthiophene). *J. Phys. Chem. B* **2012**, *116*, 14494–14503.

(77) Rawlings, J. B.; Miller, S. M.; Witkowski, W. R. Model Identification and Control of Solution Crystallization Processes: A Review. *Ind. Eng. Chem. Res.* **1993**, *32*, 1275–1296.

(78) Cubillas, P.; Anderson, M. W. SynthesisMechanism: Crystal Growth and Nucleation. In *Zeolites and Catalysis*; Wiley-VCH Verlag GmbH & Co. KGaA: Weinheim, Germany, 2010; pp. 1–55.

(79) Muthukumar, M. NUCLEATION IN POLYMER CRYSTALLIZATION. In *Advances in Chemical Physics*; John Wiley & Sons, Inc.: Hoboken, NJ, USA., 2004; Vol. 128.

(80) Hickling, R. Transient, High-pressure Solidification Associated with Cavitation in Water. *J. Acoust. Soc. Am.* **1994**, *73*, 2853–2856.

(81) Zhang, X.; Inada, T.; Tezuka, A. Ultrasonic-Induced Nucleation of Ice in Water Containing Air Bubbles. *Ultrason. Sonochem.* **2003**, *10*, 71–76.

(82) Oxtoby, D. W. Nucleation of First-Order Phase Transitions Gas - Liquid Nucleation. *Acc. Chem. Res.* **1998**, *31*, 91–97.

(83) Frydenberg, R. P.; Hammershøj, M.; Andersen, U.; Wiking, L. Ultrasonication Affects Crystallization Mechanisms and Kinetics of Anhydrous Milk Fat. *Cryst. Growth Des.* **2013**, *13*, 5375–5382.

(84) Knott, B. C.; LaRue, J. L.; Wodtke, A. M.; Doherty, M. F.; Peters, B. Communication: Bubbles, Crystals, and Laser-Induced Nucleation. *J. Chem. Phys.* **2011**, *134*, 171102.

(85) Kordylla, A.; Krawczyk, T.; Tumakaka, F.; Schembecker, G. Modeling Ultrasound-Induced Nucleation during Cooling Crystallization. *Chem. Eng. Sci.* **2009**, *64*, 1635–1642.

(86) Choi, D.; Chang, M.; Reichmanis, E. Controlled Assembly of Poly(3-Hexylthiophene): Managing the Disorder to Order Transition on the Nano- through Meso-Scales. *Adv. Funct. Mater.* **2015**, *25*, 920–927.

(87) Ikawa, M.; Yamada, T.; Matsui, H.; Minemawari, H.; Tsutsumi, J.; Horii, Y.; Chikamatsu, M.; Azumi, R.; Kumai, R.; Hasegawa, T. Simple Push Coating of Polymer Thin-Film Transistors. *Nat. Commun.* **2012**, *3*, 1176.

(88) Kim, S.-S.; Na, S.-I.; Jo, J.; Tae, G.; Kim, D.-Y. Efficient Polymer Solar Cells Fabricated by Simple Brush Painting. *Adv. Mater.* **2007**, *19*, 4410–4415.

(89) Aiyar, A. R.; Hong, J.-I.; Reichmanis, E. Regioregularity and Intrachain Ordering: Impact on the Nanostructure and Charge Transport in Two-Dimensional Assemblies of Poly(3-Hexylthiophene). *Chem. Mater.* **2012**, *24*, 2845–2853.

(90) Rughooputh, S. D. D. V.; Hotta, S.; Heeger, A. J.; Wudl, F. Chromism of Soluble Polythienylenes. *J. Polym. Sci. Part B Polym. Phys.* **1987**, *25*, 1071–1078.

(91) Nguyen, T.-Q.; Doan, V.; Schwartz, B. J. Conjugated Polymer Aggregates in Solution: Control of Interchain Interactions. *J. Chem. Phys.* **1999**, *110*, 4068.

(92) Cravotto, G.; Cintas, P. Molecular Self-Assembly and Patterning Induced by Sound Waves. The Case of Gelation. *Chem. Soc. Rev.* **2009**, *38*, 2684–2697.

(93) Bang, J. H.; Suslick, K. S. Applications of Ultrasound to the Synthesis of Nanostructured Materials. *Adv. Mater.* **2010**, *22*, 1039–1059.

(94) Brujan, E. Cavitation in Non-Newtonian Fluids. **2011**, 49–62.

(95) Savagatrup, S.; Printz, A. D.; O'Connor, T. F.; Zaretski, A. V.; Lipomi, D. J. Molecularly Stretchable Electronics. *Chem. Mater.* **2014**, *26*, 3028–3041.

(96) Chortos, A.; Bao, Z. Skin-Inspired Electronic Devices. *Mater. Today* **2014**, *17*, 321–331.

(97) Kim, B.-G.; Jeong, E. J.; Chung, J. W.; Seo, S.; Koo, B.; Kim, J. A Molecular Design Principle of Lyotropic Liquid-Crystalline Conjugated Polymers with Directed Alignment Capability for Plastic Electronics. *Nat. Mater.* **2013**, *12*, 659–664.

(98) Henson, Z. B.; Müllen, K.; Bazan, G. C. Design Strategies for Organic Semiconductors beyond the Molecular Formula. *Nat. Chem.* **2012**, *4*, 699–704.

(99) Venkateshvaran, D.; Nikolka, M.; Sadhanala, A.; Lemaur, V.; Zelazny, M.; Kepa, M.; Hurhangee, M.; Kronemeijer, A. J.; Pecunia, V.; Nasrallah, I.; *et al.*

Approaching Disorder-Free Transport in High-Mobility Conjugated Polymers. *Nature* **2014**, *515*, 384–388.

(100) Fu, B.; Baltazar, J.; Sankar, A. R.; Chu, P.-H.; Zhang, S.; Collard, D. M.; Reichmanis, E. Enhancing Field-Effect Mobility of Conjugated Polymers Through Rational Design of Branched Side Chains. *Adv. Funct. Mater.* **2014**, *24*, 3734–3744.

(101) Chen, Z.; Cai, P.; Chen, J.; Liu, X.; Zhang, L.; Lan, L.; Peng, J.; Ma, Y.; Cao, Y. Low Band-Gap Conjugated Polymers with Strong Interchain Aggregation and Very High Hole Mobility towards Highly Efficient Thick-Film Polymer Solar Cells. *Adv. Mater.* **2014**, *26*, 2586–2591.

(102) Zhang, M.; Guo, X.; Ma, W.; Ade, H.; Hou, J. A Large-Bandgap Conjugated Polymer for Versatile Photovoltaic Applications with High Performance. *Adv. Mater.* **2015**, *27*, n/a – n/a.

(103) Yuan, Y.; Giri, G.; Ayzner, A. L.; Zoombelt, A. P.; Mannsfeld, S. C. B.; Chen, J.; Nordlund, D.; Toney, M. F.; Huang, J.; Bao, Z. Ultra-High Mobility Transparent Organic Thin Film Transistors Grown by an off-Centre Spin-Coating Method. *Nat. Commun.* **2014**, *5*, 3005.

(104) Khim, D.; Han, H.; Baeg, K.-J.; Kim, J.; Kwak, S.-W.; Kim, D.-Y.; Noh, Y.-Y. Simple Bar-Coating Process for Large-Area, High-Performance Organic Field-Effect Transistors and Ambipolar Complementary Integrated Circuits. *Adv. Mater.* **2013**, *25*, 4302–4308.

(105) O’Connor, B.; Chan, E. P.; Chan, C.; Conrad, B. R.; Richter, L. J.; Kline, R. J.; Heeney, M.; McCulloch, I.; Soles, C. L.; DeLongchamp, D. M. Correlations between Mechanical and Electrical Properties of Polythiophenes. *ACS Nano* **2010**, *4*, 7538–7544.

(106) Lipomi, D. J.; Chong, H.; Vosgueritchian, M.; Mei, J.; Bao, Z. Toward Mechanically Robust and Intrinsically Stretchable Organic Solar Cells: Evolution of Photovoltaic Properties with Tensile Strain. *Sol. Energy Mater. Sol. Cells* **2012**, *107*, 355–365.

(107) Savagatrup, S.; Makaram, A. S.; Burke, D. J.; Lipomi, D. J. Mechanical Properties of Conjugated Polymers and Polymer-Fullerene Composites as a Function of Molecular Structure. *Adv. Funct. Mater.* **2014**, *24*, 1169–1181.

(108) Awartani, O.; Lemanski, B. I.; Ro, H. W.; Richter, L. J.; DeLongchamp, D. M.; O’Connor, B. T. Correlating Stiffness, Ductility, and Morphology of Polymer:Fullerene Films for Solar Cell Applications. *Adv. Energy Mater.* **2013**, *3*, 399–406.

(109) Savagatrup, S.; Printz, A. D.; Wu, H.; Rajan, K. M.; Sawyer, E. J.; Zaretski, A. V.; Bettinger, C. J.; Lipomi, D. J. Viability of Stretchable poly(3-Heptylthiophene) (P3HpT) for Organic Solar Cells and Field-Effect Transistors. *Synth. Met.* **2015**, *203*, 208–214.

(110) Shin, M.; Oh, J. Y.; Byun, K.-E.; Lee, Y.-J.; Kim, B.; Baik, H.-K.; Park, J.-J.; Jeong, U. Polythiophene Nanofibril Bundles Surface-Embedded in Elastomer: A Route to a Highly Stretchable Active Channel Layer. *Adv. Mater.* **2015**, *27*, 1255–1261.

(111) Song, Y.; Clafton, S. N.; Pensack, R. D.; Kee, T. W.; Scholes, G. D. Vibrational Coherence Probes the Mechanism of Ultrafast Electron Transfer in Polymer-Fullerene Blends. *Nat. Commun.* **2014**, *5*, 4933.

(112) Falke, S. M.; Rozzi, C. A.; Brida, D.; Maiuri, M.; Amato, M.; Sommer, E.; De Sio, A.; Rubio, A.; Cerullo, G.; Molinari, E.; *et al.* Coherent Ultrafast Charge Transfer in an Organic Photovoltaic Blend. *Science* **2014**, *344*, 1001–1005.

(113) Qiu, L.; Lee, W. H.; Wang, X.; Kim, J. S.; Lim, J. A.; Kwak, D.; Lee, S.; Cho, K. Organic Thin-Film Transistors Based on Polythiophene Nanowires Embedded in Insulating Polymer. *Adv. Mater.* **2009**, *21*, 1349–1353.

(114) Lu, G.; Blakesley, J.; Himmelberger, S.; Pingel, P.; Frisch, J.; Lieberwirth, I.; Salzmann, I.; Oehzelt, M.; Di Pietro, R.; Salleo, A.; *et al.* Moderate Doping Leads to High Performance of Semiconductor/insulator Polymer Blend Transistors. *Nat. Commun.* **2013**, *4*, 1588.

(115) Qiu, L.; Lim, J. A.; Wang, X.; Lee, W. H.; Hwang, M.; Cho, K. Versatile Use of Vertical-Phase-Separation-Induced Bilayer Structures in Organic Thin-Film Transistors. *Adv. Mater.* **2008**, *20*, 1141–1145.

(116) Arias, A. C.; Endicott, F.; Street, R. A. Surface-Induced Self-Encapsulation of Polymer Thin-Film Transistors. *Adv. Mater.* **2006**, *18*, 2900–2904.

(117) Yang, H.; LeFevre, S. W.; Ryu, C. Y.; Bao, Z. Solubility-Driven Thin Film Structures of Regioregular poly(3-Hexyl Thiophene) Using Volatile Solvents. *Appl. Phys. Lett.* **2007**, *90*, 172116.

(118) Dickey, K. C.; Anthony, J. E.; Loo, Y.-L. Improving Organic Thin-Film Transistor Performance through Solvent-Vapor Annealing of Solution-Processable Triethylsilylethynyl Anthradithiophene. *Adv. Mater.* **2006**, *18*, 1721–1726.

(119) Mikhnenko, O. V.; Azimi, H.; Scharber, M.; Morana, M.; Blom, P. W. M.; Loi, M. A. Exciton Diffusion Length in Narrow Bandgap Polymers. *Energy Environ. Sci.* **2012**, *5*, 6960.

(120) Armani, D.; Liu, C.; Aluru, N. Re-Configurable Fluid Circuits by PDMS Elastomer Micromachining. In *Technical Digest. IEEE International MEMS 99 Conference. Twelfth IEEE International Conference on Micro Electro Mechanical Systems (Cat. No.99CH36291)*; IEEE, 1999; pp. 222–227.

(121) Imai, H.; Oaki, Y. Emergence of Helical Morphologies with Crystals: Twisted Growth under Diffusion-Limited Conditions and Chirality Control with Molecular Recognition. *CrystEngComm* **2010**, *12*, 1679.

(122) Vicsek, T. Pattern Formation in Diffusion-Limited Aggregation. *Phys. Rev. Lett.* **1984**, *53*, 2281–2284.

(123) Langer, J. .; Müller-Krumbhaar, H. Theory of Dendritic growth—I. Elements of a Stability Analysis. *Acta Metall.* **1978**, *26*, 1681–1687.

(124) Wisniewski, W.; Patschger, M.; Rüssel, C. Viscous Fingering and Dendritic Growth of Surface Crystallized Sr2TiSi2O8 Fresnoite. *Sci. Rep.* **2013**, *3*, 3558.

(125) Kim, J.; Lee, M.; Shim, H. J.; Ghaffari, R.; Cho, H. R.; Son, D.; Jung, Y. H.; Soh, M.; Choi, C.; Jung, S.; *et al.* Stretchable Silicon Nanoribbon Electronics for Skin Prosthesis. *Nat. Commun.* **2014**, *5*, 5747.

(126) Fan, J. A.; Yeo, W.-H.; Su, Y.; Hattori, Y.; Lee, W.; Jung, S.-Y.; Zhang, Y.; Liu, Z.; Cheng, H.; Falgout, L.; *et al.* Fractal Design Concepts for Stretchable Electronics. *Nat. Commun.* **2014**, *5*, 3266.

VITA

Dalsu Choi

Dalsu Choi was born in Seoul, South Korea. At the age of 8, he moved to Gwangju, a city located in southern part of South Korea. After elementary and middle school years spent in Gwangju, he moved back to Seoul and attended Joong Dong High School. After high school graduation in 2007, he came to U.S. and enrolled in Purdue University, West Lafayette, Indiana. In 2011, he received a B.S. in Chemical Engineering from Purdue University, West Lafayette, Indiana. Upon graduation, Dalsu joined Prof. Elsa Reichmanis' research group to pursue Ph.D. degree in Chemical Engineering.

Dalsu is a huge music fan. He spends most of his free time listening to music of all genres including Jazz, Metal, Fusion, Classical, Lounge, Electronics, Pop, et cetera.